

Imperial College London
Department of Mechanical Engineering

Stochastic Modelling of Soot in Turbulent Combustion

Marcus Andreas Schiener

MEng

March 2018

Supervised by Professor R. P. Lindstedt

Submitted in part fulfilment of the requirements for the degree of
Doctor of Philosophy in Mechanical Engineering of
Imperial College London
and the Diploma of Imperial College London

Abstract

The current work studies the modelling of soot in turbulent combustion via a sectional model, a two-equation type approach, and the method of moments with interpolative closure in the framework of a transported probability density function model closed at joint-scalar level. Detailed sectional model calculations in a premixed well-stirred/plug flow reactor system are carried out, and updates to nucleation rates for acetylene-based soot nucleation models and soot oxidation rates used in previous work are proposed and evaluated. The updates are integrated into two-equation and method of moments calculations of two turbulent non-premixed jet flames burning ethylene and a methane based fuel, and the sensitivity to the surface area dependence of soot growth and oxidation is evaluated. Further, soot volume fraction statistics and particle size distributions (PSDs) were calculated for the turbulent ethylene flame using the sectional soot model, and an improved agreement with experimental data over the two-equation model results was noted, while the calculated PSDs demonstrate the capabilities of the model. Overall, the current work presents a significant advance upon previously published results obtained using a wide range of alternative approaches.

Declaration of Originality

I hereby certify that the present thesis is in full the work of the author,
with the work of others appropriately acknowledged.

Copyright Declaration

The copyright of this thesis rests with the author and is made available under a Creative Commons Attribution Non-Commercial No Derivatives licence. Researchers are free to copy, distribute or transmit the thesis on the condition that they attribute it, that they do not use it for commercial purposes and that they do not alter, transform or build upon it. For any reuse or redistribution, researchers must make clear to others the licence terms of this work.

Acknowledgements

First and foremost, I would like to express my most sincere gratitude to my academic supervisor Prof. Peter Lindstedt, whose guidance, support and encouragement made this work possible.

I wish to thank Dr Marco Zedda and Dr Simon Stow of Rolls Royce Derby and Dr Ruud Eggels of Rolls Royce Deutschland for technical discussions and the European Commission for financial support under the SOPRANO (award 690724 funded under H2020-EU.3.4) and DREAMCODE (award 620143 funded under FP7-JTI Clean Sky) projects.

I am fortunate to have met wonderful people along the way and would like to thank, in order of appearance, Dr Dehydys Pimentel, Dr Michalis Hadjipanayis, Dr Björn Waldheim and Mr Mosaab Alsunaidi for a warm welcome to the group and for passing on part of their wisdom; Dr Fabian Hampp for his valued perspective on numerous aspects of work and life; Dr Peter Kraus for his helpfulness, patience and for making me move more; Dr Francesco Galleni for talking politics over lunch; Dr Tao Li and Ms Lu Tian for setting such stellar examples; Mr Panagiotis Simatos for many a discussion about theoretical and practical aspects of combustion modelling and ongoing inspiration to try new things; Ms Aliko Tsopelakou and Mr Seyedhamed Shariatmadar for adding to the friendly atmosphere in rooms 208 and 674; and all of the above for good times in London, San Francisco, Budapest, Avignon and Seoul. A special thank you to Dr Outi Supponen for sharing the journey and cheering me on and to Dr Craig Leaper and everyone at Furnivall Rowing Club for getting me away from my desk and on to the water.

My parents Andreas and Gabriele Schiener and my sister Jasmin Schiener have always stood by my side, for which I am immensely grateful. Finally, a big thank you to Maria Torrentallé Dot for listening, your invaluable support and being there always.

Contents

List of Tables	7
List of Figures	9
Nomenclature	20
1 Introduction	24
1.1 Motivation and Overview	24
1.2 Turbulent Combustion Modelling	26
2 Soot Modelling	29
2.1 Background to Soot Modelling	29
2.2 Particle Dynamics	31
2.3 Nucleation	38
2.4 Surface Growth	40
2.5 Oxidation	44
2.6 Surface Area Dependence of Growth and Oxidation: The Functional Form of $f(A_s)$	45
2.7 Numerical Treatment of Surface Growth and Oxidation in the Sectional Model	46
2.8 Sectional Model: Properties of Soot Sections	47
2.9 Chemical Reaction Model	49
3 Soot Particle-Size Predictions in a Premixed Reactor Configuration	50
3.1 Experimental Configuration and Model	50
3.2 Results and Discussion	52
3.3 Conclusions	56
4 Soot Modelling in a Turbulent Natural Gas Diffusion Flame With Local Extinction and Re-Ignition	59

4.1	Introduction	59
4.2	Case Configuration	61
4.3	Results and Discussion	66
4.3.1	Velocity and Scalar Fields	66
4.3.2	Soot Statistics	79
4.4	Conclusions	88
5	Soot Modelling in the Sandia Turbulent Ethylene Diffusion Flame	90
5.1	Introduction	90
5.2	Case Configuration	90
5.3	Overview of Growth/Oxidation Model Assumptions and Reaction Rates	93
5.4	Results and Discussion	97
5.4.1	Scalar Fields	97
5.4.2	Soot Statistics	99
5.5	Conclusions	110
6	Soot Particle Size Distributions in the Sandia Flame	112
6.1	Introduction	112
6.2	Results and Discussion	113
6.3	Conclusions	125
7	Conclusions and Future Work	126
7.1	Conclusions	126
7.2	Future Work	128
A	Structures of Species	130
	Bibliography	131

List of Tables

2.1	Reaction rate constants for the PAH analogy of soot surface chemistry [80] presented in the form $A_i \alpha_i T^{\beta_i} \exp(-E_i/RT)$. Units are in K, kmol, m ³ and s.	43
3.1	Reaction rate constants for soot nucleation via Eq. (2.29) presented in the form $k_{N,i} = A_i \exp(-E_i/RT)$. Units are in K, kmol, m ³ and s.	51
3.2	Reaction rate constants for soot growth and oxidation in Eqs. (2.35) and (2.59)-(2.61) presented in the form $A_i \alpha_i T^{\beta_i} \exp(-E_i/RT)$ [27, 28, 96]. Units are in K, kmol, m ³ and s.	51
4.1	Composition of Delft flame main fuel jet in percent mole fraction in experiments and model: Dutch natural gas, California natural gas diluted with N ₂ , Adelaide natural gas diluted with N ₂ , and modified compositions of the latter two (Model 1 and 2).	62
4.2	Reaction rate constants for soot nucleation via Eq. (2.29) presented in the form $k_{N,i} = A_i \exp(-E_i/RT)$. Units are in K, kmol, m ³ and s.	64
4.3	Reaction rate constants for soot growth and oxidation in Eqs. (2.35) and (2.59)-(2.61) presented in the form $A_i \alpha_i T^{\beta_i} \exp(-E_i/RT)$ [27, 28, 96]. Units are in K, kmol, m ³ and s.	64
5.1	Overview of calculations modelling nucleation via $k_{N,1}$ [27] or $k_{N,5}$ [23].	93
5.2	Overview of calculations with updated nucleation rates.	93
5.3	Reaction rate constants for soot nucleation via Eq. (2.29) presented in the form $k_{N,i} = A_i \exp(-E_i/RT)$. Units are in K, kmol, m ³ and s.	96

5.4	Reaction rate constants for soot growth and oxidation for $f(A_s) = A_s$ (DSA) presented in the form $A_i \alpha_i T^{\beta_i} \exp(-E_i/RT)$ [27, 28]. Units are in K, kmol, m ³ and s.	96
5.5	Reaction rate constants for soot growth and oxidation for $f(A_s) = [\rho N_s]$ (ISA) presented in the form $A_i \alpha_i T^{\beta_i} \exp(-E_i/RT)$ [27, 28]. Units are in K, kmol, m ³ and s.	96
5.6	Reaction rate constants for soot growth for $f(A_s) = \sqrt{A_s}$ (PSSA) presented in the form $A_i \alpha_i T^{\beta_i} \exp(-E_i/RT)$ [27, 28]. Units are in K, kmol, m ³ and s.	96
5.7	Recommended sets of models and parameters for the two-equation model.	111
6.1	Reaction rate constants for soot growth and oxidation in Eqs. (2.35) and (2.59)-(2.61) presented in the form $A_i \alpha_i T^{\beta_i} \exp(-E_i/RT)$ [27, 28, 96]. Units are in K, kmol, m ³ and s.	112
A.1	The structures of the aromatic species in the PAH analogy model for soot surface growth by Lindstedt and Louloudi [28, 30].	130

List of Figures

2.1	A scheme of the soot formation and oxidation model, based on Bockhorn [55]. Particle inception both via polycyclic aromatic hydrocarbons (PAHs) and an acetylene-based nucleation model is considered in this work.	30
3.1	Calculated soot particle size distributions in the WSR and at PFR Ports 1 and 3 of the WSR/PFR setup of Lenhert and Manzello [18] with C_2H_4 /air at $\Phi = 2.0$ and $T_{WSR} = 1723$ K. Comparison of measurements and computations using pyrene (A_4) and acetylene based nucleation models with reaction rate coefficients $k_{N,1}$ by Lindstedt [27], $k_{N,2}$ for diffusion flames by Sunderland and Faeth [76], $k_{N,3}$ and $k_{N,4}$ from Table 4.2. A constant value for the surface reactivity parameter of $\alpha_s = 0.85$ and the updated oxidation rates k_O , $k_{OH,2}$ and $k_{O_2,2}$ were used.	53
3.2	Calculated soot particle size distributions in the WSR and at PFR Port 3 of the WSR/PFR setup of Lenhert and Manzello [18] with C_2H_4 /air at $\Phi = 2.0$ and $T_{WSR} = 1723$ K. Comparison of measurements and computations using pyrene (A_4) and acetylene based nucleation models with reaction rate coefficients $k_{N,3}$ and $k_{N,4}$ from Table 4.2. A constant value for the surface reactivity parameter of $\alpha_s = 0.85$, and the oxidation rates k_O , $k_{OH,1}$ and $k_{O_2,1}$ were used.	54

3.3	Calculated soot particle size distributions in the WSR and at PFR Port 3 of the WSR/PFR setup of Lenhert and Manzello [18] with C_2H_4/air at $\Phi = 2.0$ and $T_{WSR} = 1723$ K. The sensitivity to the van der Waals enhancement factor C_a is shown. Computations use C_2H_2 nucleation into pyrene (A_4) with the rate $k_{N,3}$, $\alpha_s = 0.85$, and the oxidation rates $k_O, k_{OH,2}$ and $k_{O_2,2}$	55
3.4	Calculated soot particle size distributions in the WSR and at PFR Port 3 of the WSR/PFR setup of Lenhert and Manzello [18] with C_2H_4/air at $\Phi = 2.0$ and $T_{WSR} = 1723$ K. The sensitivity to uncertainties in the temperature are shown. Computations use C_2H_2 nucleation into pyrene (A_4) with the rate $k_{N,3}$, $\alpha_s = 0.85$, and the oxidation rates $k_O, k_{OH,2}$ and $k_{O_2,2}$	57
3.5	Calculated soot particle size distributions in the WSR and at PFR Port 3 of the WSR/PFR setup of Lenhert and Manzello [18] with C_2H_4/air at $\Phi = 2.0$ and $T_{WSR} = 1723$ K for different values of the surface reactivity parameter α_s . Computations use C_2H_2 nucleation into pyrene (A_4) with the rate $k_{N,3}$ and the oxidation rates $k_O, k_{OH,2}$ and $k_{O_2,2}$	57
3.6	Calculated soot particle size distributions in the WSR and at PFR Port 3 of the WSR/PFR setup of Lenhert and Manzello [18] with C_2H_4/air at $\Phi = 2.0$ and $T_{WSR} = 1723$ K. Calculations with C_2H_2 based nucleation into pyrene (A_4) and naphthalene (A_2) are shown. The nucleation rate $k_{N,3}$, $\alpha_s = 0.85$, and the oxidation rates $k_O, k_{OH,2}$ and $k_{O_2,2}$ were used.	58
3.7	Calculated soot particle size distributions in the WSR and at PFR Port 3 of the WSR/PFR setup of Lenhert and Manzello [18] with C_2H_4/air at $\Phi = 2.0$ and $T_{WSR} = 1723$ K. The nucleation rate $k_{N,3}$, $\alpha_s = 0.85$, and the oxidation rates $k_O, k_{OH,2}$ and $k_{O_2,2}$ were used. The influence of additional oxidation via Eq. (2.63) with rate $k_{O_2,PAH}$ is shown.	58
4.1	Top and side view of the Delft burner head. Dimensions in mm.	61

4.2	Laminar burning velocity of natural gas obtained from laminar premixed flame calculations with strain rate $a \approx 100 \text{ s}^{-1}$ (○) with a sum-of-sines fit for $0.35 \leq \Phi \leq 1.95$ (—). The "Model 2" composition defined in Table 4.1 was used. . . .	63
4.3	(a) Calculated temperature map in the Delft flame. (b) Grid detail at $60 \leq x/d \leq 66$. (c) Grid detail near the nozzle. Control volume boundaries are shown with white lines. . . .	65
4.4	Radial profiles of Favre mean axial velocity \tilde{U} and RMS of axial (u'') and radial (v'') velocity in the Delft III / Adelaide flame at axial positions $8\frac{1}{3} \leq x/d \leq 41\frac{2}{3}$. Comparison of calculations (lines) to experimental data (symbols) by Stroomeer [112]. The "Model 1" fuel composition was used for calculations (see Table 4.1).	68
4.5	Calculated radial profiles of Favre mean mixture fraction \tilde{f} , black lines) and its RMS (f'' , red lines) in the Delft III / Adelaide flame at axial positions $8\frac{1}{3} \leq x/d \leq 41\frac{2}{3}$. Comparison to mean (black squares) and RMS (circles) from experimental data by Nooren et al. [21, 22]. The "Model 2" fuel composition was used for calculations (see Table 4.1).	69
4.6	Calculated radial profiles of Favre mean temperature (\tilde{T} , black lines/dots) and its RMS (T'' , red lines/dots) in the Delft III / Adelaide flame at axial positions $8\frac{1}{3} \leq x/d \leq 41\frac{2}{3}$ (a) in physical space and (b) in mixture fraction space. Comparison to mean (black squares) and RMS (circles) from experimental data by Nooren et al. [21, 22]. The mapping to mixture fraction space was obtained via the calculated and measured Favre mean mixture fractions. The "Model 2" fuel composition was used (see Table 4.1).	70

4.7	Calculated radial profiles of Favre mean H ₂ O mass fraction (\bar{y}_{H_2O} , black lines/dots) and its RMS (y''_{H_2O} , red lines/dots) in the Delft III / Adelaide flame at axial positions $8\frac{1}{3} \leq x/d \leq 41\frac{2}{3}$ (a) in physical space and (b) in mixture fraction space. Comparison to mean (black squares) and RMS (circles) from experimental data by Nooren et al. [21, 22]. The "Model 2" fuel composition was used (see Table 4.1). The mapping to mixture fraction space was obtained via the calculated and measured Favre mean mixture fractions.	71
4.8	Calculated radial profiles of Favre mean CO ₂ mass fraction (\bar{y}_{CO_2} , black lines/dots) and its RMS (y''_{CO_2} , red lines/dots) in the Delft III / Adelaide flame at axial positions $8\frac{1}{3} \leq x/d \leq 41\frac{2}{3}$ (a) in physical space and (b) in mixture fraction space. Comparison to mean (black squares) and RMS (circles) from experimental data by Nooren et al. [21, 22]. The "Model 2" fuel composition was used (see Table 4.1). The mapping to mixture fraction space was obtained via the calculated and measured Favre mean mixture fractions.	72
4.9	Calculated radial profiles of Favre mean O ₂ mass fraction (\bar{y}_{O_2} , black lines/dots) and its RMS (y''_{O_2} , red lines/dots) in the Delft III / Adelaide flame at axial positions $8\frac{1}{3} \leq x/d \leq 41\frac{2}{3}$ (a) in physical space and (b) in mixture fraction space. Comparison to mean (black squares) and RMS (circles) from experimental data by Nooren et al. [21, 22]. The "Model 2" fuel composition was used (see Table 4.1). The mapping to mixture fraction space was obtained via the calculated and measured Favre mean mixture fractions.	73
4.10	Calculated radial profiles of Favre mean H ₂ mass fraction (\bar{y}_{H_2} , black lines/dots) and its RMS (y''_{H_2} , red lines/dots) in the Delft III / Adelaide flame at axial positions $8\frac{1}{3} \leq x/d \leq 41\frac{2}{3}$ (a) in physical space and (b) in mixture fraction space. Comparison to mean (black squares) and RMS (circles) from experimental data by Nooren et al. [21, 22]. The "Model 2" fuel composition was used (see Table 4.1). The mapping to mixture fraction space was obtained via the calculated and measured Favre mean mixture fractions.	74

4.11	Calculated radial profiles of Favre mean CH_4 mass fraction (\tilde{y}_{CH_4} , black lines/dots) and its RMS (y''_{CH_4} , red lines/dots) in the Delft III / Adelaide flame at axial positions $8\frac{1}{3} \leq x/d \leq 41\frac{2}{3}$ (a) in physical space and (b) in mixture fraction space. Comparison to mean (black squares) and RMS (circles) from experimental data by Nooren et al. [21, 22]. The "Model 2" fuel composition was used (see Table 4.1).	75
4.12	Calculated radial profiles of Favre mean CO mass fraction (\tilde{y}_{CO} , black lines/dots) and its RMS (y''_{CO} , red lines/dots) in the Delft III / Adelaide flame at axial positions $8\frac{1}{3} \leq x/d \leq 41\frac{2}{3}$ (a) in physical space and (b) in mixture fraction space. Comparison to mean (black squares) and RMS (circles) from experimental data by Nooren et al. [21, 22]. The "Model 2" fuel composition was used (see Table 4.1). The mapping to mixture fraction space was obtained via the calculated and measured Favre mean mixture fractions.	76
4.13	Radial profiles of OH mass fraction in the Delft III / Adelaide flame at axial positions $8\frac{1}{3} \leq x/d \leq 41\frac{2}{3}$. Calculated (a) Favre mean \tilde{y}_{OH} (black lines), and (b) RMS y''_{OH} (red lines). Comparison to experimental data (squares) by Nooren et al. [21, 22]. The "Model 2" fuel composition was used (see Table 4.1).	77
4.14	Radial profiles of Favre mean OH mass fraction (\tilde{y}_{OH} , black dots) and its RMS (y''_{OH} , red dots) in the Delft III / Adelaide flame at axial positions $8\frac{1}{3} \leq x/d \leq 41\frac{2}{3}$ in mixture fraction space. Comparison to mean (black squares) and RMS (circles) from experimental data by Nooren et al. [21, 22]. The "Model 2" fuel composition was used (see Table 4.1). The mapping to mixture fraction space was obtained via the calculated and measured Favre mean mixture fractions.	78
4.15	Centre-line profiles of Favre mean of soot volume fraction in the Delft III / Adelaide flame. Comparison of predictions (—) from the two-equation model to experimental data (·) by Qamar et al. [113]. The "Model 2" fuel composition was used for calculations (see Table 4.1).	81

4.16	Centre-line profiles of Favre mean of soot volume fraction in the Delft III / Adelaide flame. Comparison of predictions (—) from the method of moments model with interpolative closure to experimental data (·) by Qamar et al. [113]. The "Model 2" fuel composition was used for calculations (see Table 4.1).	82
4.17	Centre-line profiles of Favre mean of soot volume fraction in the Delft III / Adelaide flame. Predictions (—) from the two-equation model including the PAH analogy model for soot surface chemistry with $\alpha_s = 0.50$. Comparison to experimental data (·) by Qamar et al. [113]. The "Model 2" fuel composition was used for calculations (see Table 4.1). . . .	83
4.18	Centre-line profile of calculated Favre mean mixture fraction (—) in the Delft III / Adelaide flame. Soot peak locations from calculations at $x/d \approx 82$ and measurements at $x/d \approx 116$ and corresponding calculated mixture fraction shown as (· · ·). Comparison to experimental data (□) by Nooren et al. [21, 22]. The "Model 2" fuel composition was used for calculations (see Table 4.1).	84
4.19	Favre mean soot volume fraction at the centre-line in mixture fraction space in the Delft III / Adelaide flame. Predictions from the two-equation model with $k_{N,4}, k_O, k_{OH,2}, k_{O_2,2}$. (a) The standard growth step and (b) the PAH analogy for soot surface chemistry were used. Comparison to experimental data by Qamar et al. [113], where the mapping to mixture fraction was obtained from the respective calculations. The lean and rich flammability limits of methane f_{LFL}, f_{RFL} and the stoichiometric mixture fraction for the Adelaide natural gas f_{st} are shown for comparison. The "Model 2" fuel composition was used for calculations (see Table 4.1).	85

4.20	Radial profiles of Favre mean of soot volume fraction in the Delft flame. Comparison of computations featuring the two-equation model with experimental data (black lines) by Qamar et al. [113]. The rates $k_O, k_{OH,2}, k_{O_2,2}$ and either $k_{N,3}$ (blue lines) or $k_{N,4}$ (red lines) were used for calculations. The axial locations of the measured profiles are shown, with the computed data corresponding to locations $36 x/d$ further upstream and the radial locations normalised, to account for the difference in peak locations and the rate of spread of the jet. The "Model 2" fuel composition was used for calculations (see Table 4.1).	86
4.21	Radial profiles of Favre mean of soot volume fraction in the Delft flame. Comparison of computations featuring the two-equation model and the PAH analogy for soot surface chemistry with $\alpha_s = 0.50$ with experimental data (black lines) by Qamar et al. [113]. The rates $k_O, k_{OH,2}, k_{O_2,2}$ and either $k_{N,3}$ (blue lines) or $k_{N,4}$ (red lines) were used for calculations. The axial locations of the measured profiles are shown, with the computed data corresponding to locations $36 x/d$ further upstream and the radial locations normalised, to account for the difference in peak locations and the rate of spread of the jet. The "Model 2" fuel composition was used for calculations (see Table 4.1).	87
5.1	(a) Calculated temperature map in the Sandia flame. (b) Grid detail at $40 \leq x/d \leq 50$. (c) Grid detail near the nozzle. Control volume boundaries are shown with white lines. . . .	92
5.2	(a) Functional dependence of α_s on the maximum temperature of laminar flames by Kazakov et al. [81]. (b) Mixture fraction dependence of the surface reactivity parameter α_s , based on the functional dependence and a laminar diffusion flamelet approximation with a strain rate of 100 s^{-1}	95

5.3	Radial profiles of calculated (—) Favre mean mass fraction of OH in the Sandia flame and measured (\square) OH mass fraction in normalised arbitrary units. Calculated data is smoothed via a centred moving average filter with window size $0.2 d$. Comparison to experimental data by Shaddix [140].	97
5.4	Radial profiles of calculated Favre mean temperature in the Sandia flame and measured soot temperature. Calculated data is smoothed via a centred moving average filter with window size $0.2 d$. Lines and symbols as in Fig. 5.3. Comparison to experimental data by Shaddix [140].	98
5.5	Radial profiles of calculated Favre mean mass fraction of C_2H_2 in the Sandia flame and measured PAH mass fraction in normalised arbitrary units. Calculated data is smoothed via a centred moving average filter with window size $0.2 d$. Lines and symbols as in Fig. 5.3. Comparison to experimental data by Shaddix [140].	98
5.6	Predictions of Favre mean (—) and RMS (---) of soot volume fraction at the centre-line of the Sandia flame. (a) Case 1, (b) Case 2. Soot mass growth and oxidation are modelled as proportional to the soot surface area (DSA). Comparison to measured mean (\square) and RMS (\circ) from [141].	99
5.7	Predictions of Favre mean and RMS of soot volume fraction at the centre-line of the Sandia flame. (a) Case 3, (b) Case 4. Soot mass growth and oxidation are modelled as independent of the soot surface area (ISA). Lines and symbols as in Fig. 5.6.	100
5.8	Predictions of Favre mean and RMS of soot volume fraction at the centre-line of the Sandia flame. (a) Case 5, (b) Case 6. Soot mass growth and oxidation are modelled as independent of soot surface area (ISA), with the modified oxidation rates $k_{O,3}$, $k_{OH,3}$, $k_{O_2,3}$. Lines and symbols as in Fig. 5.6.	101
5.9	Predictions of Favre mean and RMS of soot volume fraction at the centre-line of the Sandia flame. (a) Case 8, (b) Case 9. Soot mass growth is modelled as proportional to $\sqrt{A_s}$ (PSSA), and oxidation as proportional to the soot surface area (DSA). Lines and symbols as in Fig. 5.6.	101

5.10	The sensitivity of soot volume fraction predictions at the centre-line of the Sandia flame to the nucleation rate. (a/b): Surface area dependent soot mass growth and oxidation based on Case 1 (DSA). (c/d): Surface area independent growth/oxidation (ISA) based on Case 5. Lines and symbols as in Fig. 5.6.	102
5.11	Predictions of Favre mean and RMS of soot volume fraction at the centre-line of the Sandia flame. (a) Case 1b, (b) Case 2b. Soot mass growth and oxidation are modelled as proportional to the soot surface area (DSA). Lines and symbols as in Fig. 5.6.	103
5.12	Radial profiles of (a) Favre mean and (b) RMS of soot volume fractions in the Sandia flame. Calculated data is smoothed via a centred moving average filter with window size $0.2 d$. Comparison of predictions (—) from Case 1b to experimental data (---) from [141].	104
5.13	Radial profiles of (a) Favre mean and (b) RMS of soot volume fractions in the Sandia flame. Calculated data is smoothed via a centred moving average filter with window size $0.2 d$. Comparison of predictions (—) from Case 2b to experimental data (---) from [141].	105
5.14	Predictions of Favre mean and RMS of soot volume fraction at the centre-line of the Sandia flame. a) Case 5b, b) Case 6b. Soot mass growth and oxidation are modelled as independent of soot surface area (ISA), with the modified oxidation rates $k_{O,3}$, $k_{OH,3}$, $k_{O_2,3}$. Lines and symbols as in Fig. 5.6.	106
5.15	Predictions of Favre mean and RMS of soot volume fraction at the centre-line of the Sandia flame. (a) Case 8b (a) Case 9b Soot mass growth is modelled as proportional to $\sqrt{A_s}$ (PSSA), and oxidation as proportional to the soot surface area (DSA). Lines and symbols as in Fig. 5.6.	107

5.16	Predictions of Favre mean and RMS of soot volume fraction at the centre-line of the Sandia flame. Calculations are based on Cases 2 and 6, with a functional dependence of α_s on mixture fraction. Soot mass growth and oxidation are modelled as either dependent on (DSA) or independent of (ISA) soot surface area, the latter with the modified oxidation rates $k_{O,3}$, $k_{OH,3}$, $k_{O_2,3}$. Lines and symbols as in Fig. 5.6.	108
5.17	Predictions of Favre mean and RMS of soot volume fraction at the centre-line of the Sandia flame. Calculations are based on (a) Case 1b, (b) Case 5b, (c) Case 2, (d) Case 6, (e) Case 2b, (f) Case 6b, with only coagulation in the free molecular regime considered. A modified two-equation soot model with the original growth step (top row) and the soot surface chemistry growth model by Lindstedt and Louloudi [30] (middle and bottom row) is used. Lines and symbols as in Fig. 5.6.	109
6.1	Predictions of Favre mean (—) and RMS (---) of soot volume fraction from the sectional model at the centre-line of the Sandia flame using different sets of oxidation rates. Incipient soot particles are assigned the properties of pyrene, $C_a = 3.0$ and $\alpha_s = 0.35$. Comparison to measured mean (\square) and RMS (\circ) from [141].	114
6.2	Radial profiles of predictions (—) of (a) Favre mean and (b) RMS of soot volume fraction from the sectional model in the Sandia flame. Calculated data is smoothed via a centred moving average filter with window size $0.2 d$. Incipient soot particles are assigned the properties of pyrene, $C_a = 3.0$, $\alpha_s = 0.35$ and $k_O, k_{OH,2}, k_{O_2,2}$ are used. Comparison to experimental data (---) from [141].	115
6.3	Soot predictions from the sectional model at the centre-line of the Sandia flame for different values of the surface reactivity parameter α_s . Incipient soot particles are assigned the properties of pyrene, $C_a = 3.0$ and $k_O, k_{OH,2}, k_{O_2,2}$ are used. Lines and symbols as in Fig. 6.1.	116

6.4	Soot predictions from the sectional model at the centre-line of the Sandia flame using a functional dependence of α_s on mixture fraction. Incipient soot particles are assigned the properties of pyrene, $C_a = 3.0$ and $k_O, k_{OH,2}, k_{O_2,2}$ are used. Lines and symbols as in Fig. 6.1.	117
6.5	Soot predictions from the sectional model at the centre-line of the Sandia flame. Incipient soot particles are assigned the properties of naphthalene. $C_a = 3.0$, $\alpha_s = 0.35$ and $k_O, k_{OH,2}, k_{O_2,2}$ are used. Lines and symbols as in Fig. 6.1.	117
6.6	Soot predictions from the sectional model at the centre-line of the Sandia flame for different values of the van der Waals enhancement factor C_a . Incipient soot particles are assigned the properties of pyrene, $\alpha_s = 0.35$ and $k_O, k_{OH,2}, k_{O_2,2}$ are used. Lines and symbols as in Fig. 6.1.	118
6.7	Soot predictions from the sectional model at the centre-line of the Sandia flame. Additional O_2 oxidation via the surface chemistry based expression by Lindstedt and Waldheim [13] was introduced. Incipient soot particles are assigned the properties of pyrene, $C_a = 3.0$, $\alpha_s = 0.35$ and $k_O, k_{OH,2}, k_{O_2,2}$ are used. Lines and symbols as in Fig. 6.1.	119
6.8	Calculated particle size distributions at the centre-line of the Sandia flame.	120
6.9	Calculated particle size distributions at different radial positions and axial position $x/d = 40$ of the Sandia flame.	121
6.10	Calculated particle size distributions at different radial positions and axial position $x/d = 100$ of the Sandia flame.	122
6.11	Calculated particle size distributions at different radial positions and axial position $x/d = 150$ of the Sandia flame.	123
6.12	Calculated particle size distributions at different radial positions and axial position $x/d = 200$ of the Sandia flame.	124

Nomenclature

Latin Symbols

A_i, B_i, C_i	'Three-point' method coefficients
A_p	Soot surface area in (m ² /particle)
A_s	Soot surface area in (m ² /m ³ -mixture)
a	Strain rate
$a_{p,i}$	Planck mean absorption coefficient of species i
C	RADCAL model constant
C_a	Van der Waals enhancement factor
C_ϕ, C_ϕ^*	Dissipation rate closure constants
C_i	Cunningham slip correction factor of size class i
C_{min}	Minimum number of carbon atoms
d	Exit-plane jet diameter
D_f	Fractal dimension of soot aggregates
$d_c, d_{c,i}$	Fractal aggregate diameter
d_i	Particle diameter for size class i
d_p	Mean particle diameter
$d_{p,min}$	Incipient particle diameter
d_{prim}	Diameter of primary particles (largest spherical particles)
f	Mixture fraction
\tilde{f}_ϕ	Density-weighted PDF
f_{LFL}, f_{RFL}	Mixture fraction at lean and rich flammability limits
f_s	Geometric spacing factor for soot sections
f_{st}	Stoichiometric mixture fraction
f_v	Soot volume fraction
H	Enthalpy
$J_{l,\alpha}$	Molecular diffusion flux vector
k	Turbulence kinetic energy
k_B	Boltzmann constant
$k_i^f(T), k_i^f$	Forward rate constant for reaction i
$k_G(T), k_G, k_{G,i}$	Soot growth reaction rate constant
$k_N(T), k_N(T)', k_{N,i}$	Soot nucleation reaction rate constants
$k_{OH,i}, k_{O,i}, k_{O_2,i}$	Soot oxidation reaction rate constants

$k_i^r(T), k_i^r$	Reverse rate constant for reaction i
M_0, M_1, M_2, M_3, M_r	Moments of the soot particle size distribution function
M_C	Molar mass of carbon
m_A	Aggregate mass
m_i	Mass per particle in section i
$m_{M,i}$	Mass per particle in section i in number of carbon atoms
m_{prim}	Mass of primary particles (largest spherical particles)
N_A	Avogadro's number
N_{bin}	Number of soot sections
N_p	Number of primary particles per soot aggregate
N_s	Soot particle number density in (particles/kg-mixture)
N_i	Number concentration of particles in section i
P_1, P_2	Moments of the size distribution of primary soot particles per aggregate
p	Pressure
p_i	Partial pressure of species i
Q_{RAD}	Volumetric radiative heat loss rate
$R_G, R_{G,i}$	Soot growth source terms
$R_N, R_N', R_{N,i}$	Soot nucleation source terms
$R_O, R_{O,i}$	Soot oxidation source terms
$R_{CIA}, R_{CIA,i}$	Coagulation/agglomeration source terms
S_α	Mean reaction rate of species α
T, T_b	Temperature, background temperature
T_{WSR}	Temperature in the well-stirred reactor
t	Time
\tilde{U}	Favre mean axial velocity
u_i	Velocity vector
u_L	Laminar burning velocity
u'', v''	RMS of axial and radial velocity
u_η	Kolmogorov velocity scale
v_i	Volume per particle in section i
\underline{x}, x_i	Cartesian coordinate vector
x	Axial coordinate in axisymmetric system
\underline{Y}, Y_i	Species mass fractions
Y_s	Soot mass fraction
y	Radial coordinate in axisymmetric system

Greek Symbols

α_s	Soot surface reactivity parameter
$\beta_{j,k}, \beta$	Particle collision rate
δ	Jet half-width
δ_{ij}	Kronecker delta
ε	Turbulent kinetic energy dissipation rate
$\eta_{i,j,k}$	Coagulation mass distribution coefficient
λ	Gas mean free path
μ_L	Laminar dynamic viscosity
μ_t	Turbulent eddy viscosity
ν	Kinematic viscosity
$\rho, \bar{\rho}$	Density, mean density
ρ_s	Density of soot
ρ_u	Density of unburnt reactants
σ_t	Prandtl number
σ_{SB}	Stefan-Boltzmann constant
τ_T^{-1}	Turbulence time scale
τ_ϕ^{-1}	Scalar mixing time scale
Φ	Equivalence ratio
$\underline{\phi}, \phi_\alpha$	Scalar random variable
χ_s	PAH analogy model term
χ_{s-h}	Number of active sites per unit area on the soot surface
$\underline{\psi}, \psi_\alpha$	Scalar sample space of $\underline{\phi}, \phi_\alpha$
ω	Normalised stream function coordinate
ω_l^r	Forward molar reaction rate of reaction l
ω_r^r	Reverse molar reaction rate of reaction l

Subscripts

α	Scalar field index
$a2$	Secondary air co-flow
f	Fuel jet

Superscripts

\sim	Density-weighted average
$''$	Favre fluctuation
0	Standard conditions
A	Agglomeration
C	Cogulation
c	Continuum regime of coagulation/agglomeration
f	Free molecular regime of coagulation/agglomeration
t	Transition regime of coagulation/agglomeration

Abbreviations and Acronyms

A ₂	Naphthalene (C ₁₀ H ₈)
A ₄	Pyrene (C ₁₆ H ₁₀)
CI	Compression ignition
DI	Direct injection
DLCA	Diffusion limited cluster aggregate
Kn	Knudsen number
PAH	Polycyclic aromatic hydrocarbon
PFR	Plug flow reactor
Re	Reynolds number
WSR	Well-stirred reactor

1. Introduction

1.1. Motivation and Overview

Emissions of particulate matter (PM) or soot produced in combustion processes from engines and power stations are directly linked to health and environmental effects [1]. Health effects include oxidative stress and inflammation to lung tissue [2], the contribution to cardiovascular disease [3], and cancer [4]. Particulate matter entering the airways may redistribute to other parts of the body such as the spleen and liver. It has been recognized that the size of the particles plays a crucial role in this process, with finer particles with diameters in the nanometre range considered more hazardous [5]. Legislators have begun to acknowledge the importance of reducing emissions of small particles, with recent regulations taking into account the size of the particles emitted, specifying limits for particles smaller than $10\ \mu\text{m}$ (PM10) and $2.5\ \mu\text{m}$ (PM2.5) [6]. When emitted from aircraft engines at high altitudes, PM is contributing to cloud formation causing local and global effects on climate [7]. Regulations for emissions from aviation have long been less strict than those for automotive applications, with current regulations taking into account Smoke Numbers and hence targeting the total particle mass. The situation is evolving, with a framework currently being developed by the International Civil Aviation Organization (ICAO) taking into account size distributions of the emitted particles in addition to their mass [8]. Restrictions on particulate matter have long been part of the emission standards for vehicles sold in the European Union (EU) and European Economic Area (EEA), with limits on PM emissions from compression ignition (CI, i.e. diesel) engines in passenger cars and light commercial vehicles, as well as from heavy duty diesel engines in trucks and buses imposed since the Euro I/I standards taking effect in 1992 (and 1994 for light commercial vehicles) [9, 10]. Regulations have become stricter over the years, and have been expanded to include heavy-duty gas engines (Euro III, 1999/2000) and direct injection (DI) gasoline engines (Euro 5, 2009/2010), with the current Euro 6 standard limiting PM emission from passenger cars and light commercial vehicles to

0.0045 g/km. Similar standards exist in other markets, with e.g. the current Tier 3 SFTP standards regulating particulate matter emissions from light-duty vehicles in the United States gradually tightening until 2024 [11, 12]. The size of soot particles is a more recent focus, and has been regulated in the EU via the number of particles emitted since 2011 for car/light duty vehicle CI engines and 2015 for DI gasoline engines (Euro 5b/6, 6×10^{11} particles/km), and 2013 for truck and bus heavy-duty diesel and gas engines (Euro VI, 8×10^{11} and 6×10^{11} particles/km, respectively).

The advancement of soot and particulate modelling capabilities for design purposes accordingly remains important, with the development of methods allowing the prediction of soot mass as well as particle size distributions (PSDs) a current focus. The current work contributes to this pursuit by studying the calculation of soot formation from combustion under turbulent, non-premixed conditions, relevant to practical applications. In the interest of improving the generality of models, a premixed reactor-system is also considered, and both ethylene and a methane-based fuel are included. The focus of this work is on reactor systems and flames of laboratory scale, allowing the development of models at moderate cost in comparably well-defined setups, for which experimental data is readily obtainable.

In the following section, the pertinent aspects of the calculation method used for turbulent flames is summarised. In Chapter 2, the soot models in the current work are discussed in detail, comprising a sectional soot model, a two-equation type approach and the method of moments with interpolative closure. Lindstedt and Waldheim [13, 14] combined the soot mass and number density preserving fixed sectional approach of Bhatt and Lindstedt [15], based on the work of Kumar and Ramkrishna [16], with a detailed chemical reaction model featuring 358 species up to pyrene and 1789 reactions. Based on this work, predictions of soot particle size distributions in the combined WSR/PFR reactor configuration of Manzello et al. [17, 18] are presented in Chapter 3, aiming to elucidate the role of the applied soot nucleation and oxidation rates for soot particle size distribution predictions. In particular, the calculations provide an alternative evaluation of the impact of simplified soot nucleation rate expressions. An update to the soot nucleation and oxidation rates used in previous work is proposed, and evaluated in the context of joint-scalar transported PDF modelling [19] of turbulent flames in Chapters 4 to 6. In Chapter 4, soot formation in the Delft III / Adelaide turbulent natural gas jet flame [20–22] is studied via both two-equation [23] and method of moments type approaches [24]. The study of soot modelling via two-equation models is extended

in the context of the Sandia turbulent ethylene jet flame [25, 26] in Chapter 5, to further evaluate assumptions made in previous work [23, 27, 28] concerning the role of soot surface area in growth and oxidation models. The detailed sectional soot model is then introduced into turbulent flame calculations of the Sandia flame using the joint-scalar transported PDF approach, and results are presented in Chapter 6. Finally, the contributions of the current work are summarised along with suggestions for future work in Chapter 7.

1.2. Turbulent Combustion Modelling

The computational approach for turbulent combustion calculations in this work features a two-dimensional implicit parabolic flow solver, based on the well-established $x-\omega$ transformation [29], coupled with a Lagrangian particle implementation for the solution of the transport equation of joint scalar probability density function [19]:

$$\begin{aligned} \frac{\partial \bar{\rho} \tilde{f}_{\phi}}{\partial t} + \frac{\partial}{\partial x_l} \left[\bar{\rho} \tilde{u}_l \tilde{f}_{\phi} \right] + \frac{\partial}{\partial \psi_{\alpha}} \left[\bar{\rho} S_{\alpha} \tilde{f}_{\phi} \right] = & - \frac{\partial}{\partial x_l} \left[\bar{\rho} \langle u_l'' | \psi \rangle \tilde{f}_{\phi} \right] \\ & + \frac{\partial}{\partial \psi_{\alpha}} \left[\left\langle \frac{1}{\rho} \frac{\partial}{\partial x_l} J_{l,\alpha} \middle| \psi \right\rangle \bar{\rho} \tilde{f}_{\phi} \right] \end{aligned} \quad (1.1)$$

The two turbulent flame configurations studied in this work are jet flames with high Reynolds and Peclet numbers without recirculation and be adequately modelled via a GENMIX type parabolic flow solver [29]. This choice reduces the computational cost compared to the use of elliptic flow solvers. Soot is included using three alternative methods: The solution of two additional equations [23, 27, 30] for soot mass (Y_s) and number density (N_s), the alternative treatment of soot particle dynamics via the method of moments with interpolative closure (MOMIC) [24], as well as a sectional approach to soot modelling [15, 16, 31]. The former approach, termed the two-equation model, computes the evolution of the first two moments of the soot particle size distribution function (PSDF), and appeals due to its relative simplicity. The MOMIC approach allows the inclusion of further moments of the PSDF and of the size distribution of primary soot particles per aggregate. The method therefore, at least in principle, improves accuracy, at the cost of an increased complexity. Studying the jet flames of Kent and Honnery [32] and Coppalle and Joyeux [33], Lindstedt and Louloudi [28, 30] reported the

two methods to yield similar soot predictions, and the performance of both is here compared via calculations of the Delft flame. In either of these moment based methods, monodispersity of soot is assumed, i.e. only the calculation of a mean particle size is allowed. They are therefore insufficient where the knowledge of soot PSDs is required. Sectional models solve a balance equation for the evolution of the population of soot particles via some discretisation method. They inherently grant access to the particle size distribution, and their inclusion in turbulent reacting flow models is of great interest. For the two-equation model, the method solves the transport equation of the joint scalar PDF $\tilde{f}_\phi = (\underline{\psi}; \underline{x}, t)$ with $\underline{\psi}$ denoting the sample space of the random vector $\underline{\phi} = (\underline{Y}, f, H, Y_s, N_s)$, where \underline{Y} are the mass fractions of species, f is the mixture fraction, H denotes enthalpy, Y_s is the mass fraction of soot and N_s the number density of the soot particles. For the method of moments, the first four moments (M_0 – M_3) of the PSDF and two moments (P_1 – P_2) of the primary particle size distribution are included, such that the vector becomes $\underline{\phi} = (\underline{Y}, f, H, M_0, M_1, M_2, M_3, P_1, P_2)$. For the sectional model, the concentrations of soot particles in a number of specified soot sections N_j covering a selected size range (e.g. from below 1 nm to over 100 nm) are included, such that the random vector is defined by $\underline{\phi} = (\underline{Y}, f, H, N_j)$. Radiative heat losses from gas phase species H_2O , CO , CO_2 and CH_4 and soot are accounted for by means of an optically thin model [34, 35],

$$Q_{RAD} = 4\sigma_{SB} \times \left(\sum_{i=1}^K p_i a_{P,i} (T^4 - T_b^4) \right) + 4\sigma_{SB} C f_v (T^5 - T_b^5) \quad (1.2)$$

where σ_{SB} is the Stefan–Boltzmann constant ($5.669 \times 10^{18} \text{ W m}^{-2} \text{ K}^{-4}$), p_i is the partial pressure of species i in atmospheres, $a_{P,i}$ the Planck mean absorption coefficient of species i in [$\text{m}^{-1} \text{ atm}^{-1}$], T the local temperature, $T_b = 295 \text{ K}$ is the background temperature, $C = 1.307 \times 10^3 \text{ m}^{-1} \text{ K}^{-1}$ [28], and f_v is the local soot volume fraction. The velocity field is obtained via the Speziale, Sarkar and Gatski (SSG) second order closure [36] and the generalized gradient diffusion assumption [37] as also used by Louloudi [28] and Lindstedt and Louloudi [30]. The scalar mixing term in the transported PDF equation is modelled using the modified Curl’s model of Janicka et al. [38], with standard and extended closures for the scalar dissipation rate as discussed below.

The standard expression for the scalar mixing time scale τ_ϕ is related to the ratio

of the turbulence kinetic energy \tilde{k} and its dissipation rate $\tilde{\varepsilon}$,

$$\tau_\phi^{-1} = \frac{C_\phi \tilde{\varepsilon}}{2 \tilde{k}} = \frac{C_\phi}{2} \tau_T^{-1}, \quad (1.3)$$

assuming a uniform ratio of the local turbulence time scale τ_T and the local mixing time scale τ_ϕ in the whole domain. The parameter C_ϕ has been the subject of parametric studies and, in conjunction with Curl's mixing model, Lindstedt et al. [39, 40] proposed a value of 2.3. For the current set-up, values in the range $2.3 \leq C_\phi \leq 6.0$ were explored to facilitate sustained ignition. In the context of premixed and partially premixed turbulent flames, a simple extended closure for the scalar time scale was derived by Kuan et al. [41],

$$\tau_\phi^{-1} = \frac{C_\phi}{2} \left[1.0 + C_\phi^* \frac{\rho_u u_L}{\bar{\rho} u_\eta} \right] \tau_T^{-1}, \quad (1.4)$$

where ρ_u denotes the density of the unburnt reactants, $\bar{\rho}$ the local mean density, u_L is the local laminar burning velocity, a function of the mixture fraction (or equivalence ratio), and $u_\eta = (\nu \tilde{\varepsilon})^{1/4}$ is the local Kolmogorov velocity scale, defined via the local kinematic viscosity ν and the turbulence dissipation rate $\tilde{\varepsilon}$. The formulation leads to a local increase of the scalar mixing frequency in regions with equivalence ratios corresponding to flammable mixtures. The closure has been validated for a range of conditions including premixed [41, 42], partially premixed [43] and non-premixed flames [44]. Lindstedt et al. [43] assessed the impact of different scalar dissipation rate closure approximations for a set of piloted partially premixed CH₄/H₂/air turbulent jet flames at $\text{Re} \approx 60,000$ and 67,000. Excessive flame extinction was observed for the conventional closure (Eq. (1.3)) for the range of $2.3 \leq C_\phi \leq 4.0$, whereas the extended closure (Eq. (1.4)) produced good agreement with measurements. In the current work, the latter is applied, with $C_\phi = 2.3$ and $C_\phi^* = 1.2$ retained from previous work.

2. Soot Modelling

2.1. Background to Soot Modelling

The improvement of soot predictions in turbulent flames remains important for the reduction of particulate emissions in practical applications. Historically, most soot models have relied on numerical solutions of some form of the transport equation for the particle number density function (NDF), e.g. a population balance equation (PBE), evolved from Smoluchowski's master equation describing particle coagulation [45], with different degrees of simplification. Analytical solutions to solve PBEs do not generally exist and the direct numerical integration is prohibitively expensive [46–48]. One approach to solving the PBE is the discretisation along an internal variable of the NDF into sections. The internal variable used is commonly describing the particle size only, e.g. via volume or mass [49], although other internal variables such as surface area or chemical composition may be taken into account [50]. The approach, in principle, renders the solution of the PBE numerically feasible and the development of such methods and their application to soot modelling has been pursued by Smooke et al. [51] amongst others. Kumar and Ramkrishna [16] developed a fixed sectional model preserving mass and number density, offering both numerical accuracy and speed. Bhatt and Lindstedt [15] and Lindstedt and Waldheim [13] developed the approach to model soot in a well-stirred/plug flow reactor configuration [17, 18] and for premixed laminar flames [52–54]. The stability of surface growth and oxidation terms was addressed via the 'two-point' and 'three-point' methods by Park and Rogak [31].

Instead of attempting to solve an approximation of the NDF directly, moment methods [46] transport a finite set of moments [50], making such approaches computationally less expensive. The method of moments with interpolative closure (MOMIC) [24] is using an interpolation approach based on the transported moments for closure of the moment equation. Quadrature based moment approaches reconstruct the NDF to solve the closure problem and a number of strategies for discrete (quadrature [56], direct quadrature [57], hybrid [58] and condi-

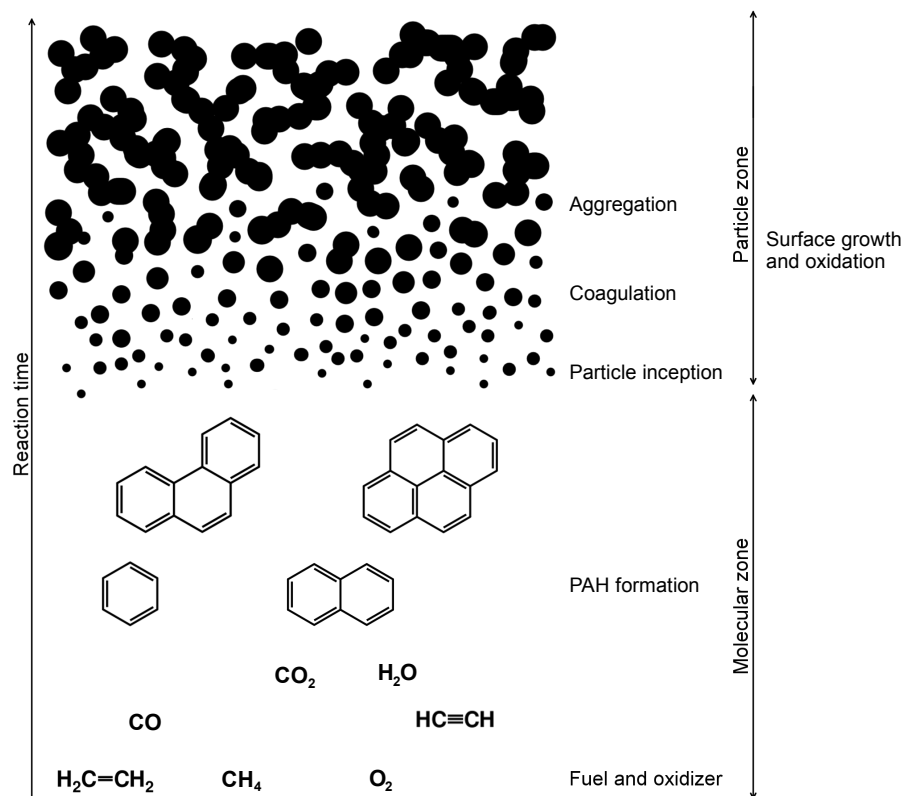


Figure 2.1: A scheme of the soot formation and oxidation model, based on Bockhorn [55]. Particle inception both via polycyclic aromatic hydrocarbons (PAHs) and an acetylene-based nucleation model is considered in this work.

tional quadrature [59] methods of moments) and continuous (extended conditional quadrature method of moments [60]) reconstruction have been developed. In two-equation type soot models [23, 27], equations for soot mass and particle number density are solved. The method is functionally equivalent to a moment approach solving for the zeroeth and first moments of the particle size distribution function only.

A particular issue with soot formation and oxidation in turbulent flames is that the chemistry tends to be slow compared to the majority of gas phase reactions. Accordingly, the need arises to solve additional transport equations for soot related properties (e.g. soot mass and number density) with, for example, soot treated as a perturbation upon the gas phase chemistry combined with a presumed PDF approach [61, 62]. Such approaches fail when a significant proportion of the available

carbon is converted to soot and also present problems due to the radiative heat loss effects typically associated with soot formation. Transported probability density function (PDF) methods offer the principal advantage of treating the highly non-linear chemical source terms occurring in turbulent combustion modelling without approximation [19], can be extended to Large Eddy Simulations (LES) [63], provide a direct coupling between gas and soot chemistries and can readily include enthalpy as part of the solved scalar space [30, 40]. In the current work, a transported PDF approach closed at joint scalar level is adopted requiring closure approximations only for turbulent transport in physical space and molecular mixing in composition space.

Figure 2.1 offers an overview of the processes considered in the soot model in this work. Incipient soot is formed via dimerisation of polycyclic aromatic hydrocarbons (PAHs) created from reactions in the gas phase. The requirement to include PAHs in the chemical reaction mechanism increases the size of the scalar space considerably, and an alternative nucleation model based on acetylene concentration is considered in the current work, as presented in Section 2.3. Colliding soot particles coagulate to initially near-spherical particles. As particle sizes increase, self-similar aggregates with a fractal morphology are formed, and both processes are considered in the context of three different particle dynamics models, introduced in Section 2.2. Finally, the surface of soot particles of any size may undergo reactions with species from the gas phase, adding or subtracting mass. The models considered for these growth and oxidation processes are introduced in Section 2.4 and Section 2.5, respectively.

2.2. Particle Dynamics

A fixed sectional approach is used with the mass (m) of the particles in each section given according to the recursive relation

$$m_{i+1} = f_s m_i, \quad (2.1)$$

where f_s is a spacing factor discussed further in Section 2.8. The approach is computationally efficient with soot mass assigned as the representative size variable. For a number of N_{bin} representative sizes, the corresponding population balance

equations for coagulation/aggregation are given by

$$\frac{dN_i}{dt} = \sum_{\substack{j,k \\ m_{i-1} \leq (m_j+m_k) \leq m_{i+1}}}^{k \leq j \leq i} \left(1 - \frac{\delta_{j,k}}{2}\right) \eta_{i,j,k} \beta_{j,k} N_j N_k - N_i \sum_{k=1}^{N_{\text{Bin}}} \beta_{i,k} N_k, \quad (2.2)$$

where N_i is the number concentration of the i th size class, $\beta_{j,k}$ the rate of collision of particles of size class j with class k and $\delta_{j,k}$ is the Kronecker delta. Newly formed particles are assigned to two adjacent bins, conserving any two general properties if new particles do not match any of the representative sizes exactly. The parameter $\eta_{i,j,k}$ is the fraction of a newly created particles assigned to size class i when two particles of classes j and k collide, hence assigning new particles to the adjacent bins as

$$\eta_{i,j,k} = \begin{cases} \frac{m_{i+1} - (m_j + m_k)}{m_{i+1} - m_i}, & m_i \leq (m_j + m_k) \leq m_{i+1} \\ \frac{m_{i-1} - (m_j + m_k)}{m_{i-1} - m_i}, & m_{i-1} \leq (m_j + m_k) \leq m_i. \end{cases} \quad (2.3)$$

The regime in which coagulation takes place may be characterised by the value of the Knudsen number

$$\text{Kn} = 2\lambda/d_i, \quad (2.4)$$

where λ is the gas mean free path and d_i is the particle diameter for a section i . The gas mean free path is defined as

$$\lambda = \frac{k_B T}{\sqrt{2} \pi d_i^2}, \quad (2.5)$$

with $k_B = 1.38 \cdot 10^{-23}$ J/K denoting the Boltzmann constant, d the molecular diameter, and T the temperature. In the current work, λ is approximated as the mean free path in air, scaled relative to the value $\lambda_{\text{air}}^0 = 6.6 \times 10^{-8}$ m at standard conditions $p^0 = 1.01325 \times 10^5$ Pa and $T^0 = 293.15$ K as

$$\lambda_{\text{air}} = \frac{p^0}{p} \frac{T}{T^0} \lambda_{\text{air}}^0. \quad (2.6)$$

For atmospheric pressure conditions with negligible mean pressure gradients, the pressure dependence is omitted from Eq. (2.6). Coagulation and aggregation of particles are considered in the limits of the free molecular regime characterised by $\text{Kn} \gg 1$ and of the continuum regime with $\text{Kn} \ll 1$, as well as the transition

regime [48]. The transition regime is here assumed to be within the boundaries $0.1 \leq \text{Kn} \leq 10$, with values of the Knudsen number above or below corresponding to the limit cases.

The rate constants for collisions of spherical particles in the three regimes are then given by Eqs. (2.7)–(2.9) [24, 64], where the collision frequency in the transition regime is approximated by the harmonic average of the values in the free molecular and continuum regimes.

$$\beta_{i,j}^{C,f} = C_a \left(\frac{3}{4\pi} \right)^{1/6} \left(\frac{6k_B T}{\rho_s} \right)^{1/2} \left(\frac{1}{v_i} + \frac{1}{v_j} \right)^{1/2} (v_i^{1/3} + v_j^{1/3})^2 \quad (2.7)$$

$$\beta_{i,j}^{C,c} = \frac{2k_B T}{3\mu_L} \left(\frac{C_i}{v_i^{1/3}} + \frac{C_j}{v_j^{1/3}} \right) (v_i^{1/3} + v_j^{1/3}) \quad (2.8)$$

$$\beta_{i,j}^t = \frac{\beta_{i,j}^f \beta_{i,j}^c}{\beta_{i,j}^f + \beta_{i,j}^c} \quad (2.9)$$

The superscript C denotes coagulation into spherical particles, f , c and t the free, continuum and transition regimes, respectively, v_i is the volume of a particle of size class i and d_i its diameter, $\rho_s = 1800 \text{ kg/m}^3$ is the density of soot, $k_B = 1.38 \cdot 10^{-23} \text{ J/K}$ the Boltzmann constant, T the temperature μ_L the laminar dynamic viscosity of the fluid, C_i the Cunningham slip correction factor given by Eq. (2.10) [64] and C_a is the van der Waals enhancement factor. Harris and Kennedy [65] calculated the van der Waals enhancement factor for soot particles of different sizes at a temperature of 1600 K using the method of Pailthorpe and Russel [66]. They evaluated C_a to approximately 2.4 for collisions between particles of a diameter of 1 nm, to 2.2 for two particles of 30 nm diameter, to approximately $C_a = 1$ for collisions of particles larger than that or for interactions of two particles with diameters of 1 nm and 30 nm ($C_a = 1.2$). It was found that the particle evolution of an aerosol calculated using the map of C_a created could be closely reproduced via a single value of $C_a = 2.2$ for all particle interactions. Lindstedt and Waldheim [13] used a value of $C_a = 3.0$, close to the recommendation by Harris and Kennedy [65], studying soot in laminar premixed stagnation flow flames [52–54] and the value has been the base for sectional model calculations in this work, with the sensitivity explored. In the context of the two-equation model, a value of $C_a = 9.0$ was proposed by Leung et al. [23], based on measurements of soot number density and mass fraction in laminar non-premixed flames. The value is

subject to the uncertainty in experimental data at the time. It was subsequently also applied to two-equation model and method of moments calculations of turbulent non-premixed flames by Lindstedt and Louloudi [28, 30], and is retained for the turbulent flame calculations in this work for consistency.

$$C_i = 1 + 1.257 \text{ Kn} \quad (2.10)$$

Aggregation (or agglomeration) is characterised by the creation of chain-like structures after collision of similarly sized primary particles, replacing coalescent growth in the limit of large mean particle diameters. There exists no satisfactory model describing the transition from coalescent growth to aggregation, and in the current work aggregation replaces coagulation if the diameter of either of the colliding particles surpasses $d_{prim} = 27.5$ nm, following Kazakov and Frenklach [48] who used 25 or 30 nm. The diameter of the fractal aggregates follows the fractal relationship of Eq. (2.11) based on the primary particle diameter d_p and the number of primary particles per aggregate N_p with a fractal dimension D_f :

$$d_c = d_{prim} N_p^{1/D_f} \quad (2.11)$$

A value of $D_f = 1.8$ [67] in continuity with previous work [13–15, 28, 30] is adopted here, close to the canonical range of 1.78 ± 0.1 for diffusion limited cluster aggregates (DLCAs) typically forming in aerosols [68]. Soot superaggregates with fractal dimension of 2.6 forming in laminar acetylene/diffusion flames alongside DLCAs with $D_f = 1.8$ [69] have been reported, as well as soot particles with values as low as $D_f = 1.20$ – 1.74 from in-cylinder measurements of diesel combustion [70]. While the choice of $D_f = 1.8$ in the current work is conventional, it therefore may require a review before the current model is applied to specific conditions outside of the scope of this work. Assuming identical mobility and collision diameters, aggregation rates in the two limiting regimes are given as [71],

$$\beta_{i,j}^{A,f} = C_a \left(\frac{\pi k_B T}{2} \right)^{1/2} \left(\frac{1}{m_i} + \frac{1}{m_j} \right)^{1/2} (d_{c,i} + d_{c,j})^2 \quad (2.12)$$

$$\beta_{i,j}^{A,c} = \frac{2k_B T}{3\mu_L} \left(\frac{C_i}{d_{c,i}} + \frac{C_j}{d_{c,j}} \right) (d_{c,i} + d_{c,j}) \quad (2.13)$$

where the superscript A denotes aggregation involving chain-like fractal aggregates. Both terms are combined in the transition regime via Eq. (2.9).

The above approach is used to evaluate the impact of simplified soot nucleation and revised oxidation rates in the context of the sectional soot model. In two-equation approaches to soot modelling [23, 27] a single mean particle size is adopted and the evolution of the soot particle number density is calculated by integration of Eq. (2.14), corresponding to the equation for the zeroeth moment of the PSDF in method of moments type approaches.

$$\frac{d[\rho N_s]}{dt} = R_N' - R_{CIA} \quad (2.14)$$

The total number density (in particles/kg-mixture) is denoted by N_s , the sum of all particles in all size classes:

$$N_s = \sum_{i=1}^{\infty} N_i . \quad (2.15)$$

The nucleation term (R_N') is discussed below with coagulation/aggregation (R_{CIA}) defined as,

$$R_{CIA} = \frac{1}{2} \sum_{i=1}^{\infty} \sum_{j=1}^{\infty} \beta_{ij} [\rho N_i] [\rho N_j] \quad (2.16)$$

$$= \frac{1}{2} \beta [\rho N_s]^2 \quad (2.17)$$

where $[\rho N_i]$ is the number density (particles/m³) of particles of size class i and β_{ij} the collision frequency with Eq. (2.16) simplified via Eq. (2.15) under the assumption of a nearly monodisperse and sufficiently diluted system [72].

The mean particle diameter d_p is calculated via Eq. (2.18) as a function of the soot mass fraction Y_s , the number density N_s and the gas (ρ) and soot (ρ_s) densities [27].

$$d_p = \left(\frac{6 \rho}{\pi \rho_s} \frac{Y_s}{[\rho N_s]} \right)^{1/3} \quad (2.18)$$

Similar to the sectional model, the collision frequency β is obtained in the limits of the free molecular and continuum regimes, and in the transition regime via Eq. (2.9). In this context, the Knudsen number is evaluated in terms of the mean particle diameter as

$$\text{Kn} = 2\lambda/d_p . \quad (2.19)$$

The superscript notation from Eqs. (2.7)–(2.9) and (2.12)–(2.13) is retained, with

the subscript ij omitted due to the adoption of a single mean particle size. Under the assumption of spherical particles and monodispersity, the collision frequency in the free molecular regime ($\text{Kn} > 10$) is obtained as [28, 72]

$$\beta^{C,f} = 4C_a \left(\frac{6k_B T}{\rho_s} \right)^{1/2} d_p^{1/2}, \quad (2.20)$$

where the value $C_a = 9$ was retained to provide continuity with previous work [28, 30]. This high value was originally chosen to reproduce the measured evolution of the (mean) soot particle number density in a set of laminar diffusion flames [23, 27]. In the continuum regime ($\text{Kn} < 0.1$), assuming validity of the Stokes-Einstein equation for the diffusion constant and monodispersity ($i = j$), the collision frequency can be expressed as [28, 72]

$$\beta^{C,c} = \frac{8k_B T}{3\mu_L} C_i. \quad (2.21)$$

The aggregate diameter d_c for large, chain-like fractal aggregates is defined by Eq. (2.11). The number of primary particles per aggregate N_p and the total mass of the aggregate m_A are related via Eqs. (2.22)–(2.23), where M_g denotes the molar mass of the gas mixture and $N_A = 6.022 \times 10^{26} \text{ kmol}^{-1}$ is Avogadro's number [28].

$$N_p = \frac{N_s M_g}{N_A} \quad (2.22)$$

$$m_A = \frac{\pi}{6} \rho_s d_p^3 N_p \quad (2.23)$$

The collision rate for aggregation in the free molecular and continuum regimes can then be obtained for a monodisperse system as [28, 71]:

$$\beta^{A,f} = 4C_a (\pi k_B T)^{1/2} \frac{d_c^2}{m_A^{1/2}}, \quad (2.24)$$

$$\beta^{A,c} = \frac{8k_B T}{3\mu_L} C_i. \quad (2.25)$$

As for the sectional model, the collision rate in the transition regime for both coagulation and aggregation is obtained as a harmonic average of the rates in the free

molecular and continuum regimes:

$$\beta^t = \frac{\beta^f \beta^c}{\beta^f + \beta^c} \quad (2.26)$$

In addition to the integration of Eq. (2.14), the particle dynamics are also modelled via the method of moments with interpolative closure defined by Frenklach [24] and as used by Lindstedt and Louloudi [28, 30]. In this approach, Smoluchowski's equation is rewritten in terms of the r -th order moment of the PSDF defined as [47]

$$M_r = \sum_{i=1}^{\infty} m_{M,i}^r [\rho N_i] , \quad (2.27)$$

where $m_{M,i}^r$ is the mass in number of carbon atoms and N_i the number density (particles/kg-mixture) of the soot particles of size class i . The resulting set of equations may then be extended to account for nucleation, oxidation and coalescence or aggregation, such that the evolution of the moments is hence obtained as [30, 47]

$$\begin{aligned} \frac{dM_0}{dt} &= R_{N,0} - R_{C/A,0}, \\ \frac{dM_1}{dt} &= R_{N,1} + R_{G,1} - R_{O,1}, \\ \frac{dM_2}{dt} &= R_{N,2} + R_{C/A,2} + R_{G,2} - R_{O,2}, \\ &\dots \\ \frac{dM_r}{dt} &= R_{N,r} + R_{C/A,r} + R_{G,r} - R_{O,r}, \end{aligned} \quad (2.28)$$

where the subscript N indicates nucleation, C/A coagulation/aggregation, G mass growth and O oxidation. The solution obtained for the first four moments (M_0 – M_3) is here used as an alternative to the integration of Eq. (2.14), with the terms in Eq. (2.28) as defined by Lindstedt and Louloudi [28, 30]. In the context of two-equation models, the evolution of the soot mass is represented by an equation corresponding to the first moment (M_1), as discussed below, with M_2 and M_3 neglected.

2.3. Nucleation

The transported PDF method provides the full turbulence-chemistry interactions associated with the applied chemical mechanism. Accordingly, simplifications to the nucleation step are highly desirable as the PAH chemistry inevitably leads to a significant increase in the size of the scalar space. Past work [23, 27, 30] has featured nucleation steps formulated as first order in the acetylene concentration via Eqs. (2.29)–(2.30),



$$R_N = k_N(T) [\text{C}_2\text{H}_2] \quad (2.30)$$

where C_{soot} denotes carbon atoms contributing to the soot particle mass. The reaction is assumed irreversible with a reduction in soot mass caused by oxidation and a reduction in the particle number density caused by coagulation/agglomeration. Equation (2.29) also gives rise to the source term in the number density equation (Eq. (2.31)), where C_{min} is the number of carbon atoms in an incipient soot particle.

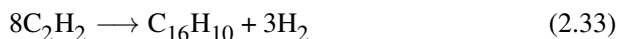
$$R_N' = 2N_A k_N'(T) [\text{C}_2\text{H}_2] \quad (2.31)$$

$$k_N'(T) = k_N(T)/C_{\text{min}} \quad (2.32)$$

The parameter C_{min} can be interpreted as providing a scaling for the source term in the particle number density equation that improves consistency of predictions of both soot mass and number density within the framework of simplified models. Leung et al. [23] and Fairweather et al. [61] assumed $C_{\text{min}} = 100$, while in subsequent work by Lindstedt [27] and Lindstedt and Louloudi [30] the parameter was set to correspond to a C_{60} shell ($C_{\text{min}} = 60$), which has been shown to be the most common of the lower PAH ions [73] in premixed laminar benzene-oxygen flames. To preserve continuity with these studies, the latter value has been retained here. The link of number density to the soot mass equation is via the particle size in growth and oxidation rate expressions.

Modelling nucleation in the absence of reliable compact reduced models for PAH molecules relies upon a correlation between PAH and C_2H_2 concentrations. Sunderland et al. [74], Lin et al. [75], and Sunderland and Faeth [76] measured soot nucleation and growth for laminar diffusion flames across a wide range of condi-

tions and fuels and proposed nucleation rates based on a first order correlation with the acetylene concentration. Louloudi [28] and Lindstedt and Louloudi [30] modelled nucleation in the turbulent ethylene diffusion flames of Kent and Honnery [32] and Coppalle and Joyeux [33] using a reaction step previously validated in laminar non-premixed methane, ethylene, propane flames [23, 27]. The current work compares these nucleation rates with a more accurate formulation based on pyrene concentration using the detailed chemistry of Lindstedt and Waldheim [13]. The impact on the evolution of the PSD is assessed against the experimental data obtained by Lenhert and Manzello [18] in a WSR/PFR reactor configuration by using a sectional model [13, 15]. In sectional models, the particle number density and soot mass are intrinsically linked via the particle mass assigned to each section. The nucleation step accordingly represents both a source of soot mass and particle number density in the smallest section. For consistency, soot nucleation is treated via Eq. (2.33) with the incipient soot particles assigned the molecular mass and thermodynamic properties of pyrene.



For a given nucleation rate, reactions Eqs. (2.29) and (2.33) yield approximately the same mass of soot per mole of C_2H_2 ($2M_C \approx M_{\text{C}_{16}\text{H}_{10}}/8$). By contrast, in the two-equation model, the reaction rate constant in the number density source term is scaled relative to that of the mass source term via $k'_N = k_N/C_{min}$ and the different stoichiometric coefficients in Eq. (2.29) and (2.33) are not balanced by the difference in molar mass of soot. As a result, for any given rate of reaction, the number density source term in the two-equation model yields $2/C_{min}$ moles of soot per mole of C_2H_2 , whereas in the sectional model Eq. (2.33) gives $1/8$ moles of incipient soot particles, an increase by a factor of 3.75. The nucleation rates in the sectional model calculations have been scaled accordingly to ensure consistency with the two-equation and method of moments models in terms of the soot particle number density source term.

Alternative formulations of the nucleation step are possible. In the approach according to Equation (2.34), the nucleation step is considered to form incipient soot particles with the properties of naphthalene. The model is considered in the current work, and the scaling applied for consistency with the two-equation model is accordingly adapted to a factor of $60/(2 \cdot 5) = 6.0$ where appropriate. The thermodynamic properties of the soot sections are set to those of either pyrene or

naphthalene, depending on whether the nucleation step in Eq. (2.33) or Eq. (2.34) is used.



2.4. Surface Growth

Particle growth due to the adsorption of C_2H_2 on the surface of soot particles is typically the dominant mechanism for increasing soot mass and is modelled via a one-step growth reaction [23, 27, 30]:



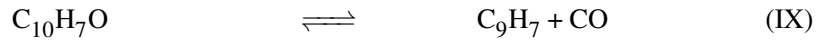
Soot mass growth via acetylene is approximately a first order reaction [77] and a proportionality to some function of $f(A_s)$ of the total external surface area of soot is assumed:

$$R_G = k_G(T)f(A_s) [\text{C}_2\text{H}_2] \quad (2.36)$$

The soot mass growth step discussed above can be augmented to approximately take into account the effects of the chemical environment of the soot particle, e.g. via the ubiquitous hydrogen-abstraction/acetylene-addition (HACA) sequence [78] first introduced by Frenklach and Wang [79]. The current work features a closed, systematically reduced, analogy of the soot surface chemistry by Lindstedt and Louloudi [28, 30] based on naphthalene, previously evaluated in the context of a plug flow reactor [80] and for the turbulent diffusion flames of Kent and Honnery and Coppalle and Joyeux [32, 33], and applied to model soot growth as part of a sectional approach in premixed stagnation flow flames [13], as well as non-premixed laminar flames and a WSR/PFR reactor system [14].

The soot surface chemistry model by Lindstedt and Louloudi [28, 30] based on naphthalene is shown in Eqs. (I)-(X). The corresponding rate constants are presented in Table 2.1 and the structures of the aromatic species are shown in Ta-

ble A.1 in the Appendix.



Reaction (X) corresponds to the soot mass growth step expressed as first order in concentrations of both acetylene and naphthyl radicals in Eq. (2.37).

$$R_G = k_X^f(T) [\text{C}_{10}\text{H}_7] [\text{C}_2\text{H}_2] \quad (2.37)$$

The concentration of $[\text{C}_{10}\text{H}_7]$ in Eq. (2.37) is obtained via the application of truncated steady-state approximations involving reactions (I)-(X) [28] resulting in Eq. (2.39).

$$\mathcal{L}([\text{C}_{10}\text{H}_7]) = \omega_I^r + \omega_{II}^r + \omega_{IV}^f + \omega_V^r + \omega_{VI}^r - \omega_I^f - \omega_{II}^f - \omega_{IV}^r - \omega_V^f - \omega_{VI}^f - \omega_X^f \quad (2.38)$$

$$[\text{C}_{10}\text{H}_7] = \frac{K_1 [\text{C}_{10}\text{H}_8] + K_2 [\text{C}_{10}\text{H}_7\text{O}] + K_3 [\text{C}_{10}\text{H}_7\text{OO}]}{K_4} \quad (2.39)$$

where

$$K_1 = k_I^r + k_{II}^r [\text{H}] + k_{IV}^f [\text{OH}] \quad (2.40)$$

$$K_2 = k_V^r [\text{O}] \quad (2.41)$$

$$K_3 = k_{VI}^r \quad (2.42)$$

$$K_4 = k_I^f [\text{H}] + k_{II}^f [\text{H}_2] + k_{IV}^r [\text{H}_2\text{O}] + k_V^f [\text{O}_2] + k_{VI}^f [\text{O}_2] + k_X^f [\text{C}_2\text{H}_2] \quad (2.43)$$

The concentrations $[C_{10}H_7O]$ and $[C_{10}H_7OO]$ are likewise obtained via steady-state approximations:

$$\mathcal{L}([C_{10}H_7O]) = \omega_{II}^f + \omega_V^f - \omega_{III}^r - \omega_V^r - \omega_{IX}^f \quad (2.44)$$

$$[C_{10}H_7O] = \frac{K_5[C_{10}H_7] + K_6[C_{10}H_8]}{K_7} \quad (2.45)$$

$$\mathcal{L}([C_{10}H_7OO]) = \omega_{VI}^f - \omega_{VI}^r - \omega_{VII}^f - \omega_{VIII}^f \quad (2.46)$$

$$[C_{10}H_7OO] = \frac{K_8[C_{10}H_7]}{K_9} \quad (2.47)$$

where

$$K_5 = k_V^f [O_2] \quad (2.48)$$

$$K_6 = k_{III}^f [O] \quad (2.49)$$

$$K_7 = k_{III}^r [H] + k_V^r [O] + k_{IX}^f \quad (2.50)$$

$$K_8 = k_{VI}^f [O_2] \quad (2.51)$$

$$K_9 = k_{VI}^r + k_{VII}^f + k_{VIII}^f \quad (2.52)$$

Substitution of Eqs. (2.39), (2.45) and (2.47) into (2.37) then gives

$$R_G = k_X^f(T) K_{PAH} [C_{10}H_8] [C_2H_2], \quad (2.53)$$

where the $K_{PAH} = [C_{10}H_7]/[C_{10}H_8]$ includes the terms K_1-K_9 from the steady-state approximation steps:

$$K_{PAH} = \frac{K_1 K_7 + K_2 K_6}{K_4 K_7 K_9 - K_2 K_5 K_9 - K_3 K_7 K_8} K_9 \quad (2.54)$$

The emerging naphthalene concentration is approximated as a function of the maximum number of active sites on the soot surface $\chi_{s-h} \approx 2.32 \times 10^{19}$ sites / (m²-soot surface) [27, 47] and the soot surface area A_s (via Eq. (2.68)) as

$$[C_{10}H_8] = \alpha_s A_s \frac{\chi_{s-h}}{N_A}, \quad (2.55)$$

where $N_A = 6.022 \times 10^{26}$ kmol⁻¹ is Avogadro's number, A_s is the total soot particle surface area [28], and α_s is a modelling parameter expressing the fraction of reaction sites on the soot surface available for reaction. A strong sensitivity

Table 2.1: Reaction rate constants for the PAH analogy of soot surface chemistry [80] presented in the form $A_i \alpha_i T^{\beta_i} \exp(-E_i/RT)$. Units are in K, kmol, m³ and s.

Step	A_i	α_i	β_i	E_i/R
I	7.83×10^{10}	1	0	0
II	4.44×10^1	1	2.43	3,158
III	2.5×10^{10}	1	0	2,347
IV	1.7×10^5	1	1.42	729
V	2.15×10^{10}	1	0	3,076
VI	2.5×10^9	1	-0.15	80
VII	2.272×10^8	1	0	0
VIII	2.272×10^8	1	0	0
IX	1.8×10^{11}	1	0	22,062
X	3.57×10^{21}	1	-3.176	7,471

has been found in previous work [27, 30, 47, 78, 81]. Lindstedt and Louloudi [30] presented results for $\alpha_s = 0.75$ and 1.00 in their study of the turbulent ethylene diffusion flames of Kent and Honnery [32] and Coppalle and Joyeux [33]. Kazakov et al. [81] proposed a correlation for α_s in laminar premixed ethylene/air flames as a function of the maximum flame temperature T_{max} , as

$$\alpha_s = \tanh(8168/T_{max} - 4.57 + 1)/2, \quad (2.56)$$

spanning values in the range $0.2 \leq \alpha_s \leq 0.6$ for the flames studied.

The final expression for growth via the surface chemistry model analogous to Eq. (2.36) is hence given by Eq. (2.57), where $k_X^f(T)$ is the acetylene addition rate and χ_s expresses the number of sites available for reaction on the surface of soot particles.

$$R_G = k_X^f(T) \chi_s A_s [\text{C}_2\text{H}_2] \quad (2.57)$$

$$\chi_s = K_{PAH} \alpha_s \frac{\chi_s - h}{N_A} \quad (2.58)$$

2.5. Oxidation

The oxidation of soot is assumed to take place via irreversible reactions with OH, O and O₂ as described by Eqs. (2.59)–(2.61).



Guo et al. [82] examined twelve experimental studies [83–95] reporting soot oxidation rates, temperature, OH and O₂ concentration, comprising a total of 160 measurements of soot oxidation rates in premixed flames, diffusion flames, thermogravimetric analyzers (TGAs) and flow reactors for a wide range of conditions. Optimized reaction rate expressions for oxidation of soot by OH and O₂ were developed, featuring a collision efficiency of 0.10 for soot oxidation by OH and an activation energy of 195 kJ/mol for oxidation by O₂. The latter value is much higher than that suggested by Roth et al. [96], but comparatively close to the value of 164 kJ/mol used by Lindstedt [27]. In the current work, the reaction rate constants of Lindstedt and Louloudi [28, 30] are compared with the updated suggestion for the collision efficiency of OH from Guo et al. [82] and the rate with the higher activation barrier [27]. The combined reaction rate source term is given by Eq. (2.62), with oxidation being considered proportional to the function $f(A_s)$ discussed in Section 2.6.

$$R_O = \left(k_{\text{OH},1}(T) [\text{OH}] + k_{\text{O},1}(T) [\text{O}] + k_{\text{O}_2,1}(T) [\text{O}_2] \right) f(A_s) \quad (2.62)$$

In order to account for the fact that the reaction rates in Eq. (2.62) used in previous work [15, 30] were derived based on the oxidation of carbon black [96], not taking into account that the higher H/C ratio in soot particles will lead to increased reactivity. Pyrene, e.g., has a H/C ratio of 0.625, naphthalene of 0.8 and carbon black of 0.006 [97]. Lindstedt and Waldheim [13, 14] extended the above model by introducing a further term expressing soot oxidation by O₂ as a function of the number of active sites on the soot surface. Analogous to the PAH surface growth model, the expression is given in Eq. (2.63), where χ_s and $k_{\text{O}_2,PAH} = k_V^f$

are defined in Eq. (2.57) and Table 2.1.

$$R_{O_2,PAH} = k_V^f(T)\chi_s A_s [C_2H_2] \quad (2.63)$$

2.6. Surface Area Dependence of Growth and Oxidation: The Functional Form of $f(A_s)$

The function $f(A_s)$ expresses the relation of the growth and oxidation terms to the surface area of soot A_s . One of the simplest assumptions is that of proportionality of soot growth and oxidation to the number density of soot particles $[\rho N_s]$ (in particles/m³-mixture), which is equivalent to the ratio of the total soot surface A_s (in m²/m³-mixture) to the surface area of an individual soot particle A_p (in m²) [27, 28]:

$$f(A_s) = [\rho N_s] \quad (2.64)$$

$$= A_s/A_p \quad (2.65)$$

Among the most common assumptions is the proportionality to the total soot surface A_s [27, 28]:

$$f(A_s) = A_s \quad (2.66)$$

Further, a square-root dependence on A_s was used in the original work on the two-equation model by Leung et al. [23]:

$$f(A_s) = \sqrt{A_s} \quad (2.67)$$

In the turbulent flame calculations in this work, a single mean particle size is assumed, and the total surface is calculated under the assumption of spherical particles and, disregarding any effect of soot porosity [98, 99], via Eqs. (2.68)–(2.69) and Eq. (2.18).

$$A_s = A_p [\rho N_s] \quad (2.68)$$

$$A_p = \pi d_p^2 \quad (2.69)$$

For the sectional model, Eq. (2.66) is adopted, where the A_s is the total surface area associated with a particle size class and growth and oxidation are calculated

for all soot sections individually, with growth modelled via Eq. (2.57).

2.7. Numerical Treatment of Surface Growth and Oxidation in the Sectional Model

The 'two-point' and 'three-point' fixed numerical methods for the treatment of soot surface growth and oxidation proposed by Park and Rogak [31] have been implemented in the current sectional model [15]. In the 'two-point' method, particles subject to growth or oxidation are assigned to two adjacent bins,

$$\frac{dN_i}{dt} = \frac{I_{i-1}N_{i-1}}{m_i - m_{i-1}} - \frac{I_i N_i}{m_{i+1} - m_i}, \quad (2.70)$$

$$\frac{dN_i}{dt} = \frac{I_i N_i}{m_i - m_{i-1}} - \frac{I_{i+1} N_{i+1}}{m_{i+1} - m_i}, \quad (2.71)$$

where Eq. (2.70) describes growth, Eq. (2.71) oxidation, and $I_i = \frac{dm_i}{dt}$ is the surface growth or oxidation rate of the i th soot section. The method preserves the particle number and mass, but tends to overestimate higher order moments due to numerical diffusion [31], that can be reduced by decreasing the section spacing. The modified 'three-point' method proposed by Park and Rogak [31] addresses this problem, while also improving stability over the 'three-point' method previously introduced by Hounslow et al. [100]. It is given as

$$\frac{dN_i}{dt} = \frac{A_{i-1}I_{i-1}N_{i-1}}{m_{i-1}} + \frac{B_i I_i N_i}{m_i} + \frac{C_{i+1}I_{i+1}N_{i+1}}{m_{i+1} - m_{i+1}}. \quad (2.72)$$

The coefficients at the boundaries $i = 1$ and N_{bin} are defined as

$$A_1 = \frac{1}{f_s - 1}, \quad (2.73)$$

$$B_1 = \frac{-1}{f_s - 1}, \quad (2.74)$$

$$C_1 = 0, \quad (2.75)$$

$$A_{N_{bin}} = 0, \quad (2.76)$$

$$B_{N_{bin}} = \frac{f_s}{f_s - 1}, \quad (2.77)$$

$$C_{N_{bin}} = \frac{-f_s}{f_s - 1}, \quad (2.78)$$

and those for the interior sections $2 \leq i \leq N_{bin} - 1$ as

$$A_i = \frac{f_s - B_i(f_s - 1)}{f_s^2 - 1}, \quad (2.79)$$

$$B_i = \begin{cases} \frac{f_s}{f_s - 1} \operatorname{erf} \left(\frac{1}{8} \frac{d \ln N_i}{d \ln m_i} \right), & \frac{d \ln N_i}{d \ln m_i} \leq 0 \\ \frac{1}{f_s - 1} \operatorname{erf} \left(\frac{1}{8} \frac{d \ln N_i}{d \ln m_i} \right), & \frac{d \ln N_i}{d \ln m_i} > 0, \end{cases} \quad (2.80)$$

$$C_i = -(A_i + B_i). \quad (2.81)$$

The fraction occurring as the first argument of the error function in the definition of B_i in Eq. (2.79) was changed to $1/8$ in previous work [14, 101], improving stability of the 'three-point' method. Nevertheless, Bhatt and Lindstedt [15] reported instabilities of the 'three-point' method under lean conditions with strong soot oxidation. To avoid instability issues, calculations in the current investigation are therefore performed via the 'two-point' method.

2.8. Sectional Model: Properties of Soot Sections

The mass of the particles in each soot section is given by the recursive relation expressed in Eq. (2.1). Equivalently, the molar mass of the soot sections is given as

$$M_{i+1} = f_s M_i. \quad (2.82)$$

The spacing factor f_s determines the resolution of the solved PSD and, via the total number of bins N_{bin} , the particle size range covered. In conjunction with the 'two-point' method, Park and Rogak [31] showed that $f_s = 2$ yields a sufficiently accurate solution if particle coagulation as well as growth are considered, and noted a significant increase in computation time for smaller values due to an increase in the stiffness of the problem. In this work, to decrease the numerical diffusion of the method and in line with previous work [13–15], a value of $f_s = 1.5$ is adopted, leading to a maximum particle size of 390 nm using 43 bins, and covering a sufficient size range for the calculations in the WSR/PFR system in Chapter 3. For the calculations of PSDs the Sandia turbulent jet flame in Chapter 6, residence times are considerably higher, and an extension of the particle size range is required. A fixed value of $f_s = 1.5$ was therefore used for particles up to a size of 100 nm, and the value was linearly relaxed for larger particles up to $f_s = 2$ for the largest bin.

Using this strategy, a range up to $120 \mu\text{m}$ is covered using 61 bins, while the high resolution in the crucial region $d_p < 100 \text{ nm}$ is retained.

In the context of the sectional soot model, nucleation is modelled as formation of dimers from two PAH molecules, necessarily included in the chemical reaction model. In the current work, nucleation via either naphthalene (A_2) or pyrene (A_4) is considered, with soot nucleation in the model occurring directly by formation of naphthalene/pyrene in the gas phase. The standard atomic weight of the zeroeth and first bin are then given by the nucleating species and the corresponding primer, as either of the following:

$$m_0 = m_{A_2} = 128.174 , \quad (2.83)$$

$$m_0 = m_{A_4} = 202.256 , \quad (2.84)$$

$$m_1 = 2m_0 . \quad (2.85)$$

Particles in the final two soot sections are prevented from taking part in aggregation, with their mass set to:

$$m_{N_{bin-1}} = 2m_{N_{bin-2}} , \quad (2.86)$$

$$m_{N_{bin}} = 3m_{N_{bin-2}} . \quad (2.87)$$

Following previous work [13, 15], the corresponding diameters of the nucleating species are approximated via the carbon–carbon bond lengths of naphthalene (A_2) and pyrene (A_4) [102] as either of the following:

$$d_0 = d_{A_2} = 0.28 \text{ nm} , \quad (2.88)$$

$$d_0 = d_{A_4} = 0.38 \text{ nm} . \quad (2.89)$$

Due to the reduced size of the incipient particles for nucleation via naphthalene, the maximum particle diameters of the grid discussed above reduce slightly to 280 nm and $90 \mu\text{m}$ for 43 and 61 bins, respectively. In the limit of small particles, soot particles are represented by perfect spheres, and the cross-sectional area A_i and volume v_i of particles in the i th section are hence obtained from the diameter

d_0 and mass m_0 of the zeroeth section as:

$$d_i = d_0 \left(\frac{m_i}{m_0} \right)^{1/3}, \quad (2.90)$$

$$A_i = \pi d_i^2, \quad (2.91)$$

$$v_i = \frac{\pi}{6} d_i^3. \quad (2.92)$$

For diameters larger than a selected primary particle size diameter, here around 25 nm, soot particles are represented by chain-like structures following a fractal relationship with $D_f = 1.8$. The properties of these fractal aggregates are calculated in relation to the mass (m_{prim}) and diameter (d_{prim}) of a primary particle, based on Eq. (2.90):

$$N_p = \left(\frac{m_i}{m_{prim}} \right), \quad (2.93)$$

$$d_i = d_{prim} N_p^{1/D_f}, \quad (2.94)$$

$$A_i = \pi d_{prim}^2 N_p, \quad (2.95)$$

$$v_i = \frac{\pi}{6} d_{prim}^3 N_p. \quad (2.96)$$

2.9. Chemical Reaction Model

The detailed reaction model used in the context of WSR/PFR calculations is that of Lindstedt and Waldheim [13] described in detail in the PhD thesis of Waldheim [14]. It is based on a combination of the model of Wang and Frenklach [103] for higher PAHs with the indene and cyclopentadiene chemistry by Lindstedt et al. [101] and Robinson and Lindstedt [104]. The complete gas phase reaction model includes 358 species up to pyrene and 1789 reactions.

For all turbulent flame calculations in this work, the reduced reaction model for the gas phase chemistry by Lindstedt and Louloudi [28, 30, 105] is used. It is based on the systematically reduced 7-step model for the H/N/O system by Lindstedt and Selim [106] updated to include the C chemistry [107, 108], with N_2 considered inert and hence removed from the model. It features 144 reactions, 15 solved (H, O, OH, HO_2 , H_2O , H_2 , O_2 , CO, CO_2 , CH_3 , CH_4 , C_2H_2 , C_2H_4 , C_2H_6 , and N_2) and 14 steady-state species (C, CH, 1CH_2 , 3CH_2 , CHO, CH_2OH , CH_3O , C_2 , C_2H , C_2H_3 , C_2H_5 , C_2HO , C_2H_2O , and CH_2O).

3. Soot Particle-Size Predictions in a Premixed Reactor Configuration

3.1. Experimental Configuration and Model

The uncertainties in the nucleation rate of soot are considerable and depend on the flame configuration [27, 74–76, 109]. In this chapter the sensitivity of an acetylene based soot nucleation model to nucleation rates is assessed by comparing computed soot particle size distributions (PSDs) in the NIST combined well-stirred and plug flow reactor (WSR/PFR) configuration of Manzello et al. [17, 18].

The WSR/PFR reactor configuration of Manzello et al. [17, 18] features a plug flow reactor connected to the outlet of a well-stirred reactor. The setup has been used to study growth of PAHs and soot inception by measuring soot particle size distributions (PSDs) [17, 18] under fuel-rich conditions. The resulting data is suitable for the validation of soot models aimed at reproducing PSDs under premixed conditions. Calculations are here carried out under sooting conditions for a mixture of ethylene and nitrogen/oxygen with mole fractions corresponding to air at $\Phi = 2.0$, an air flow rate of 175 SLPM, and with a temperature of 1723 K in the WSR, as reported by Lenhert et al. [18]. Additional fuel can be injected at the interface between the two reactors, and the formation of soot under nominally non-sooting conditions from PAHs introduced into the system has been studied [14, 18]. The PFR features four sampling ports, spaced 152 mm apart, and measures 700 mm in length and 51 mm in diameter. The temperature profile imposed in the PFR is based on the interpolation of experimental data [14, 18] as 1420 K between the inlet and Port 1 at axial position $x = 152$ mm, and decreasing linearly with distance to Port 3 at $x = 456$ mm. Residence times in the WSR and PFR part are approximately 11 and 18 ms [15, 17, 18].

The gas phase chemistry is modelled via the detailed chemical reaction model by Lindstedt and Waldheim [13, 14], as outlined in Section 2.9, and soot is calculated using the sectional soot model described in Chapter 2, permitting the com-

Table 3.1: Reaction rate constants for soot nucleation via Eq. (2.29) presented in the form $k_{N,i} = A_i \exp(-E_i/RT)$. Units are in K, kmol, m³ and s.

k_i	A_i	α_i	β_i	E_i/R	Source
$k_{N,1}$	6.30×10^3	1	0	21,000	Lindstedt [27]
$k_{N,2}$	3.79×10^1	1	0	17,500	Sunderland and Faeth [76]
$k_{N,3}$	6.30×10^1	1	0	21,000	Current work
$k_{N,4}$	3.78×10^1	1	0	21,000	Current work

Table 3.2: Reaction rate constants for soot growth and oxidation in Eqs. (2.35) and (2.59)-(2.61) presented in the form $A_i \alpha_i T^{\beta_i} \exp(-E_i/RT)$ [27, 28, 96]. Units are in K, kmol, m³ and s.

k_i	A_i	α_i	β_i	E_i/R
$k_{G,2}$	3.57×10^{21}	1	-3.176	7,471
k_O	9.09	0.2	1/2	0
$k_{OH,1}$	8.82	0.05	1/2	0
$k_{O_2,1}$	6.43	0.723	1/2	11,250
$k_{OH,2}$	8.82	0.10	1/2	0
$k_{O_2,2}$	6.43	116	1/2	19,680
$k_{O_2,PAH}$	2.15×10^{10}	1	0	3,076

parison of calculated PSDs to experimental data. Soot nucleation is modelled by the acetylene based reaction in Eq. (2.33), forming soot particles based on the size and with the thermodynamical properties of pyrene, although nucleation via Eq. (2.34) into naphthalene is also evaluated. The nucleation rates $k_{N,1}$ by Lindstedt [27], $k_{N,2}$ by Sunderland and Faeth [76], as well as the rates $k_{N,3}$ and $k_{N,4}$ are evaluated, as shown in Table 3.1. The nucleation model by Bhatt and Lindstedt [15], creating soot via the formation of pyrene from the gas phase is considered for comparison purposes. The soot oxidation rates k_O , $k_{OH,1}$, $k_{O_2,1}$ stated in Table 3.2 are retained from previous work [28, 30], and an updated set k_O , $k_{OH,2}$, $k_{O_2,2}$ taking into account recent findings by Guo et al. [82] as discussed in Section 2.5 is evaluated. Growth is modelled via the PAH analogy based surface chemistry model by Lindstedt and Louloudi [30], with the acetylene addition rate $k_{G,2} = k_X^f$ and the soot surface area evaluated based on the individual soot sections. In their modelling study of the NIST reactor system, Bhatt and Lindstedt [15] evaluated the surface reactivity parameter α_s via the correlation by Kazakov et al. [81] based on the maximum flame temperature of laminar premixed flames, shown in Eq. (2.56). T_{max} was set to the temperature in the WSR, and the constant 4.57 was adapted to 5.74 to account for experimental differences [15], giving $\alpha_s \approx 0.12$ for $T_{max} = T_{WSR} = 1723$ K for the case considered here. Studying the NIST reactor

system under non-sooting conditions at $\Phi = 1.8$ with injection of aromatics as secondary fuel at the PFR inlet [18], Waldheim [14], on the other hand, used $\alpha_s = 0.4$, and reported only a moderate sensitivity in the range 0.0–0.6. Instead of adopting a single residence time, residence time distributions were assumed in the WSR to study the impact of non-perfect mixing. Considerable differences in the growth and oxidation models exist between each of these studies and the current work. There is a lack of a generally accepted physical model for the surface reactivity parameter, and a suitable constant value of α_s across different experimental configurations. The sensitivity to α_s in the context of the current model is explored below.

3.2. Results and Discussion

Measured [18] and predicted soot particle size distributions (PSDs) obtained with the sectional model in the WSR and at Ports 1 and 3 of the PFR are presented in Fig. 3.1. Soot oxidation was modelled via the updated rates (k_O , $k_{OH,2}$, $k_{O_2,2}$). Predictions obtained using the pyrene based nucleation model by Lindstedt and Waldheim [13] overall agree well with the measurements for a value of the surface reactivity parameter $\alpha_s = 0.85$, with the peaks of the PSD at PFR Ports 1 and 3 moderately underpredicted. The measured PSDs display a discontinuous gradient at $d_p \approx 25$ nm, and noticeably flatten for larger particle sizes. While this feature is not discussed by Lenhart and Manzello [18], its location coincides with the formation of the smallest fractal aggregates with Hanisch et al. [110] reporting primary particle size diameters around 30 nm. Following Kazakov and Frenklach [48], a primary particle diameter of 27.5 nm is assumed in the current sectional model, and a discontinuity in the gradient of the PSD at this location is also observed in the calculations. However, the effect is moderate, and the shape of the measured PSDs is not matched by the calculations in this region. The agreement of calculated PSDs obtained with the acetylene based nucleation model varies widely. The nucleation rate $k_{N,1}$ by Lindstedt [27] results in peak locations at larger particle sizes than measured. Results from calculations using $k_{N,2}$ by Sunderland et al. [76] show the same tendency, although less pronounced. This is consistent with the observations of Sunderland et al. [74, 76] and Lin et al. [75] who report the rate used by Leung et al. [23] ($\approx 1.6 \times k_{N,1}$) to be excessively high. The discrepancy was related to scarcity of experimental data and uncertainties in the interpretation of optical measurements used to evaluate primary particle sizes [74].

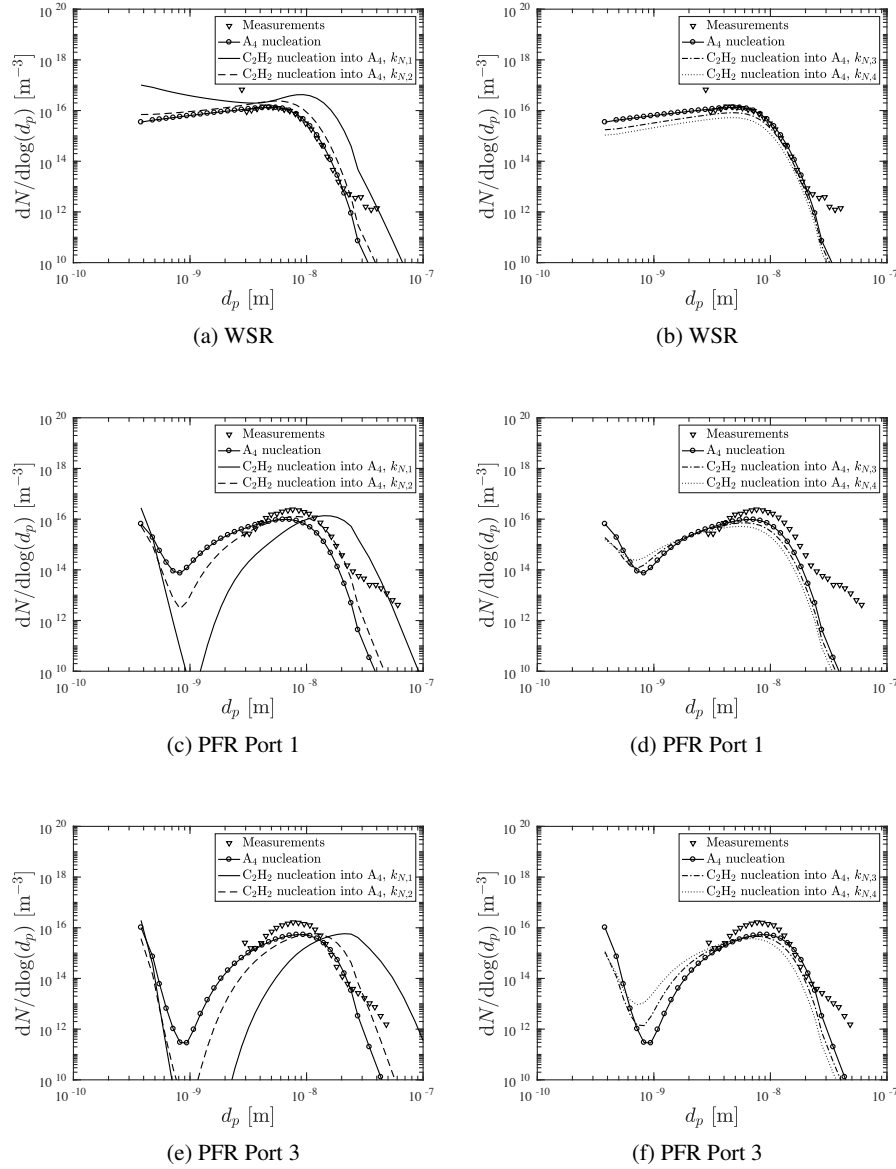


Figure 3.1: Calculated soot particle size distributions in the WSR and at PFR Ports 1 and 3 of the WSR/PFR setup of Lenhert and Manzello [18] with C_2H_4 air at $\Phi = 2.0$ and $T_{WSR} = 1723$ K. Comparison of measurements and computations using pyrene (A_4) and acetylene based nucleation models with reaction rate coefficients $k_{N,1}$ by Lindstedt [27], $k_{N,2}$ for diffusion flames by Sunderland and Faeth [76], $k_{N,3}$ and $k_{N,4}$ from Table 4.2. A constant value for the surface reactivity parameter of $\alpha_s = 0.85$ and the updated oxidation rates $k_O, k_{OH,2}$ and $k_{O_2,2}$ were used.

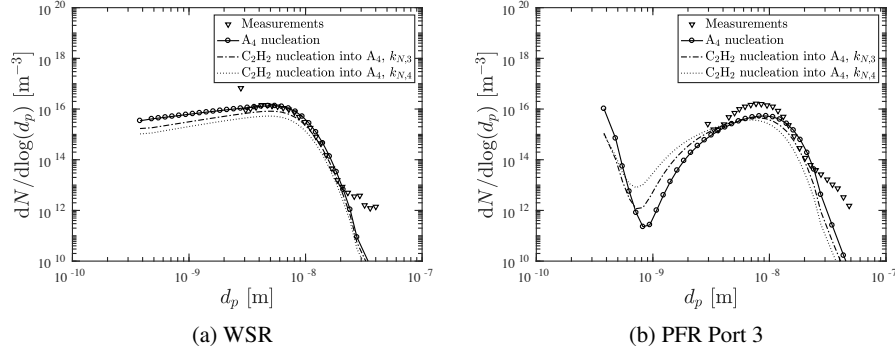


Figure 3.2: Calculated soot particle size distributions in the WSR and at PFR Port 3 of the WSR/PFR setup of Lenhart and Manzello [18] with C_2H_4 /air at $\Phi = 2.0$ and $T_{WSR} = 1723$ K. Comparison of measurements and computations using pyrene (A_4) and acetylene based nucleation models with reaction rate coefficients $k_{N,3}$ and $k_{N,4}$ from Table 4.2. A constant value for the surface reactivity parameter of $\alpha_s = 0.85$, and the oxidation rates k_O , $k_{OH,1}$ and $k_{O_2,1}$ were used.

Acceptable agreement for an acetylene based nucleation model can be obtained using $k_{N,3}$ and $k_{N,4}$, with the former matching the predictions from the pyrene based model closely. Figure 3.2 shows PSDs obtained using the latter two rates and the alternative oxidation rates (k_O , $k_{OH,1}$, $k_{O_2,1}$). The results are virtually identical to those of Fig. 3.1.

The sensitivity of the model to a range of assumptions is explored in Figs. 3.3–3.7, where the updated rates $k_{N,4}$ and k_O , $k_{OH,2}$, $k_{O_2,2}$ are used unless stated otherwise. For the calculations shown in Figs. 3.1–3.2, the value of $C_a = 3.0$ for the van der Waals enhancement factor was retained from work by Lindstedt and Waldheim [13] on laminar premixed stagnation flow flames. PSD predictions in the WSR and at PFR Port 3 from calculations covering the range $1.5 \leq C_a \leq 9.0$ are presented in Fig. 3.3. In the WSR, the influence on the PSD is moderate, whereas the predictions at PFR Port 3 are noticeably affected. With increasing values of C_a , particularly concentrations of small particles with $d_p < 1$ nm are depleted more rapidly. For values $C_a \leq 3.0$, the influence on the PSD is mostly limited to the zone $d_p < 10$ nm, with the distributions moderately affected at sizes smaller than the mode at ≈ 7 nm, and negligibly increased concentrations at larger particle sizes. The value $C_a = 9.0$ has been used in the context of method of moments calculations in turbulent flames [28], where soot particles are repre-

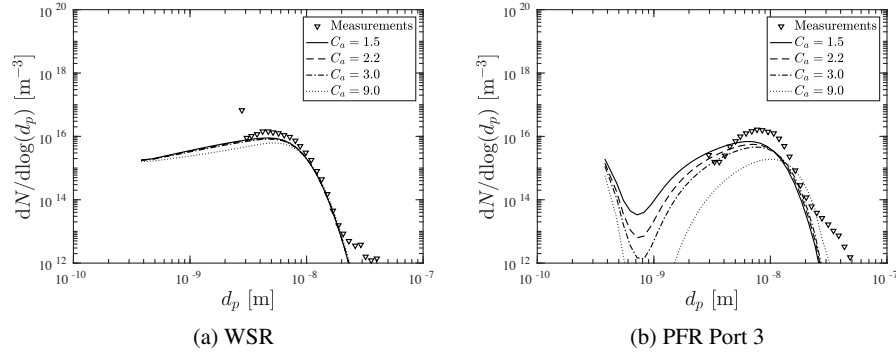


Figure 3.3: Calculated soot particle size distributions in the WSR and at PFR Port 3 of the WSR/PFR setup of Lenhert and Manzello [18] with C_2H_4/air at $\Phi = 2.0$ and $T_{WSR} = 1723$ K. The sensitivity to the van der Waals enhancement factor C_a is shown. Computations use C_2H_2 nucleation into pyrene (A_4) with the rate $k_{N,3}$, $\alpha_s = 0.85$, and the oxidation rates k_O , $k_{OH,2}$ and $k_{O_2,2}$.

sented by a single mean particle size, and a significant impact is observed here, with the number of small particles around 1 nm being depleted rapidly, a shift of the mode to ≈ 11 nm and moderately elevated concentrations for particles larger than ≈ 15 nm compared to the calculations with $C_a \leq 3.0$. The temperature distribution in the PFR is tentatively imposed based on experimental measurements at Ports 1 and 3 for slightly different operating conditions [14], and it is recognized that the uncertainty of temperature measurements in the WSR is $\pm 10\%$ [17]. In order to assess the effect of this uncertainty on PSD predictions, the temperature in the reactor system was arbitrarily raised or decreased by ± 50 and ± 100 K and the predictions thus obtained are presented in Fig. 3.4. A significant impact is observed, with an increase in temperature resulting in an acceleration of the shift of the mode to larger particle sizes with residence time, along with an increased depletion of particles smaller than the mode. Calculation results for a range of values for the surface reactivity parameter α_s are presented in Fig. 3.5. Under the current conditions at $\Phi = 2.0$, an increase of α_s from 0.25 to 1.00 leads to a shift of the peak of the distribution towards larger particles, approximately comparable to the effect of the temperature variations of ± 100 K discussed above. The use of naphthalene as a nucleating species and the addition of the additional oxidation term defined in Eq. (2.63) based on an analogy to the soot surface chemistry model [14, 30] compared to the reference case is shown in Figures 3.6 and 3.7. In the

former case, peak particle sizes are noticeably reduced in both the WSR and PFR, while for the latter, number densities for particles larger than 4 nm are considerably reduced and the qualitative agreement with the experiment worsened in the WSR and not given at PFR Port 3.

3.3. Conclusions

Soot nucleation rates and oxidation rates in the context of a sectional soot model using an acetylene based nucleation step have been evaluated in a well-stirred/plug flow reactor configuration. The following conclusions can be drawn:

- Compared to rates previously used in the context of two-equation and method of moments calculations [28, 30], the reduced nucleation rates $k_{N,3}$ and $k_{N,4}$ yield improved agreement of PSD predictions with experimental data and calculations using a pyrene-based nucleation model.
- The sensitivity to model parameters and other assumptions was explored, and a moderate impact was found for changes in the van der Waals enhancement factor C_a .
- On the other hand, the value adopted for the surface reactivity parameter α_s , as well as variations of the temperature in the range ± 100 K, within the experimental uncertainty, influence the predictions considerably.
- Best agreement between measurements and calculations using either the pyrene-based model or the acetylene-based model with $k_{N,3}$ and $k_{N,4}$ is found for an empirically optimised value of $\alpha_s = 0.85$.
- The use of naphthalene as the nucleating species within the acetylene based model and the adoption of an additional O_2 based oxidation term both worsen the agreement with the experimental data.

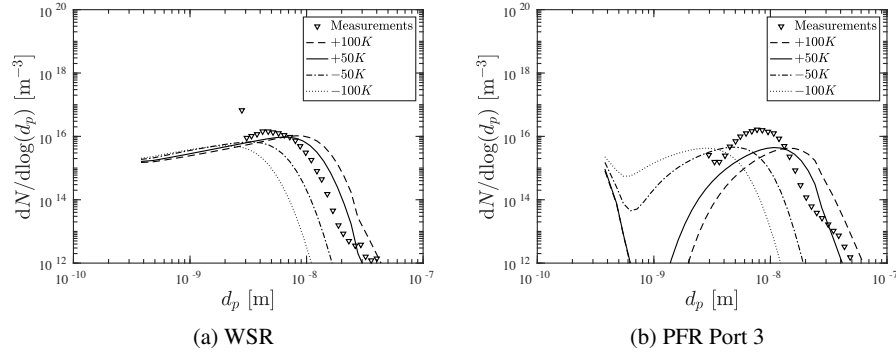


Figure 3.4: Calculated soot particle size distributions in the WSR and at PFR Port 3 of the WSR/PFR setup of Lenhert and Manzello [18] with C_2H_4/air at $\Phi = 2.0$ and $T_{WSR} = 1723$ K. The sensitivity to uncertainties in the temperature are shown. Computations use C_2H_2 nucleation into pyrene (A_4) with the rate $k_{N,3}$, $\alpha_s = 0.85$, and the oxidation rates k_O , $k_{OH,2}$ and $k_{O_2,2}$.

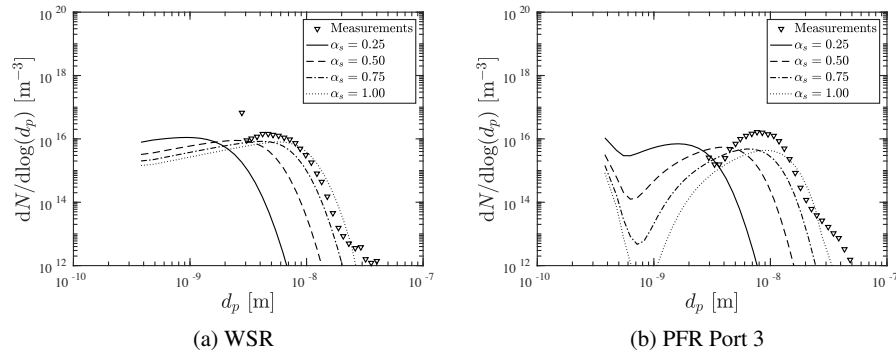


Figure 3.5: Calculated soot particle size distributions in the WSR and at PFR Port 3 of the WSR/PFR setup of Lenhert and Manzello [18] with C_2H_4/air at $\Phi = 2.0$ and $T_{WSR} = 1723$ K for different values of the surface reactivity parameter α_s . Computations use C_2H_2 nucleation into pyrene (A_4) with the rate $k_{N,3}$ and the oxidation rates k_O , $k_{OH,2}$ and $k_{O_2,2}$.

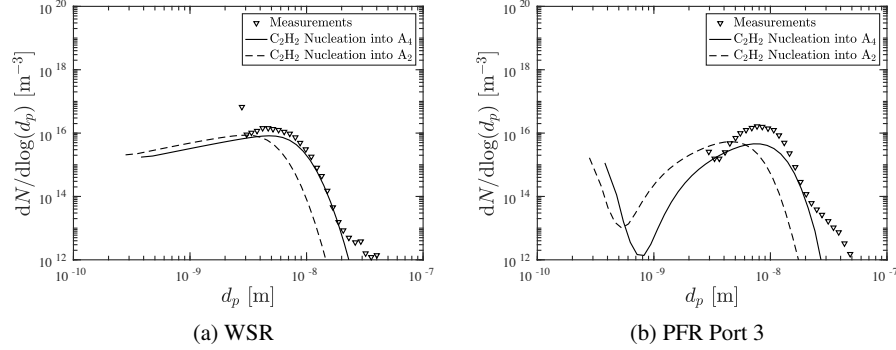


Figure 3.6: Calculated soot particle size distributions in the WSR and at PFR Port 3 of the WSR/PFR setup of Lenhert and Manzello [18] with C_2H_4/air at $\Phi = 2.0$ and $T_{WSR} = 1723$ K. Calculations with C_2H_2 based nucleation into pyrene (A_4) and naphthalene (A_2) are shown. The nucleation rate $k_{N,3}$, $\alpha_s = 0.85$, and the oxidation rates k_O , $k_{OH,2}$ and $k_{O_2,2}$ were used.

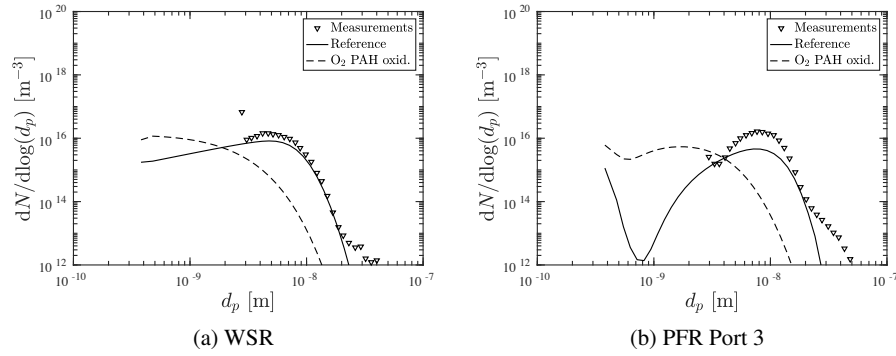


Figure 3.7: Calculated soot particle size distributions in the WSR and at PFR Port 3 of the WSR/PFR setup of Lenhert and Manzello [18] with C_2H_4/air at $\Phi = 2.0$ and $T_{WSR} = 1723$ K. The nucleation rate $k_{N,3}$, $\alpha_s = 0.85$, and the oxidation rates k_O , $k_{OH,2}$ and $k_{O_2,2}$ were used. The influence of additional oxidation via Eq. (2.63) with rate $k_{O_2,PAH}$ is shown.

4. Soot Modelling in a Turbulent Natural Gas Diffusion Flame With Local Extinction and Re-Ignition

4.1. Introduction

The Delft III / Adelaide flame ("Delft flame") [20] is a piloted turbulent non-premixed flame burning natural gas, and has been designated a target flame of the International Sooting Flame (ISF) workshop [111] series. Designed for manageable size, laboratory scale turbulent jet flames as the Delft flame allow experimentalists to obtain measurements with relative ease due to their straight-forward optical accessibility compared to real combustors or enclosed flames. They may serve as test-beds for the validation of soot models under turbulent flow conditions, reducing the uncertainty and cost associated with the solution of the flow field in a more complex configuration. Extensive measurements have been performed on the Delft flame, allowing comparison of fields of velocity, temperature and species mass fractions, as well as soot volume fraction: the experimental dataset available for this flame includes laser-Doppler anemometry (LDA) velocity measurements reported by Stroomer et al. [112], data on mean and variance of scalars, the PDF of mixture fraction and joint measurements of mixture fraction and scalars by Nooren et al. [21, 22] using Raman-Rayleigh-LIF (RRL) and laser-induced incandescence (LII) soot measurements by Qamar et al. [113]. Further, while the number of experimental datasets for turbulent sooting flames is already limited, the vast majority of flames considered are ethylene-fueled [32, 33, 111]. Using a methane-based fuel, the Delft flame is therefore particularly relevant for the validation of soot models under turbulent conditions, extending the envelope of fuels used. For these reasons, the Delft flame has been selected as object of study in this chapter.

Calculations of soot statistics in this flame have been carried out by Mueller and Pitsch [114] and Donde et al. [115] using LES with a flamelet / progress variable

approach and a hybrid method of moments model [58] for particle dynamics. Good agreement was reported for velocity and scalar fields, while the location of the peak mean soot volume fraction was predicted 30–40 nozzle diameters upstream of the experimental location with maximum soot levels overpredicted by factors of 3–5.5 [114] and 6.5 [115]. The disagreement was attributed to uncertainties in the sub-filter dissipation rate model and the PAH chemistry, with the computed early soot onset attributed to the latter. Further computational studies investigating the non-sooting aspects of the Delft flame have been carried out [116–121]. Merci et al. [117, 118] used conserved scalar presumed PDF and joint scalar transported PDF approaches. For the latter, the applied pilot model was found to have a strong influence on the flow field close to the nozzle exit, while the effect on the global flame shape was small [117]. The performance of three different micromixing models was also assessed [118]. Global flame extinction was observed with the interaction by exchange with the mean (IEM) model and local extinction was found to be underpredicted with the Euclidean Minimum Spanning Tree (EMST) model. The Curl’s coalescence/dispersion model was used to investigate the sensitivity to (i) the thermal power introduced by the pilot and (ii) to the model constant C_ϕ affecting the mixing frequency. It was found that either increasing the pilot power by 50 % or the value of C_ϕ to 3.0 was required for flame attachment to the burner. Ayache and Mastorakos [121] modelled the flame using LES with a conditional moment closure (CMC) sub-grid model and successfully captured local extinction and re-ignition close to the burner.

The investigation presented in this chapter extends past efforts to model the Delft III / Adelaide flame using a joint scalar transported PDF modelling approach [30] with soot particle dynamics treated via two-equation (e.g. [23, 27]) and method of moments with interpolative closure (MOMIC) [24] based models. The approach, in principle, eliminates uncertainties associated with the influence of turbulence-chemistry interactions. The updated rates for soot nucleation and oxidation derived in Chapter 3 are applied in computations of the Delft flame. A sensitivity analysis is performed to elucidate the impact of nucleation rate uncertainties on the location of the peak soot concentration and possible causes analysed. Soot oxidation rates are also updated with recent recommendations and the impact assessed in both configurations.

4.2. Case Configuration

The Delft burner is shown in Fig. 4.1 and features a concentric layout of a central fuel jet at $Re = 9,700$ with a diameter $d = 6$ mm at the exit plane, an annular rim of 4.5 mm width holding the pilot flame, and an annular air co-flow at $Re = 8,600$ with inner and outer diameters of 30 and 45 mm in the fuel exit plane [112]. The burner is placed in an octagonal burner chamber in which a forced secondary air co-flow prevents recirculation. The pilot burns a mixture of acetylene, hydrogen and air, with the same elemental carbon-to-hydrogen ratio as the main fuel jet at an equivalence ratio of $\Phi = 1.4$, and is supplied by twelve individual pilot holes of diameter 0.5 mm embedded into the rim around the fuel jet on a circle of radius 7.5 mm. It accounts for about 1 % of the total power of the flame. The mean exit

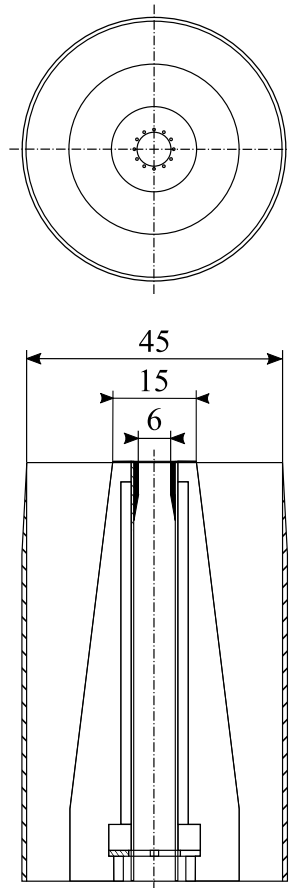


Figure 4.1: Top and side view of the Delft burner head. Dimensions in mm.

Table 4.1: Composition of Delft flame main fuel jet in percent mole fraction in experiments and model: Dutch natural gas, California natural gas diluted with N₂, Adelaide natural gas diluted with N₂, and modified compositions of the latter two (Model 1 and 2).

Component	Dutch [112, 122]	California [22]	Model 1	Adelaide [113]	Model 2
CH ₄	81.29	81.70	81.70	79.89	79.89
C ₂ H ₆	2.87	3.00	3.10	3.72	3.92
C _n H _m	0.62	0.10	0.00	0.20	0.00
N ₂	14.32	14.60	14.60	13.97	13.97
O ₂	0.01	0.00	0.00	0.00	0.00
CO ₂	0.89	0.60	0.60	2.22	2.22

velocity of the cold pilot flow is reported by de Vries [122] to be $\tilde{U}_p = 12 \text{ m s}^{-1}$. The rim separating fuel jet and primary air co-flow, and holding the pilot flames, creates a recirculation zone near the nozzle, providing an additional flame stabilisation mechanism. The conditions lead to a flame with strong turbulence-chemistry interactions at the burner exit with some local extinction and re-ignition further downstream. The composition of the main fuel varies slightly between experiments as shown in Table 4.1. Although the difference is expected to have only a minor impact, calculations are carried out using two compositions: Dutch natural gas, used for the LDA velocity measurements by Stroomer et al. [112], and diluted California natural gas used for for the RRL scalar and temperature field measurements by Nooren et al. [21, 22] are modelled via the composition termed "Model 1". The composition of diluted Adelaide natural gas, as used for the LII soot measurements by Qamar et al. [113], is approximated via the composition denoted "Model 2". As the current reduced chemical reaction mechanism (see Section 2.9) only includes hydrocarbons up to ethane, mole fractions of higher hydrocarbons (C_nH_m) present in the experimental fuel compositions are hence added to that of ethane in the model compositions. These higher hydrocarbons contribute no more than 0.62 % to the total fuel volume, and their exclusion is therefore considered to have a negligible effect.

Merci et al. [117] assessed the use of rigorously constructed inlet conditions based on separate flow calculations inside the burner head in comparison to the simpler conditions derived from experimental mass flow rates and LDA measurements near the inlet used by Nooren et al. [116]. The influence of the inlet conditions was shown to be limited to the zone close to the nozzle exit, and no significant advantage of the former set was found. In the present case, a set of simpler condi-

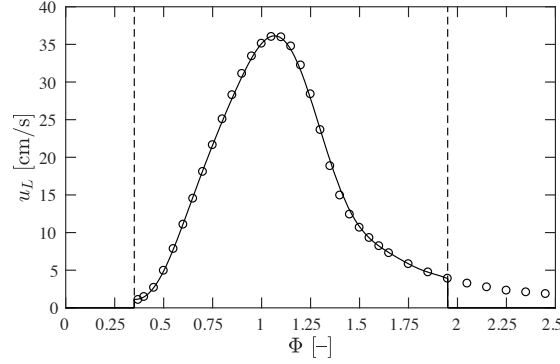


Figure 4.2: Laminar burning velocity of natural gas obtained from laminar pre-mixed flame calculations with strain rate $a \approx 100 \text{ s}^{-1}$ (\circ) with a sum-of-sines fit for $0.35 \leq \Phi \leq 1.95$ (—). The "Model 2" composition defined in Table 4.1 was used.

tions based on those reported by Merci et al. [117] was therefore used: flat profiles for velocity, turbulence kinetic energy and turbulence dissipation rate in the fuel jet ($\tilde{U}_f = 21.9 \text{ m s}^{-1}$, $\tilde{k}_f = 2.2 \text{ m}^2 \text{ s}^{-2}$, $\tilde{\varepsilon}_f = 500 \text{ m}^2 \text{ s}^{-3}$), and secondary air co-flow ($\tilde{U}_{a2} = 0.4 \text{ m s}^{-1}$, $\tilde{k}_{a2} = 4 \times 10^{-4} \text{ m}^2 \text{ s}^{-2}$, $\tilde{\varepsilon}_{a2} = 2 \times 10^{-4} \text{ m}^2 \text{ s}^{-3}$), and the profiles in the primary air co-flow were based on a fully developed annulus flow calculation with bulk velocity $\tilde{U}_{a1} = 4.3 \text{ m s}^{-1}$. Across the pilot rim, the axial velocity profile in the inlet plane drops linearly from 21.9 m s^{-1} at the edge of the fuel jet to 1 m s^{-1} at a radial position $y = 3.7 \text{ mm}$ and remains at this value for $y \leq 7.5 \text{ mm}$. The inlet axial velocity profile in the primary air co-flow is flattened by a factor of 0.96 to account for the additional momentum introduced into the computation by the imposed velocity profile across the pilot rim. The turbulence kinetic energy k across the rim is taken to vary linearly from the value in the fuel jet to zero at the outer edge of the rim. The turbulence dissipation rate is approximated from a dimensional argument as $\varepsilon_{max} = \sqrt{2/3} k^{3/2} l_t^{-1}$, with the turbulence length scale l_t set to the rim width (9 mm).

The pilot of the Delft flame is modelled by introducing a volumetric enthalpy source in a region close to the burner exit, while omitting the pilot flow, similarly to the model chosen by Merci et al. [117] for the same flame. The pilot flame being responsible for only about 1 % of the burner's total power output, omitting its mass flow is not expected to alter downstream results considerably. The volume occupied by the heat source is defined by an annulus located at the inner boundary

Table 4.2: Reaction rate constants for soot nucleation via Eq. (2.29) presented in the form $k_{N,i} = A_i \exp(-E_i/RT)$. Units are in K, kmol, m³ and s.

k_i	A_i	α_i	β_i	E_i/R	Source
$k_{N,1}$	6.30×10^3	1	0	21,000	Lindstedt [27]
$k_{N,2}$	3.79×10^1	1	0	17,500	Sunderland and Faeth [76]
$k_{N,3}$	6.30×10^1	1	0	21,000	Current work
$k_{N,4}$	3.78×10^1	1	0	21,000	Current work

of the pilot rim in the exit plane of the burner and with an axial extension x as $3.0 \leq y \leq 4.5$ mm, $0 \leq x \leq 7.5$ mm. Ignition was achieved using a power input 25 % higher than the experimental value of 196 W.

Table 4.3: Reaction rate constants for soot growth and oxidation in Eqs. (2.35) and (2.59)–(2.61) presented in the form $A_i \alpha_i T^{\beta_i} \exp(-E_i/RT)$ [27, 28, 96]. Units are in K, kmol, m³ and s.

k_i	A_i	α_i	β_i	E_i/R
$k_{G,1}$	7.50×10^2	1	0	12,100
$k_{G,2}$	3.57×10^{21}	1	-3.176	7,471
k_O	9.09	0.2	1/2	0
$k_{OH,1}$	8.82	0.05	1/2	0
$k_{O_2,1}$	6.43	0.723	1/2	11,250
$k_{OH,2}$	8.82	0.10	1/2	0
$k_{O_2,2}$	6.43	116	1/2	19,680

Both the use of the conventional dissipation rate closure for the scalar mixing model defined in Eq. (1.3) and of the extended closure by Kuan et al. [41] shown in Eq. (1.4) were explored for this flame. For the latter closure, the required laminar burning velocity u_l of the fuel was obtained from laminar premixed flame calculations using a strain rate of $a \approx 100$ s⁻¹ for a range of equivalence ratios. A sum-of-sines fit in the range $0.35 \leq \Phi \leq 1.95$ to the discrete burning velocity data was created as shown in Fig. 4.2, and implemented into the turbulent flame calculations.

The gas phase chemistry was modelled via the reduced chemical reaction model outlined in Section 2.9, with 144 reactions, 15 solved and 14 steady-state species. The reaction rate coefficients for soot nucleation, growth and oxidation used in the context of the two-equation and method of moments model for this flame are shown in Table 4.2 and Table 4.3, where $k_{G,1}$ denotes the rate for soot growth via Eq. (2.36), and $k_{G,2} = k_X^f$ is the acetylene addition rate for the PAH analogy model to soot surface growth in Eq. (2.57). The full set of rates for the latter model

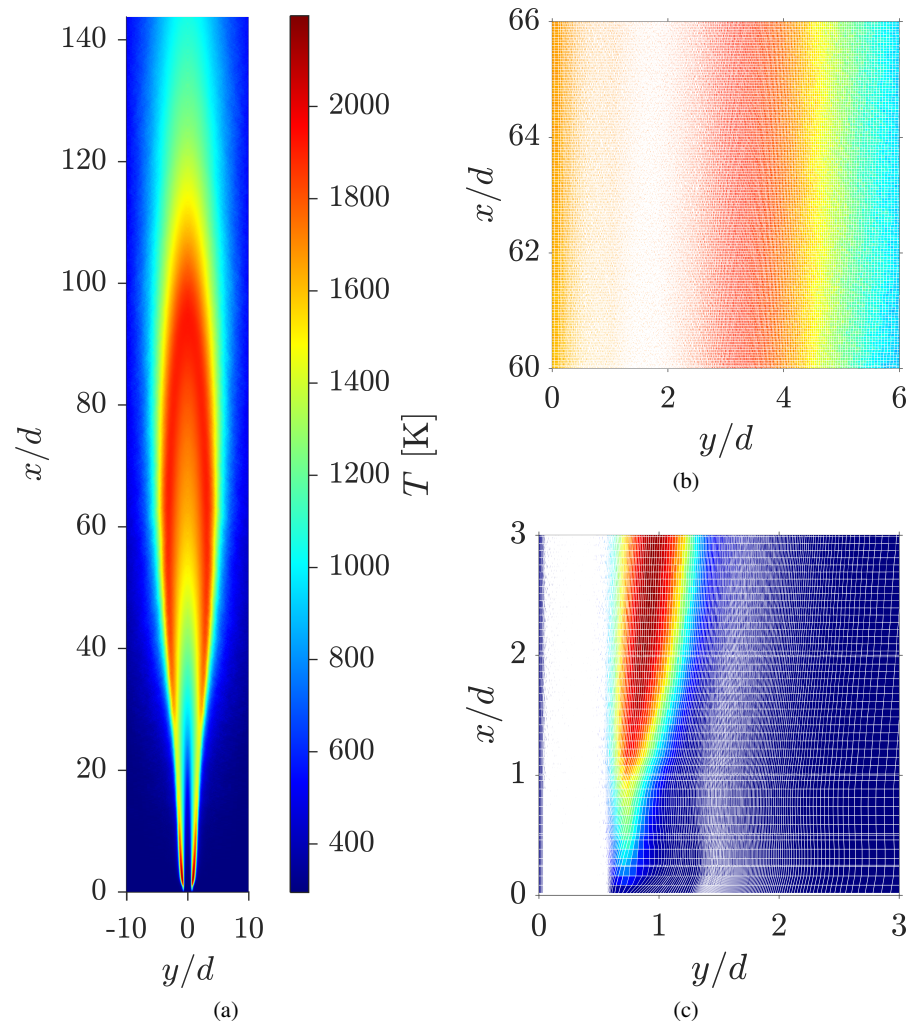


Figure 4.3: (a) Calculated temperature map in the Delft flame. (b) Grid detail at $60 \leq x/d \leq 66$. (c) Grid detail near the nozzle. Control volume boundaries are shown with white lines.

is outlined in Table 2.1 in Section 2.4. They include the nucleation rates $k_{N,1}$, $k_{N,3}$, $k_{N,4}$ as well as the set of soot oxidation rates k_O , $k_{OH,1}$, $k_{O_2,1}$ retained from previous work [28, 30] and the updated set k_O , $k_{OH,2}$, $k_{O_2,2}$, all evaluated in the context of the sectional model in Chapter 3.

The computations featured 465 distributed radial control volumes with initially 275 volumes in the core jet, 70 in the pilot and 120 in the coflow. In Fig. 4.3, the calculated temperature distribution is presented and local details of the grid are shown. In the current approach, the axial (x) grid resolution is computed during run-time via a Courant–Friedrichs–Lewy (CFL) condition. The radial (y) dimension is converted to normalised stream function (ω) space via the inlet conditions, and calculations rely on grids in both y and ω -space [29]. While the location of control volume boundaries is fixed in ω -space, the volumes are dynamically redistributed in y -space during computation, according to the evolution of the stream function in physical space. In the current work, the grid is set-up in ω -space with a high density of nodes in the core jet, and is expanding smoothly towards the outer domain boundary. As a result, the jet is initially over-resolved (Fig. 4.3c). As the height above the burner increases, the grid relaxes towards a more even distribution in y -space (Fig. 4.3b). The approach ensures sufficient resolution in the main reaction zone as the jet expands. It was found that a smoother radial distribution of control volumes could be achieved across the domain by defining the radial grid in ω -space compared to the alternative definition in y -space (and deduction of the ω -grid). The computations featured a minimum of 200 Lagrangian stochastic particles per control volume and the computations were performed using 20 cores.

4.3. Results and Discussion

4.3.1. Velocity and Scalar Fields

In calculations of the Delft III / Adelaide flame, the standard scalar dissipation rate closure defined by Eq. (1.3) was found to lead to early flame extinction at $x/d \leq 25$ for the range $2.3 \leq C_\phi \leq 4.0$. For $C_\phi = 6.0$, no global flame extinction was observed. The latter value is unrealistically high and the observed behaviour is consistent with the excessive flame extinction found by Lindstedt et al. [43] for partially premixed flames and with the need to further increase the pilot power [118]. By contrast, the extended closure defined in Eq. (1.4) was found to prevent flame extinction and all computations presented were obtained with this formula-

tion. Figures 4.4–4.6 show radial profiles of Favre mean axial velocity (\tilde{U}), RMS of axial (u'') and radial (v'') velocities, mixture fraction (f) and temperature (T) in the Delft flame. The agreement between computations and experiments is overall arguably fair, although there is a tendency to over-predict v'' throughout and u'' far downstream from the burner exit. The correspondence between the computed and measured mixture fraction statistics is generally good, although f'' is over-predicted in the jet centre near the nozzle and the variance peaks in the jet flanks at $x/d = 41\frac{2}{3}$ are somewhat too low. A tendency to moderately overpredict the rate of spread of the jet close to the nozzle at $x/d \leq 8\frac{1}{3}$ and in the downstream region $x/d \geq 33\frac{1}{3}$ is observed, apparent from lower values of \tilde{f} compared to the experimental data at the centre-line, and increased \tilde{f} in the jet flanks. Agreement of \tilde{f} in the zone $16\frac{2}{3} \leq x/d \leq 25$ is arguably excellent. Further, the temperatures at the outer edges of the core jet are predicted to be higher as shown, for example, at $x/d \leq 8\frac{1}{3}$ and $x/d = 41\frac{2}{3}$. The peak temperature is also overpredicted, while the location is in reasonable agreement. The discrepancies can in part be attributed to the boundary conditions across the pilot rim, in conjunction with the parabolic CFD solver, not correctly reflecting the downstream effect of the small recirculation zone. By comparison, the velocity and scalar fields reported by LES simulations [114, 115] show improved agreement for velocity and temperature statistics.

While the disagreement of the calculated mixture fraction results with experiment is moderate, the locally increased values of \tilde{f} in the jet flanks correspond to a widening of the reaction zone with its center placed radially outward from the experimental location. To address this effect, radial profiles of temperature and species' mass fractions are shown in Figs. 4.6–4.14 in both normalized physical space and mixture fraction space, where mapping to the latter was obtained from the calculated and measured values of the Favre mean mixture fraction \tilde{f} for the computed and measured data, respectively.

The prediction of the H_2O , CO_2 and O_2 mass fractions mirrors the temperature data to some extent as shown in Figs. 4.7–4.9 with reduced accuracy in the jet flanks at $x/d = 33\frac{1}{3}$ and $x/d = 41\frac{2}{3}$, while elevated values of O_2 near the jet centre for $x/d = 4\frac{1}{6}$ indicate excessive extinction in this zone. Computed mass fractions of H_2 suggest too high peak values close to the burner exit with improved agreement further downstream (Fig. 4.10). The agreement is further improved in mixture fraction space. The inaccuracies in the jet flanks, noted for temperature and $\text{H}_2\text{O}/\text{CO}_2/\text{O}_2$, are not present for hydrogen. This suggests that the reaction zone structure is comparatively well reproduced. The computed CH_4 mass fractions

shown in Fig. 4.11 appear to support this suggestion. The observation is important as soot formation is expected to occur in fuel rich mixtures towards the fuel jet and not in the leaner mixtures in the jet flanks. Computed CO mass fractions presented in Fig. 4.12 show a tendency to overpredict the mean at the peaks for $x/d \leq 16\frac{2}{3}$ and also in the centre of the jet further downstream as shown in Fig. 4.12. The computed mass fraction statistics for OH are presented in Figures 4.13 and 4.14. The RMS fluctuations (Fig. 4.13b) are of the same order as the mean (Fig. 4.13a) and the data is hence presented separately for clarity. The peak location is well reproduced along with the extent of the reaction zone with peak values showing a tendency to being over predicted as expected from the computed temperatures.

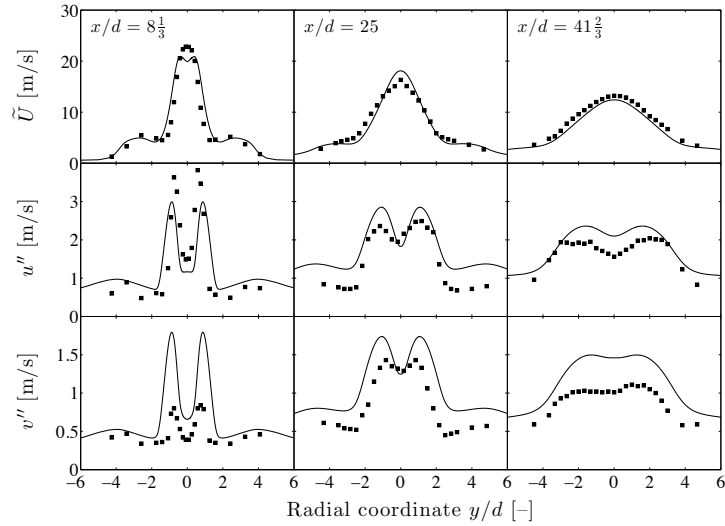


Figure 4.4: Radial profiles of Favre mean axial velocity \tilde{U} and RMS of axial (u'') and radial (v'') velocity in the Delft III / Adelaide flame at axial positions $8\frac{1}{3} \leq x/d \leq 41\frac{2}{3}$. Comparison of calculations (lines) to experimental data (symbols) by Stroomer [112]. The "Model 1" fuel composition was used for calculations (see Table 4.1).

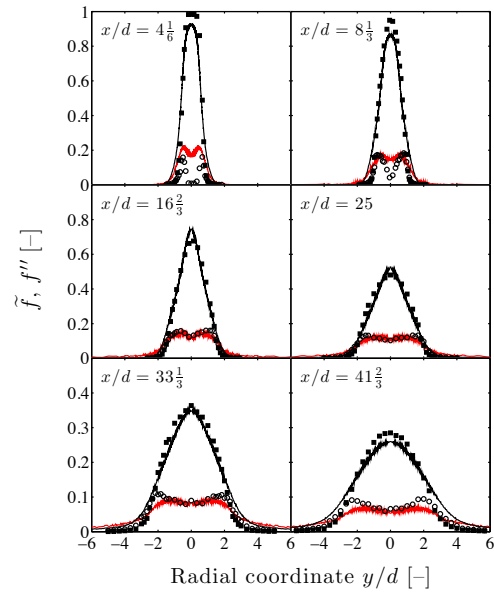
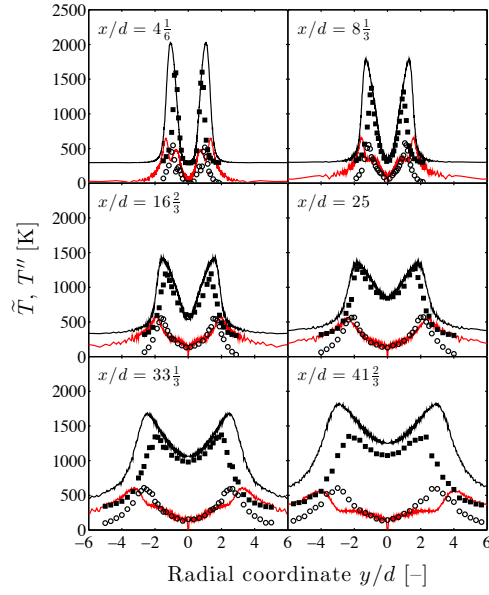
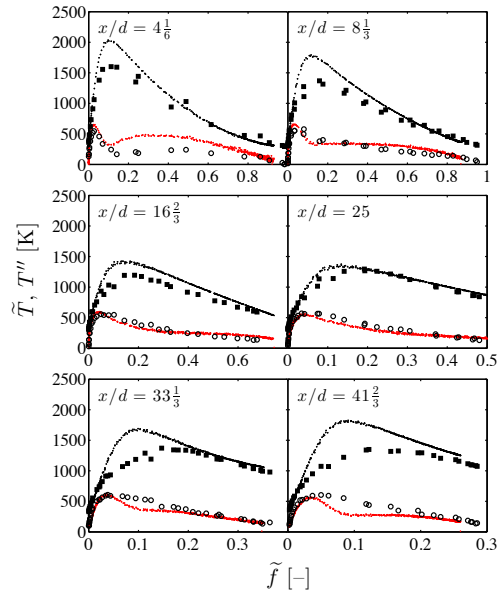


Figure 4.5: Calculated radial profiles of Favre mean mixture fraction (\tilde{f} , black lines) and its RMS (f'' , red lines) in the Delft III / Adelaide flame at axial positions $8\frac{1}{3} \leq x/d \leq 41\frac{2}{3}$. Comparison to mean (black squares) and RMS (circles) from experimental data by Nooren et al. [21, 22]. The "Model 2" fuel composition was used for calculations (see Table 4.1).

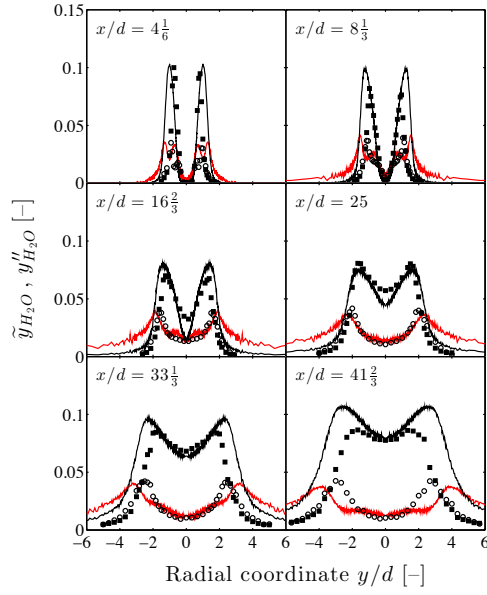


(a)

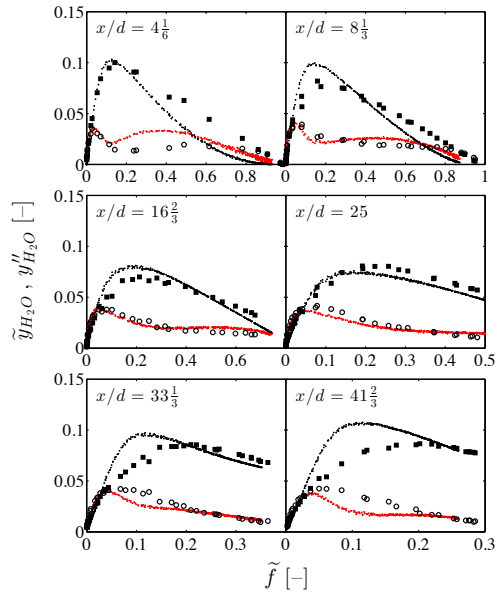


(b)

Figure 4.6: Calculated radial profiles of Favre mean temperature (\tilde{T} , black lines/dots) and its RMS (T'' , red lines/dots) in the Delft III / Adelaide flame at axial positions $8\frac{1}{3} \leq x/d \leq 41\frac{2}{3}$ (a) in physical space and (b) in mixture fraction space. Comparison to mean (black squares) and RMS (circles) from experimental data by Nooren et al. [21, 22]. The mapping to mixture fraction space was obtained via the calculated and measured Favre mean mixture fractions. The "Model 2" fuel composition was used (see Table 4.1).

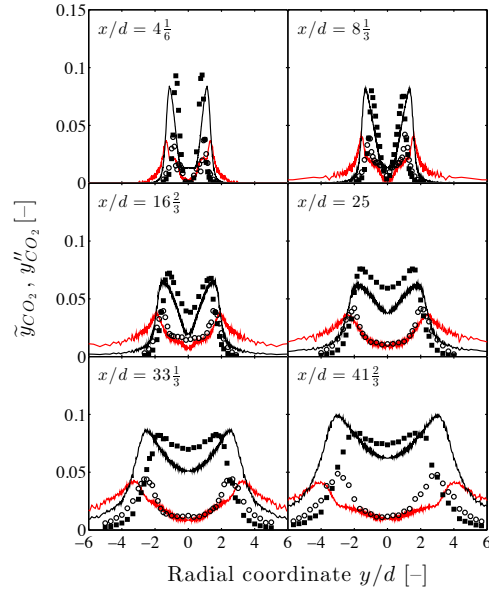


(a)

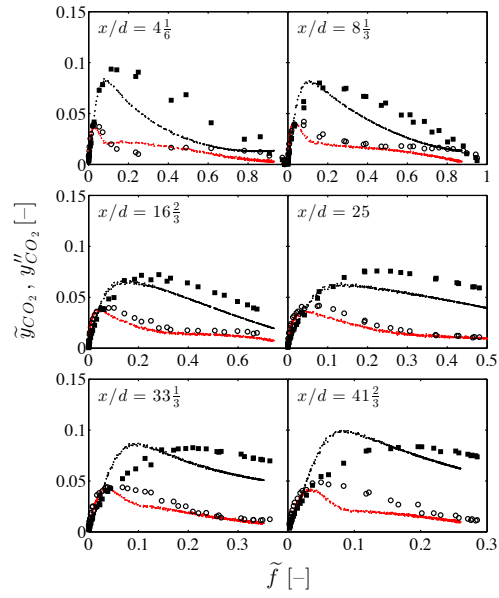


(b)

Figure 4.7: Calculated radial profiles of Favre mean H_2O mass fraction $\overline{\gamma}_{\text{H}_2\text{O}}$, black lines/dots) and its RMS ($\gamma''_{\text{H}_2\text{O}}$, red lines/dots) in the Delft III / Adelaide flame at axial positions $8\frac{1}{3} \leq x/d \leq 41\frac{2}{3}$ (a) in physical space and (b) in mixture fraction space. Comparison to mean (black squares) and RMS (circles) from experimental data by Nooren et al. [21, 22]. The "Model 2" fuel composition was used (see Table 4.1). The mapping to mixture fraction space was obtained via the calculated and measured Favre mean mixture fractions.

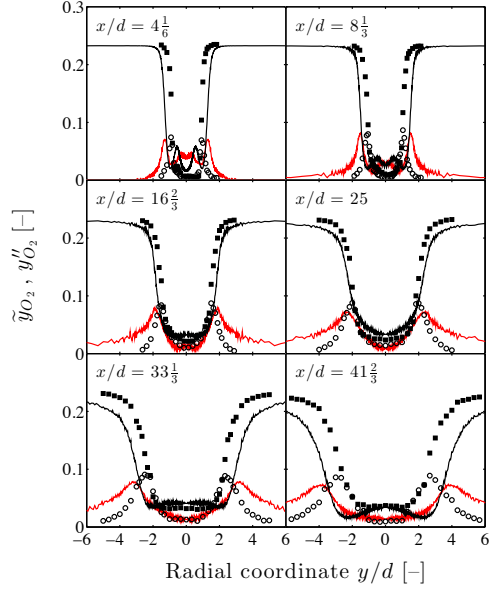


(a)

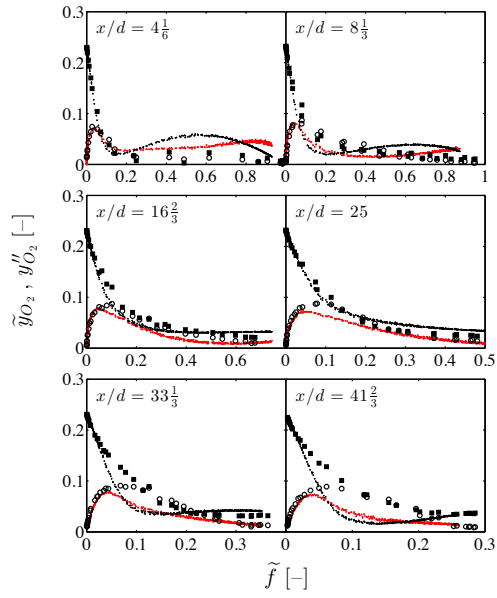


(b)

Figure 4.8: Calculated radial profiles of Favre mean CO_2 mass fraction $\overline{y}_{\text{CO}_2}$, black lines/dots) and its RMS (y''_{CO_2} , red lines/dots) in the Delft III / Adelaide flame at axial positions $8\frac{1}{3} \leq x/d \leq 41\frac{2}{3}$ (a) in physical space and (b) in mixture fraction space. Comparison to mean (black squares) and RMS (circles) from experimental data by Nooren et al. [21, 22]. The "Model 2" fuel composition was used (see Table 4.1). The mapping to mixture fraction space was obtained via the calculated and measured Favre mean mixture fractions.

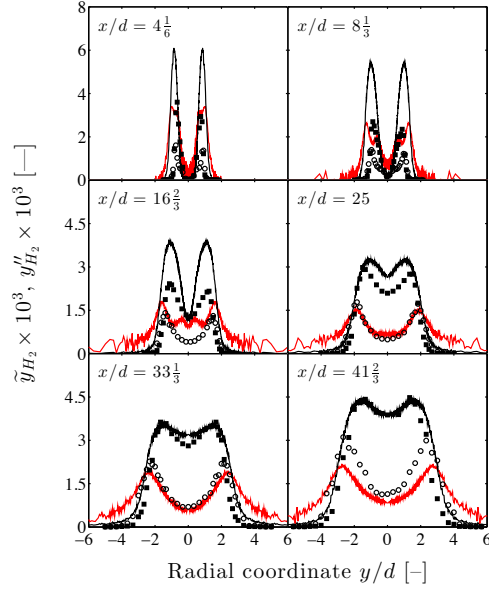


(a)

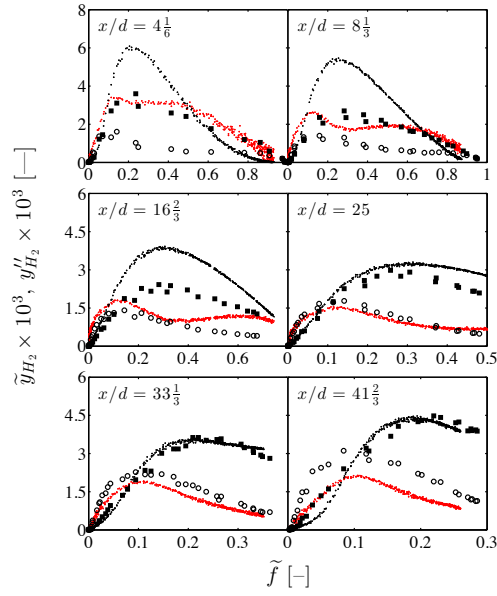


(b)

Figure 4.9: Calculated radial profiles of Favre mean O_2 mass fraction (\tilde{y}_{O_2} , black lines/dots) and its RMS (y''_{O_2} , red lines/dots) in the Delft III / Adelaide flame at axial positions $8\frac{1}{3} \leq x/d \leq 41\frac{2}{3}$ (a) in physical space and (b) in mixture fraction space. Comparison to mean (black squares) and RMS (circles) from experimental data by Nooren et al. [21, 22]. The "Model 2" fuel composition was used (see Table 4.1). The mapping to mixture fraction space was obtained via the calculated and measured Favre mean mixture fractions.

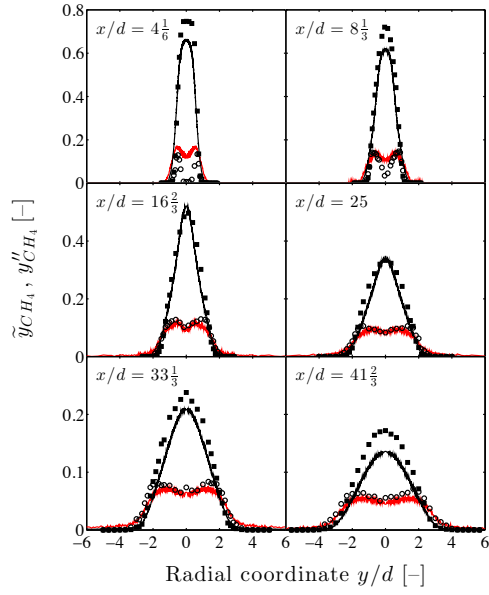


(a)

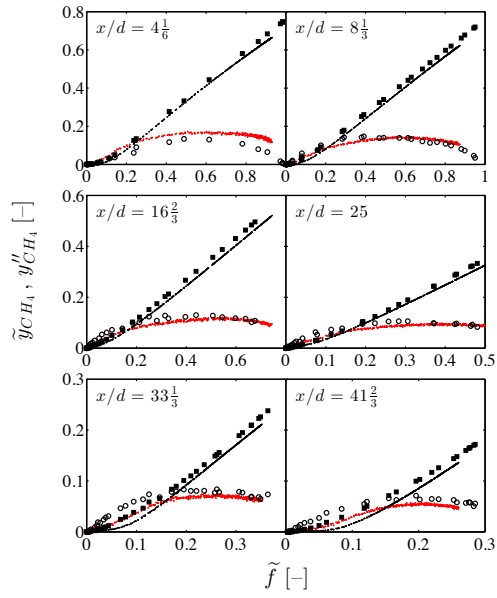


(b)

Figure 4.10: Calculated radial profiles of Favre mean H_2 mass fraction \overline{y}_{H_2} , black lines/dots) and its RMS (y''_{H_2} , red lines/dots) in the Delft III / Adelaide flame at axial positions $8\frac{1}{3} \leq x/d \leq 41\frac{2}{3}$ (a) in physical space and (b) in mixture fraction space. Comparison to mean (black squares) and RMS (circles) from experimental data by Nooren et al. [21, 22]. The "Model 2" fuel composition was used (see Table 4.1). The mapping to mixture fraction space was obtained via the calculated and measured Favre mean mixture fractions.

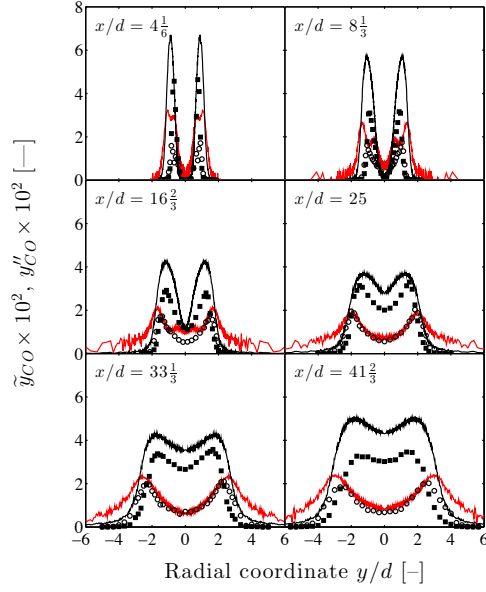


(a)

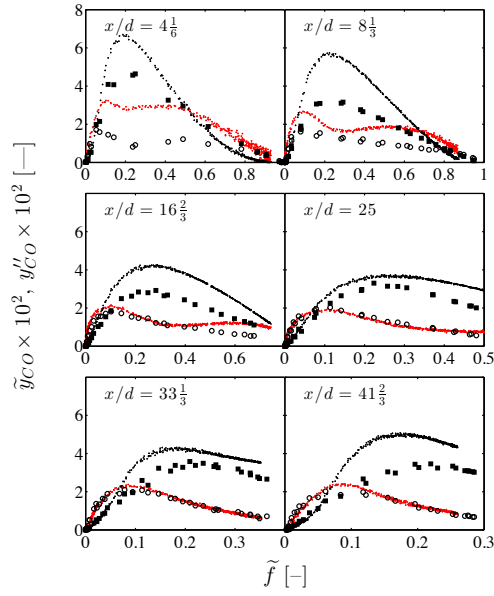


(b)

Figure 4.11: Calculated radial profiles of Favre mean CH_4 mass fraction \bar{y}_{CH_4} , black lines/dots) and its RMS (y''_{CH_4} , red lines/dots) in the Delft III / Adelaide flame at axial positions $8\frac{1}{3} \leq x/d \leq 41\frac{2}{3}$ (a) in physical space and (b) in mixture fraction space. Comparison to mean (black squares) and RMS (circles) from experimental data by Nooren et al. [21, 22]. The "Model 2" fuel composition was used (see Table 4.1).

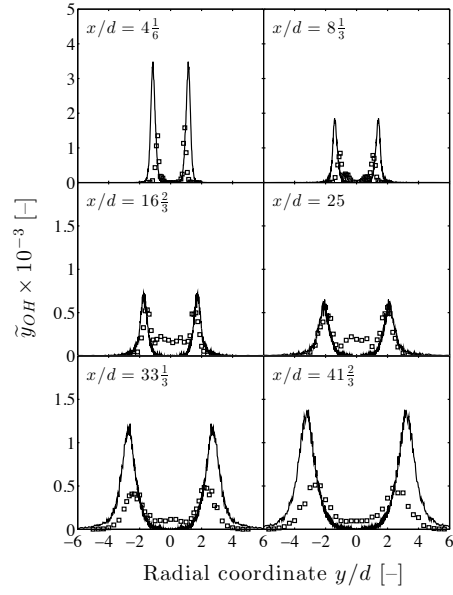


(a)

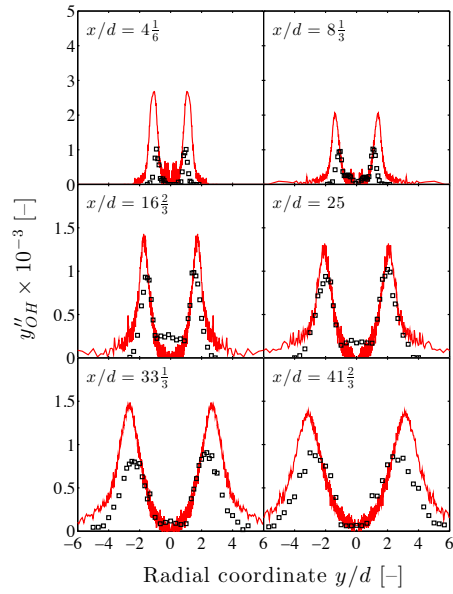


(b)

Figure 4.12: Calculated radial profiles of Favre mean CO mass fraction (\bar{y}_{CO} , black lines/dots) and its RMS (y''_{CO} , red lines/dots) in the Delft III / Adelaide flame at axial positions $8\frac{1}{3} \leq x/d \leq 41\frac{2}{3}$ (a) in physical space and (b) in mixture fraction space. Comparison to mean (black squares) and RMS (circles) from experimental data by Nooren et al. [21, 22]. The "Model 2" fuel composition was used (see Table 4.1). The mapping to mixture fraction space was obtained via the calculated and measured Favre mean mixture fractions.



(a)



(b)

Figure 4.13: Radial profiles of OH mass fraction in the Delft III / Adelaide flame at axial positions $8\frac{1}{3} \leq x/d \leq 41\frac{2}{3}$. Calculated (a) Favre mean \tilde{y}_{OH} (black lines), and (b) RMS y''_{OH} (red lines). Comparison to experimental data (squares) by Nooren et al. [21, 22]. The "Model 2" fuel composition was used (see Table 4.1).

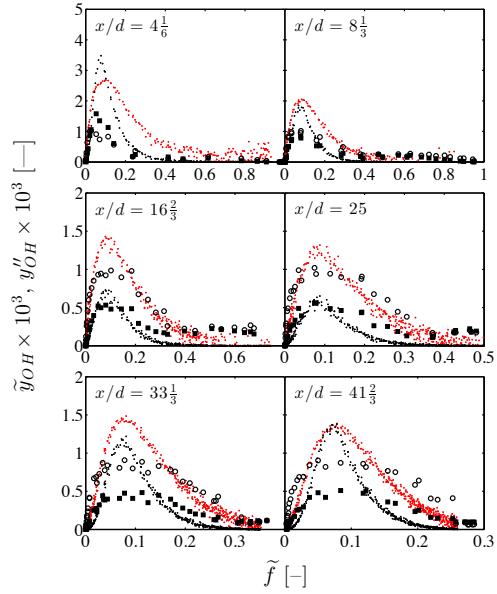


Figure 4.14: Radial profiles of Favre mean OH mass fraction (\tilde{y}_{OH} , black dots) and its RMS (\tilde{y}_{OH}'' , red dots) in the Delft III / Adelaide flame at axial positions $8\frac{1}{3} \leq x/d \leq 41\frac{2}{3}$ in mixture fraction space. Comparison to mean (black squares) and RMS (circles) from experimental data by Nooren et al. [21, 22]. The "Model 2" fuel composition was used (see Table 4.1). The mapping to mixture fraction space was obtained via the calculated and measured Favre mean mixture fractions.

4.3.2. Soot Statistics

Figures 4.15–4.17 show Favre mean soot mass fraction (\tilde{f}_v) at the centre-line compared to the experimental data by Qamar et al. [113] using the different sets of nucleation and oxidation rates discussed above. Predictions obtained with the two-equation model are shown in Fig. 4.15. The soot peak is predicted approximately 40 nozzle diameters upstream from the experimental location. This feature is consistent with the LES (combined with a flamelet / progress variable approach and a hybrid method of moments model) calculations by Mueller and Pitsch [114] and Donde et al. [115] who attribute it to uncertainties in the PAH chemistry. However, the nucleation rate in the current model was chosen to be consistent with that of pyrene in the WSR/PSR geometry, as discussed above, and found to reasonably predict the soot PSD. Furthermore, while the peak soot mass fraction increased by a factor of approximately 30 with the use of $k_{N,1} = 167 \cdot k_{N,4}$ (not shown), the axial location of the soot peak only moves in the range $x/d \approx 77.2$ to $x/d \approx 80.1$ (for the two-equation model and $k_O, k_{OH,2}, k_{O_2,2}$) and is hence broadly independent of the nucleation rate. For $k_{N,3}$, the calculated soot mass fraction is virtually identical for either set of soot oxidation rates ($k_O, k_{OH,1}, k_{O_2,1}$ or $k_O, k_{OH,2}, k_{O_2,2}$), while the maximum soot is moderately reduced for the updated set of oxidation rates. A corresponding data set for the soot volume fraction obtained with the method of moments by solving for the first four moments ($M_0 - M_3$) of the soot PSDF is presented in Fig. 4.16. Qualitative and quantitative agreement with experiment is very similar to that obtained with the two-equation model, with a reduction in peak values observed, and no marked influence of the set of oxidation rates used.

Figure 4.17 shows computations using the two-equation model with the additional PAH analogy model for soot surface growth (Eq. (2.57)). While the location of the maximum soot volume fraction is consistent with Figs. 4.15–4.16, increased soot levels are observed for $x/d \leq 50$. Lindstedt and Louloudi [28, 30] obtained ignition for the turbulent diffusion flames of Kent and Honnery [32] and Coppalle and Joyeux [33] using a presumed PDF / flamelet approach in the region close to the nozzle and increased soot levels far upstream were not observed. This points to a high sensitivity of the model to the locally elevated temperature and radical concentrations caused by the current pilot model, via Eqs. (2.40)–(2.54) (see Section 2.4), while one-step growth via Eq. (2.36) is unaffected. The overprediction is reduced by around 75 % when the pilot is modelled using the experimental value of the pilot power (not shown here), although an increased value of 1.25 times the

experimental power is preferred in the current work to improve the flame stability and prevent random flame extinction in the stochastic calculations. As for the two-equation and method of moments calculations with one-step growth, no strong sensitivity to the oxidation rates is observed in conjunction with the extended soot surface growth model, and soot levels are moderately reduced for $k_{\text{OH},2}$ and $k_{\text{O}_2,2}$. In comparison to the former cases, a reduced sensitivity to the nucleation rate is observed, and the measured peak soot volume fraction at the centre-line is approximately matched for $k_{N,4}$ and a constant value for the surface reactivity parameter of $\alpha_s = 0.50$ as shown. The LES simulations by Mueller and Pitsch [114] and Donde et al. [115] provide overall superior flow field predictions. However, the peak soot levels were found to be strongly influenced by the subfilter dissipation rate model with overpredictions by factors of 3–5.5 [114] and 6.5 [115] reported. In this context, the current results are encouraging and the compatibility of the simplified nucleation rate across different fuels and devices perhaps surprising. It can also be noted that despite the very different computational methods applied, the centre-line peak soot location varies approximately in the range $72 \leq x/d \leq 80$, compared to the experimental location of ≈ 116 .

Figure 4.18 shows the downstream evolution of the computed and measured axial mean mixture fraction. The experimental data is well reproduced up to the point where the measurements end. The locations of the computed and measured soot peaks are also indicated. Figure 4.19 shows the measured and calculated values of the mean soot volume fraction against the calculated mixture fraction on the centre-line. The computations shown were obtained with the two-equation model with the growth step given by Eq. (2.35) and with the PAH analogy for the soot surface chemistry with $\alpha_s = 0.50$ via Eq. (2.57). The data is compared to the lean (f_{LFL}) and rich (f_{RFL}) flammability limits of methane, and the stoichiometric mixture fraction ($f_{st} \approx 0.073$) of the Adelaide natural gas. The peak mean soot is predicted on the rich side of stoichiometry at $f \approx 0.11$, with no soot present below f_{LFL} and some transported soot at $f > f_{RFL}$. On the other hand, the peak of the measured mean soot is located at $f \approx 0.05$, below the stoichiometric mixture fraction, with some soot present below the lean flammability limit. The absence of experimental mixture fraction data for this part of the flame introduces uncertainties in the mapping of the measurements to the computed mixture fraction space. However, caution appears to be required when attributing the misaligned peak soot locations to specific model aspects.

Figures 4.20–4.21 show radial profiles of the Favre mean soot volume fraction.

In order to be able to compare the calculated radial distribution of soot to the measurements, given the discrepancy in peak soot location, the experimental data is compared to predicted profiles at locations further upstream by using a normalisation of the radial coordinate accounting for the rate of spread of the jet. Hence, the radial positions (y) are normalised by the half-width of the jet (δ). The latter value is calculated from the profile of the predicted mean mixture fraction \tilde{f} at any given axial position (x) as $\delta = 2 \cdot y_{half}$, where $\tilde{f}(y_{half})|_x = 0.5 \cdot \tilde{f}_{max}|_x$. It therefore corresponds to the radial location where the mixture fraction takes a value of half the maximum $\tilde{f}_{max}|_x$. The normalisation of the measured profiles of soot volume fraction is effected via the calculated mixture fraction. While the comparison is clearly approximate, it illustrates that the radial distribution of soot generally agrees with experimental data with a tendency to lower values of \tilde{f}_v in the jet flanks. In addition, the calculated oxidation of soot appears to be somewhat over-predicted.

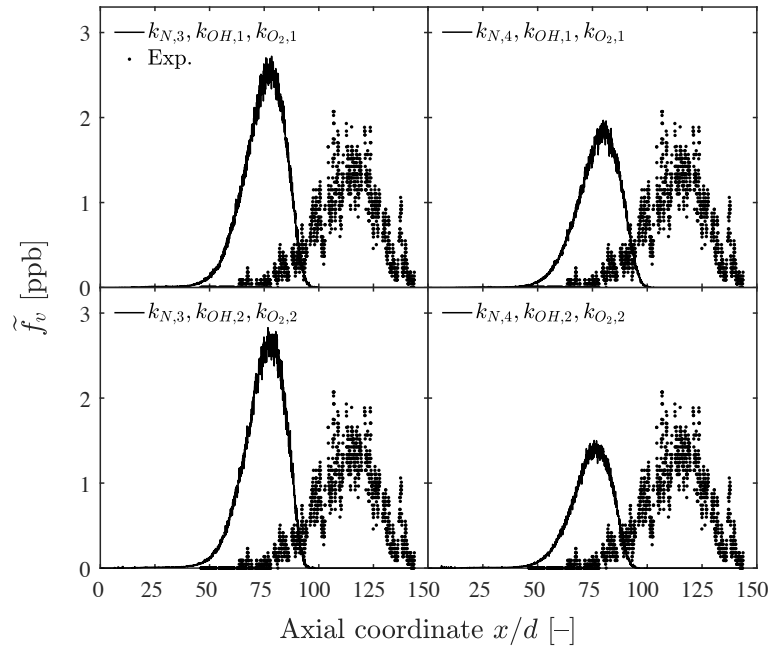


Figure 4.15: Centre-line profiles of Favre mean of soot volume fraction in the Delft III / Adelaide flame. Comparison of predictions (—) from the two-equation model to experimental data (·) by Qamar et al. [113]. The "Model 2" fuel composition was used for calculations (see Table 4.1).

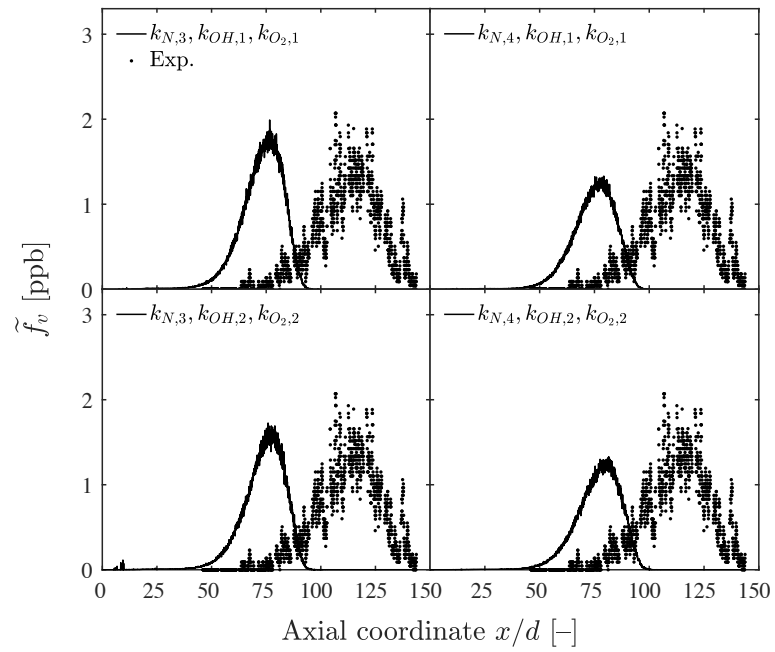


Figure 4.16: Centre-line profiles of Favre mean of soot volume fraction in the Delft III / Adelaide flame. Comparison of predictions (—) from the method of moments model with interpolative closure to experimental data (·) by Qamar et al. [113]. The "Model 2" fuel composition was used for calculations (see Table 4.1).

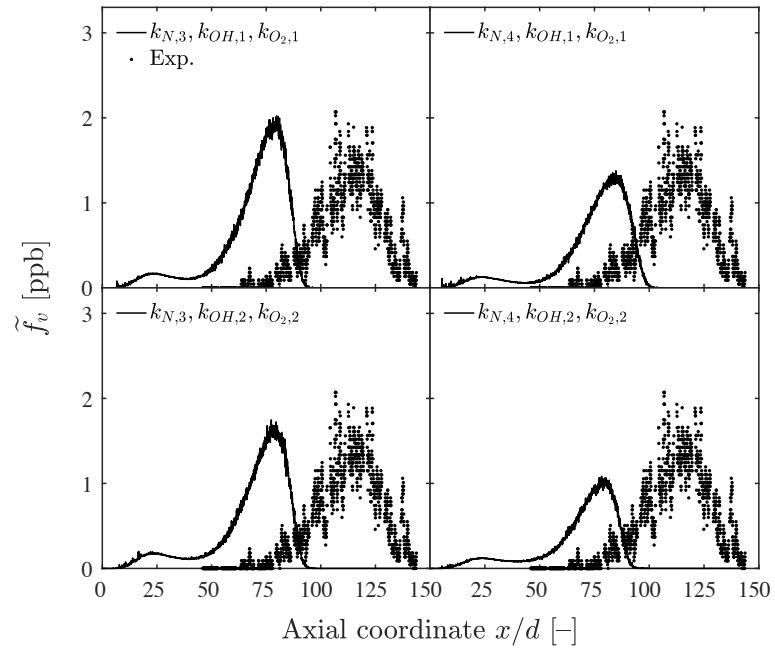


Figure 4.17: Centre-line profiles of Favre mean of soot volume fraction in the Delft III / Adelaide flame. Predictions (—) from the two-equation model including the PAH analogy model for soot surface chemistry with $\alpha_s = 0.50$. Comparison to experimental data (·) by Qamar et al. [113]. The "Model 2" fuel composition was used for calculations (see Table 4.1).

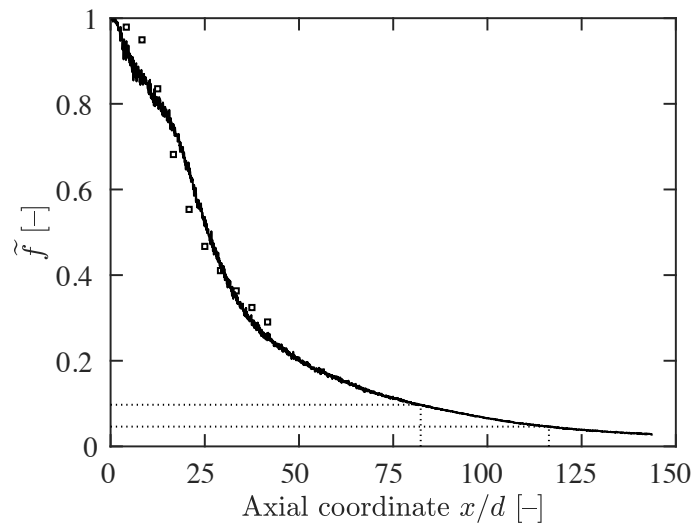
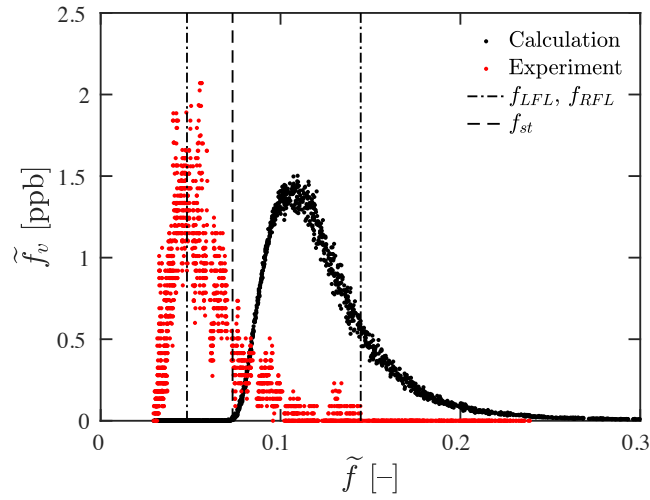
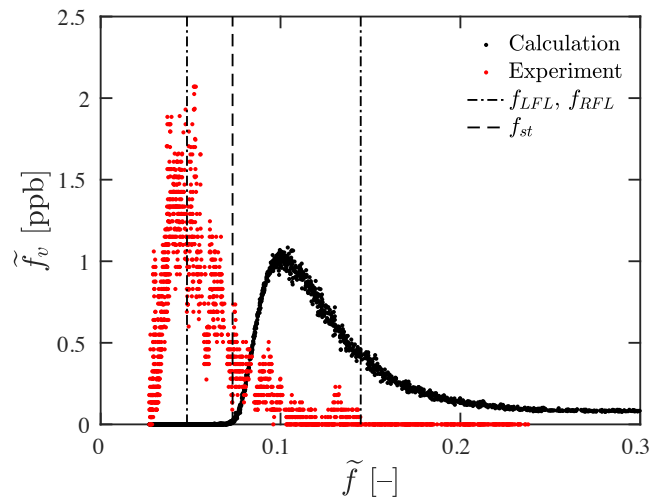


Figure 4.18: Centre-line profile of calculated Favre mean mixture fraction (—) in the Delft III / Adelaide flame. Soot peak locations from calculations at $x/d \approx 82$ and measurements at $x/d \approx 116$ and corresponding calculated mixture fraction shown as (\cdots). Comparison to experimental data (\square) by Nooren et al. [21, 22]. The "Model 2" fuel composition was used for calculations (see Table 4.1).



(a)



(b)

Figure 4.19: Favre mean soot volume fraction at the centre-line in mixture fraction space in the Delft III / Adelaide flame. Predictions from the two-equation model with $k_{N,4}$, k_O , $k_{OH,2}$, $k_{O_2,2}$. (a) The standard growth step and (b) the PAH analogy for soot surface chemistry were used. Comparison to experimental data by Qamar et al. [113], where the mapping to mixture fraction was obtained from the respective calculations. The lean and rich flammability limits of methane f_{LFL} , f_{RFL} and the stoichiometric mixture fraction for the Adelaide natural gas f_{st} are shown for comparison. The "Model 2" fuel composition was used for calculations (see Table 4.1).

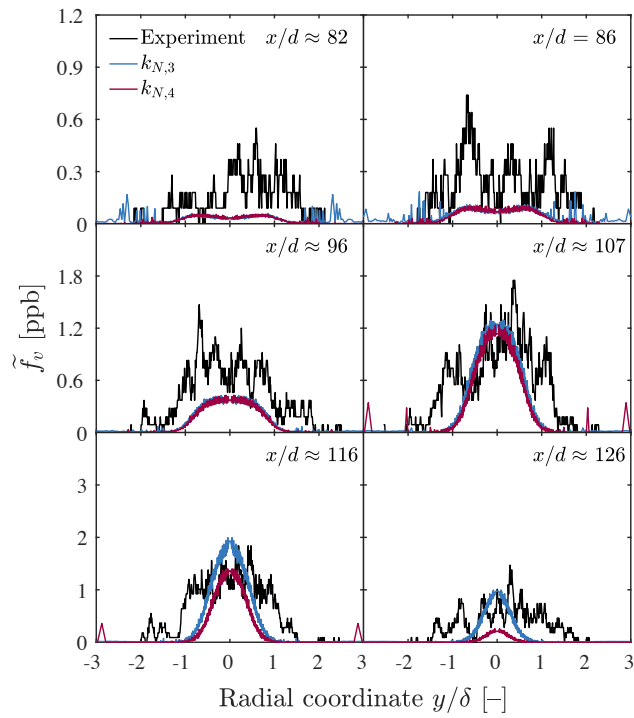


Figure 4.20: Radial profiles of Favre mean of soot volume fraction in the Delft flame. Comparison of computations featuring the two-equation model with experimental data (black lines) by Qamar et al. [113]. The rates k_{O} , $k_{\text{OH},2}$, $k_{\text{O}_2,2}$ and either $k_{N,3}$ (blue lines) or $k_{N,4}$ (red lines) were used for calculations. The axial locations of the measured profiles are shown, with the computed data corresponding to locations $36 x/d$ further upstream and the radial locations normalised, to account for the difference in peak locations and the rate of spread of the jet. The "Model 2" fuel composition was used for calculations (see Table 4.1).

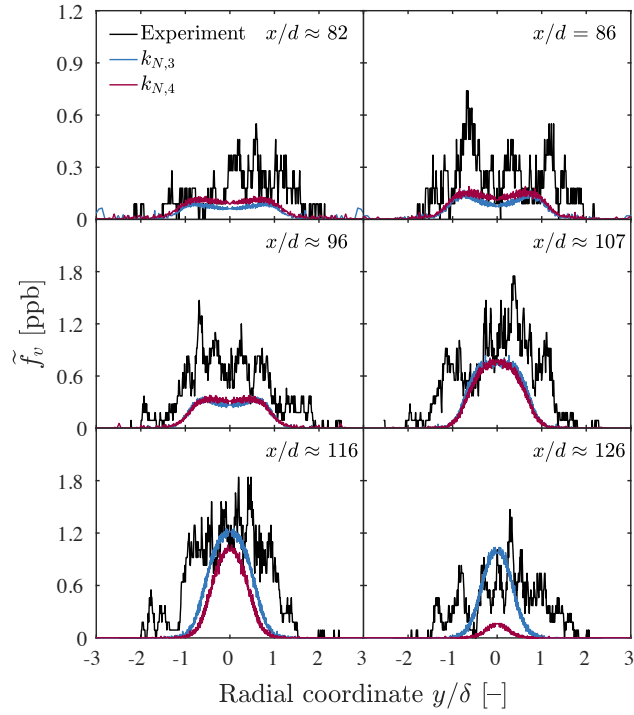


Figure 4.21: Radial profiles of Favre mean of soot volume fraction in the Delft flame. Comparison of computations featuring the two-equation model and the PAH analogy for soot surface chemistry with $\alpha_s = 0.50$ with experimental data (black lines) by Qamar et al. [113]. The rates $k_O, k_{OH,2}, k_{O_2,2}$ and either $k_{N,3}$ (blue lines) or $k_{N,4}$ (red lines) were used for calculations. The axial locations of the measured profiles are shown, with the computed data corresponding to locations $36 x/d$ further upstream and the radial locations normalised, to account for the difference in peak locations and the rate of spread of the jet. The "Model 2" fuel composition was used for calculations (see Table 4.1).

4.4. Conclusions

In Chapter 3, a sectional approach [13, 15] was used to determine an approximate acetylene based soot nucleation rate that is broadly consistent with experimental data for the evolution of the soot PSD in the WSR/PFR configuration of Manzello et al. [17, 18] and that computed using pyrene as the nucleating species [13]. The rate was then applied directly to the modelling of the Delft III / Adelaide turbulent natural gas flame using a transported PDF based approach combined with two-equation and method of moments based methods [24] for the soot particle dynamics. The sensitivity of computed soot levels was assessed for both geometries. The following conclusions are drawn:

- The derived nucleation rates provide broadly consistent results for both the WSR/PFR configuration and the Delft flame, despite using parent fuels (C_2H_4 and natural gas/ CH_4 , respectively) with very different sooting characteristics in very different experimental geometries. The change of fuel from C_2H_4 to natural gas (effectively CH_4) presents a significant step, from a soot nucleation chemistry point of view. While the generality of the simplified acetylene-based nucleation descriptions remains conjectural, the current results suggests that it may be possible to derive simplified descriptions of greater applicability than expected.
- The location of peak soot was consistently predicted approximately 40 d upstream from the measured axial position. This finding is in agreement with previous LES studies [114, 115], where it was attributed it to uncertainties in the PAH chemistry. In the current work, the magnitude of the soot concentration in the flame was found to be dependent on the nucleation rate, while the physical downstream location where soot appears is broadly unaffected.
- It was confirmed that previous rates for the acetylene based nucleation model [23, 27] are too high as suggested by Sunderland et al. [74, 76] and Lin et al. [75].
- An update of the soot oxidation model used in previous work [15, 30], to reflect the recent evaluation by Guo et al. [82], was considered. Only a moderate influence was found in the Delft flame.
- The agreement obtained for the latter for velocity, temperature and the mass fractions of major species with measurements by Stroomer et al. [112] and Nooren et al. [21, 22] was found to be fair with some discrepancies close to

the nozzle attributed to the pilot model.

- Considering soot volume fraction levels, acceptable quantitative agreement with experimental measurements by Qamar et al. [113] was found, with the maximum at the centre-line approximately matched with the nucleation rate $k_{N,3}$, for both the two-equation and the method of moments based approaches.
- The computed radial profiles of soot were compared with experimental data by accounting for the differences in peak location and rate of spread of the jet by tracking the location where the mixture fraction reaches 50% of its maximum value at a each radial location. The resulting comparisons are tentative, but show arguably good agreement between computations and measurements.
- The impact of the inclusion of the PAH based analogy for soot surface reactions by Lindstedt and Louloudi [30] was also evaluated. For a value of the surface reactivity parameter $\alpha_s = 0.50$ the peak soot volume fraction was slightly underpredicted when the updated oxidation rates and $k_{N,4}$ were used. The value of α compares to 0.75–1.0 used by Lindstedt and Louloudi [30] for turbulent non-premixed ethylene flames and 0.2–0.6 reported by Kazakov et al. [81] for laminar premixed ethylene flames. A marked reduction in the sensitivity to the nucleation rate was also observed with the growth model including soot surface reactions.

5. Soot Modelling in the Sandia Turbulent Ethylene Diffusion Flame

5.1. Introduction

The introduction of two additional equations for soot mass and number density [23, 27] into reacting flow models offers an inexpensive method of modelling soot, which does not rely on detailed chemical reaction mechanisms including PAHs. In previous work [27, 28, 30], the treatment of soot growth and oxidation as proportional to either the surface area of soot particles or the number density of soot particles was investigated. In this chapter, two-equation soot modelling is considered further, with the Sandia turbulent ethylene diffusion flame chosen as the validation case. The flame has been selected as a target for the International Sooting Flame (ISF) Workshop [111]. Past work [30] relied upon older data sets [32, 33] for validation, and the current flame arguably provides more reliable data. The effect of the treatment of soot particle surface area dependence in growth and oxidation models, along with the influence of changes to the soot oxidation and nucleation rates, as discussed in Chapters 3 and 4, are evaluated. The investigation in Chapter 4 is complemented by extending the work on a turbulent natural gas jet flame with joint scalar transported PDF calculations of a turbulent ethylene flame. Further, the importance of including aggregation into fractal aggregates and coagulation/aggregation in the continuum regime is investigated, and a functional form for the surface reactivity parameter α_s in the PAH analogy model for soot surface growth is explored.

5.2. Case Configuration

The Sandia ethylene diffusion flame at a Reynolds number of $Re = 20,000$ ("the Sandia flame") [25, 26, 123] features a main fuel jet of pure ethylene, with exit diameter $d = 3.2$ mm and bulk velocity $U = 54.7$ m s⁻¹. It is one of a family of

ethylene flames at Reynolds numbers of 10,000–25,000 generated using the same burner, with a JP-8 surrogate flame at $Re = 20,000$ on a similar burner designed for liquid fuels complementing the set [26]. Inlet conditions are prescribed at the burner exit plane, with axial velocity profiles across the fuel jet and in the air coflow set according to a fully-developed pipe and boundary layer flow, respectively, matching the experimental volumetric flow rate of 26.4 slpm of the jet and with the coflow velocity $U_\infty = 0.6 \text{ m s}^{-1}$. The pilot plate in this burner design features three concentric rows of 64 evenly distributed holes, supplying premixed ethylene/air at $\bar{\Phi} = 0.90$ corresponding to approximately 2% of the heat release of the main jet, and has been deliberately designed to create uniform flow conditions across the pilot annulus in the burner exit plane [26]. The pilot is hence modelled as a fully reacted ethylene/air mixture at the equivalence ratio reported, with a uniform velocity profile across the pilot annulus preserving the experimental mass flow of 10.63 g min^{-1} . Turbulence intensity at the inlet is set according to $u = 2 \times v = 0.01 \times U$ throughout. To obtain non-zero velocities across the burner rims, required by the parabolic flow solver to avoid re-circulation, the outer rim was included as part of the air coflow, whereas the fluid across the inner rim was set to pilot conditions with a linearly interpolated velocity profile. The velocity across the pilot annulus was reduced accordingly.

For this flame, the conventional dissipation rate closure for scalar mixing ((1.3)) was used, with a value of $C_\phi = 2.3$ in line with the work of Lindstedt and Louloudi [28, 30, 40], as the pilot arrangement did not lead to strong local extinction. The gas phase chemistry was modelled via the reduced chemical reaction mechanism also used in the calculations of the Delft flame in Chapter 4, as presented in Section 2.9. The domain was discretised via 800 control volumes in the radial direction, with initially 67 cells in the central fuel jet and 30 cells across the pilot zone assuring a sufficient resolution in both physical and stream function space. A calculated temperature map and details of the grid are depicted in Fig. 5.1. The rapid radial expansion of the grid at the interface of the central jet and pilot streams close to the nozzle is a result of the stream function distribution at the inlet plane. Downstream from the nozzle, the radial distribution of control volume quickly becomes more even. Test calculations with a further refined grid in the pilot zone at the inlet were performed, but no noticeable effect on results downstream was observed. Calculations featured a minimum of 100 stochastic particles per cell and were carried out on 20 cores.

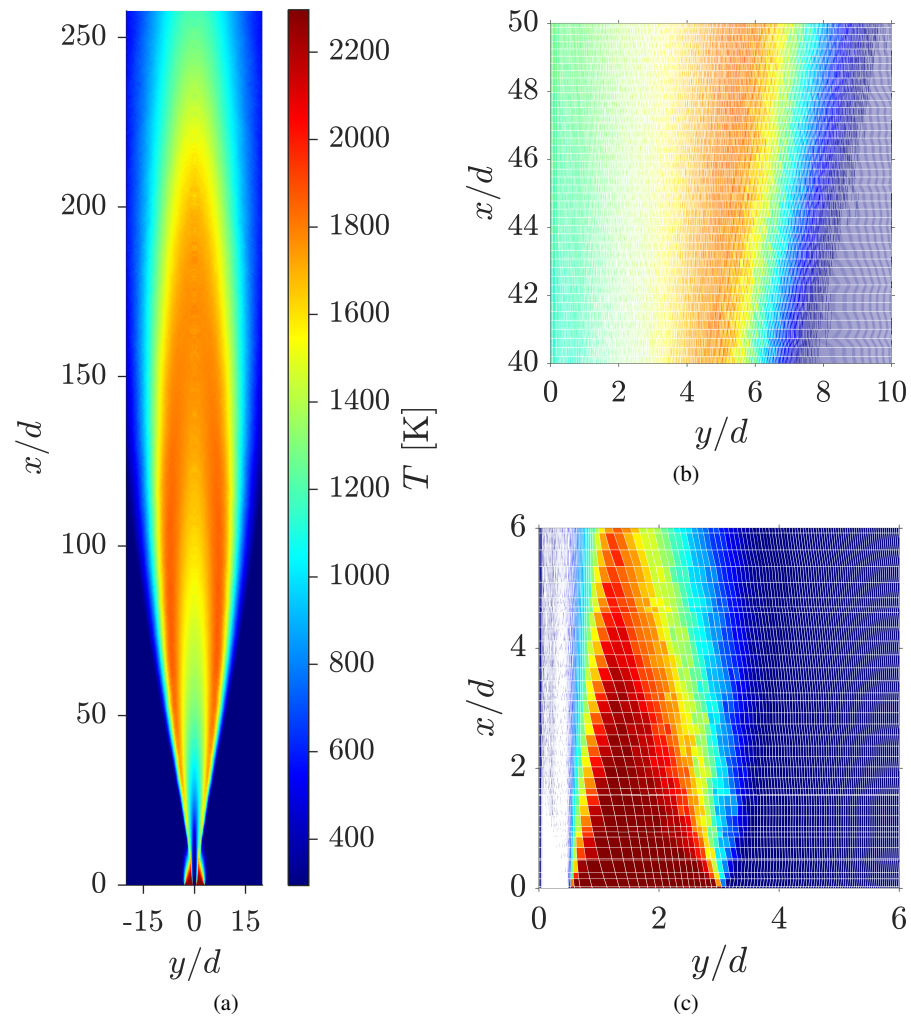


Figure 5.1: (a) Calculated temperature map in the Sandia flame. (b) Grid detail at $40 \leq x/d \leq 50$. (c) Grid detail near the nozzle. Control volume boundaries are shown with white lines.

Table 5.1: Overview of calculations modelling nucleation via $k_{N,1}$ [27] or $k_{N,5}$ [23].

Case	Growth	Surface chemistry	α_s	Oxidation	$k_{N,i}$	$k_{G,j}$	$k_{OH,k}, k_{O,k}, k_{O_2,k}$
1	DSA	No	-	DSA	$k_{N,1}$	$k_{G,1}$	$k_{i,2}$
2	DSA	Yes	0.35	DSA	$k_{N,1}$	$k_{G,2}$	$k_{i,2}$
3	ISA	No	-	ISA	$k_{N,1}$	$k_{G,3}$	$k_{i,3}$
4	ISA	Yes	0.35	ISA	$k_{N,1}$	$k_{G,4}$	$k_{i,3}$
5	ISA	No	-	ISA	$k_{N,1}$	$k_{G,3}$	$k_{i,4}$
6	ISA	Yes	0.35	ISA	$k_{N,1}$	$k_{G,4}$	$k_{i,4}$
7	PSSA	No	-	DSA	$k_{N,5}$	$k_{G,5}$	$k_{i,2}$
8	PSSA	No	-	DSA	$k_{N,1}$	$k_{G,5}$	$k_{i,2}$
9	PSSA	Yes	0.47	DSA	$k_{N,1}$	$k_{G,6}$	$k_{i,2}$

Table 5.2: Overview of calculations with updated nucleation rates.

Case	Growth	Surface chemistry	α_s	Oxidation	$k_{N,i}$	$k_{G,j}$	$k_{O,k}, k_{OH,k}, k_{O_2,k}$
1b	DSA	No	-	DSA	$k_{N,3}$	$k_{G,1}$	$k_{i,2}$
2b	DSA	Yes	0.85	DSA	$k_{N,3}$	$k_{G,2}$	$k_{i,2}$
5b	ISA	No	-	ISA	$k_{N,6}$	$k_{G,3}$	$k_{i,4}$
6b	ISA	Yes	0.90	ISA	$k_{N,6}$	$k_{G,4}$	$k_{i,4}$
8b	PSSA	No	-	DSA	$k_{N,7}$	$k_{G,5}$	$k_{i,2}$
9b	PSSA	Yes	1.00	DSA	$k_{N,7}$	$k_{G,6}$	$k_{i,2}$

5.3. Overview of Growth/Oxidation Model Assumptions and Reaction Rates

In this chapter, the three different functional forms for the dependence of soot mass growth and oxidation on the soot surface area discussed in Section 2.6 are considered. For the assumption of proportionality of growth and oxidation to the soot surface area A_s via Eq. (2.66), and proportionality to the number density $[\rho N_s]$ via Eq. (2.65), the terms "DSA" (dependant on surface area) and "ISA" (independent of surface area), respectively, coined in the work by Louloudi [28] are retained for consistency. Leung et al. [23] modelled soot growth as proportional to the square-root of the surface area of soot, corresponding to Eq. (2.67), for which the acronym "PSSA" will be used here. Where growth is modelled via the PSSA assumption, DSA oxidation has been assumed, as in the original work by Leung et al. [23].

An overview of the calculations discussed in this chapter is given in Tables 5.1 and 5.2, with the corresponding reaction rate constants for soot nucleation, growth

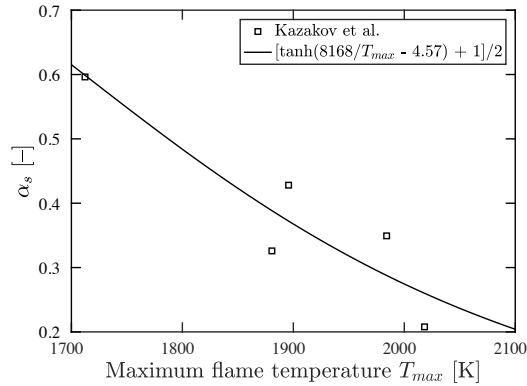
and oxidations shown in Tables 5.3–5.6. The different sets of oxidation rates $k_{O,k}$, $k_{OH,k}$, $k_{O_2,k}$ are termed $k_{i,k}$ in this chapter, where the set $k_{i,2}$ denotes the updated rates $k_{O,2}$, $k_{OH,2}$, $k_{O_2,2}$ discussed in Chapters 3 and 4, and the unchanged rate k_O is denoted $k_{O,2}$ for consistency in notation. Calculations using a growth model via a single acetylene addition rate, as defined in Eq. (2.36), and using the PAH analogy model for soot growth by Lindstedt and Louloudi [30] (Eq. (2.57)) are presented.

The nucleation rate $k_{N,1}$ [28, 30] serves as a starting point, and the rates for Cases 1–4 correspond most closely to those in previous work by Louloudi [28], with the oxidation rates $k_{i,2}$ evaluated in Chapters 3 and 4 being introduced. The growth rate $k_{G,2} = k_X^f$ represents the acetylene addition rate in the soot surface chemistry model, and the corresponding rates $k_{G,4}$ and $k_{G,6}$ were obtained via a scaling relationship. The oxidation rates $k_{i,3}$ were adapted from Louloudi [28], by introducing updates corresponding to the rates $k_{i,2}$ and appropriate scaling, and the rates $k_{i,4}$ represent a further improvement for the ISA assumption discussed below. The ISA assumption is functionally equivalent to calculating reaction rate source terms based on an assumed particle surface area A_p constant throughout the flame, included in the pre-exponential factor of the reaction rate constant. Analogous to the ISA growth rates $k_{G,2}$ and $k_{G,4}$, this set is calculated based on the DSA rates, scaled by assuming a constant diameter d_p , as $k_{i,3} = \pi d_p^2 k_{i,1}$. A value of $d_p = 20.6$ nm, close to that of a primary particle, is assumed in line with the ISA growth rates from previous work [28], whereas the original expressions $k_{i,3}$ focussed on the oxidation of much smaller (incipient) particles with $d_p = 1$ nm.

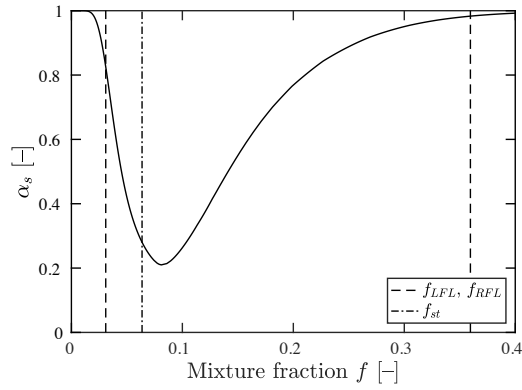
In Case 7, the original nucleation and growth reaction rate constants from Leung et al. [23] are used, whereas Case 8 explores the use of the only slightly lower rate $k_{N,1}$ by Lindstedt [27] with the PSSA assumption. In the former case, and in line with Leung et al. [23], the parameter value $C_{min} = 100$ is used (see Eq. (2.31)), whereas it takes the value $C_{min} = 60$ [27] for the latter and all other cases.

The nucleation rate $k_{N,3}$ proposed in Chapters 3 and 4 is introduced in Cases 1b and 2b. The sensitivity to the nucleation rate is explored, and $k_{N,6}$ and $k_{N,7}$ are obtained empirically to match peak soot at the centre-line for the ISA and PSSA assumptions and the current flame.

The surface reactivity parameter α_s expresses the fraction of sites on the surface of soot particles available for reaction with gas phase species. Fundamentally, it reflects the history of reactions on the surface of the individual soot particles. For modelling purposes, a constant value is often prescribed, although the dependence of α_s on flame conditions is recognized (e.g. [79]), and a range of functional forms



(a)



(b)

Figure 5.2: (a) Functional dependence of α_s on the maximum temperature of laminar flames by Kazakov et al. [81]. (b) Mixture fraction dependence of the surface reactivity parameter α_s , based on the functional dependence and a laminar diffusion flamelet approximation with a strain rate of 100 s^{-1} .

for the mean reactivity parameter derived from laminar flames has been proposed [77, 81, 124–139]. For cases where growth is modelled via the PAH surface chemistry model, a sensitivity analysis to the surface reactivity parameter α_s was carried out. The cases shown were obtained with the empirically optimised constant values of α_s stated in Tables 5.1 and 5.1. Based on a fit to optimised values of α_s in premixed laminar flame calculations, Kazakov et al. [81] proposed a functional form for the surface reactivity as a decreasing function of maximum flame temperature T_{max} , with $\alpha_s = \tanh(8168/T_{max} - 4.57) + 1/2$. In the current work, a mapping of the function by Kazakov et al. [81] to the mixture fraction in non-premixed flames via

a laminar diffusion flamelet approximation was evaluated, where T_{max} is equated to the local temperature across the flamelet in mixture fraction space. The resulting functional form of α_s in mixture fraction space is shown in Fig. 5.2. The adiabatic laminar flame calculation featured a strain rate of approximately 100 s^{-1} , as soot tends to form in low strain regions.

Table 5.3: Reaction rate constants for soot nucleation via Eq. (2.29) presented in the form $k_{N,i} = A_i \exp(-E_i/RT)$. Units are in K, kmol, m^3 and s.

k_i	A_i	α_i	β_i	E_i/R	Source
$k_{N,1}$	6.30×10^3	1	0	21,000	Lindstedt [27]
$k_{N,3}$	6.30×10^1	1	0	21,000	Current work
$k_{N,5}$	1.00×10^4	1	0	21,100	Leung et al. [23]
$k_{N,6}$	1.89×10^3	1	0	21,000	Current work
$k_{N,7}$	2.02	1	0	21,000	Current work

Table 5.4: Reaction rate constants for soot growth and oxidation for $f(A_s) = A_s$ (DSA) presented in the form $A_i \alpha_i T^{\beta_i} \exp(-E_i/RT)$ [27, 28]. Units are in K, kmol, m^3 and s.

k_i	A_i	α_i	β_i	E_i/R
$k_{G,1}$	7.50×10^2	1	0	12,100
$k_{G,2}$	3.57×10^{21}	1	-3.176	7,471
$k_{O,2}$	9.09	0.2	1/2	0
$k_{OH,2}$	8.82	0.1	1/2	0
$k_{O_2,2}$	6.43	116	1/2	19,680

Table 5.5: Reaction rate constants for soot growth and oxidation for $f(A_s) = [\rho N_s]$ (ISA) presented in the form $A_i \alpha_i T^{\beta_i} \exp(-E_i/RT)$ [27, 28]. Units are in K, kmol, m^3 and s.

k_i	A_i	α_i	β_i	E_i/R
$k_{G,3}$	1.00×10^{-12}	1	0	12,100
$k_{G,4}$	4.76×10^6	1	-3.176	7,471
$k_{O,3}$	2.86×10^{-17}	0.2	1/2	0
$k_{OH,3}$	2.77×10^{-17}	0.1	1/2	0
$k_{O_2,3}$	2.02×10^{-17}	116	1/2	19,680
$k_{O,4}$	1.21×10^{-14}	0.2	1/2	0
$k_{OH,4}$	1.18×10^{-14}	0.1	1/2	0
$k_{O_2,4}$	8.57×10^{-15}	116	1/2	19,680

Table 5.6: Reaction rate constants for soot growth for $f(A_s) = \sqrt{A_s}$ (PSSA) presented in the form $A_i \alpha_i T^{\beta_i} \exp(-E_i/RT)$ [27, 28]. Units are in K, kmol, m^3 and s.

k_i	A_i	α_i	β_i	E_i/R
$k_{G,5}$	6.00×10^3	1	0	12,100
$k_{G,6}$	2.86×10^{22}	1	-3.176	7,471

5.4. Results and Discussion

5.4.1. Scalar Fields

Figure 5.3 presents calculated radial profiles of OH Favre mean mass fraction in comparison to measured values by Shaddix [140] in arbitrary units. The experimental data has been normalised to match the calculated peak value at $x/d = 23$. It hence only allows a qualitative comparison. Peak OH locations appear to be generally well-matched, with the calculated locations at $23 \leq x/d \leq 86$ shifted moderately outward in comparison to the measurements. In the region $86 \leq x/d \leq 148$, absolute values appear high in comparison the regions further up- and downstream.

Radial profiles of the calculated Favre mean temperature are compared to measured soot temperature in Fig. 5.4. Agreement in peak values is reasonable, but qualitatively the profiles match poorly. As no measurements of the gas phase temperature are available for a direct comparison, no definite conclusion can be drawn.

In Fig. 5.5, radial profiles of Favre mean mass fraction of acetylene are compared to measured PAH mass fractions. As for Fig. 5.3, the experimental data is supplied in arbitrary units, and hence scaled to match the calculated peak value at

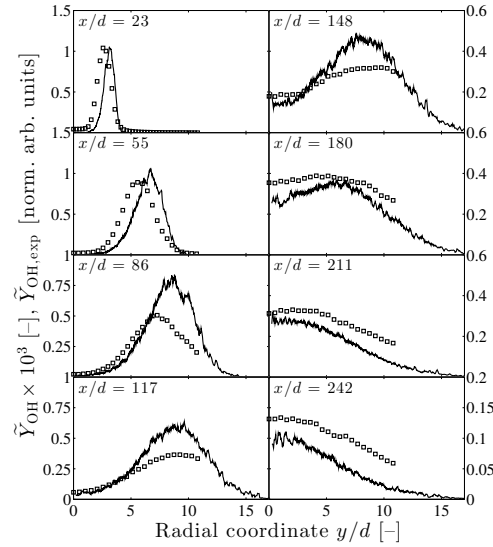


Figure 5.3: Radial profiles of calculated (—) Favre mean mass fraction of OH in the Sandia flame and measured (\square) OH mass fraction in normalised arbitrary units. Calculated data is smoothed via a centred moving average filter with window size $0.2 d$. Comparison to experimental data by Shaddix [140].

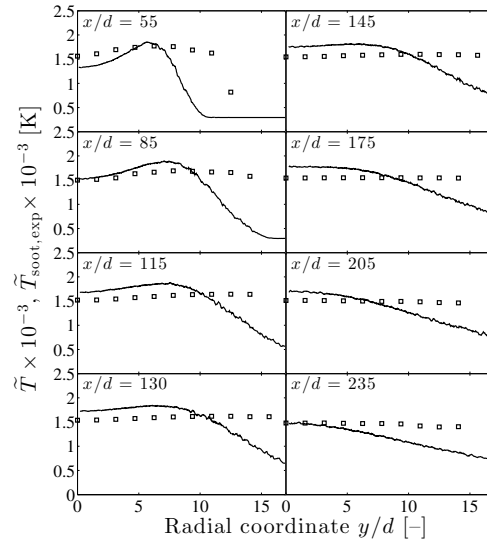


Figure 5.4: Radial profiles of calculated Favre mean temperature in the Sandia flame and measured soot temperature. Calculated data is smoothed via a centred moving average filter with window size $0.2 d$. Lines and symbols as in Fig. 5.3. Comparison to experimental data by Shaddix [140].

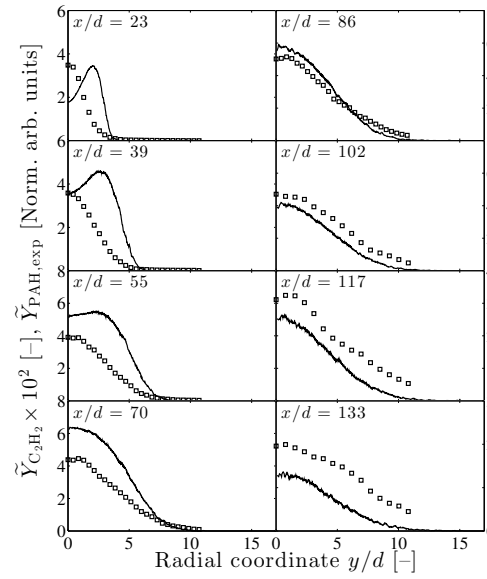


Figure 5.5: Radial profiles of calculated Favre mean mass fraction of C_2H_2 in the Sandia flame and measured PAH mass fraction in normalised arbitrary units. Calculated data is smoothed via a centred moving average filter with window size $0.2 d$. Lines and symbols as in Fig. 5.3. Comparison to experimental data by Shaddix [140].

the first measurement location. The comparison may indicate a limitation of acetylene based nucleation models for the current flame, as the maximum PAH mass fraction is found at or near the centre-line throughout, whereas the peak in C_2H_2 shifts from the jet flanks at $23 \leq x/d \leq 39$ towards the centre. However, the qualitative agreement improves significantly further downstream.

5.4.2. Soot Statistics

In Fig. 5.6, calculated Favre mean and RMS of soot volume fraction at the centre-line of the Sandia flame are presented for Case 1. Surface growth and oxidation were considered proportional to soot surface area (DSA) in this calculation. For the original growth model the peak of the mean soot volume fraction is overpredicted by approximately a factor of four, with the location of the peak about $40 d$ further upstream than measured. Predictions of RMS values take values of approximately 50 % of the predicted Favre mean at the respective position, whereas the measured RMS values are of almost equal magnitude to the mean upstream of the peak soot location, and surpass it further downstream. In Fig. 5.6b, predictions for Case 2 obtained using the PAH analogy soot surface chemistry for growth by Lindstedt and Louloudi [30] (Eq. (2.37)) are presented. Here the value of the surface reactivity was optimised, and a value of $\alpha_s = 0.35$ was found to lead to good agreement with the measured peak soot at the centre-line. Qualitative agreement

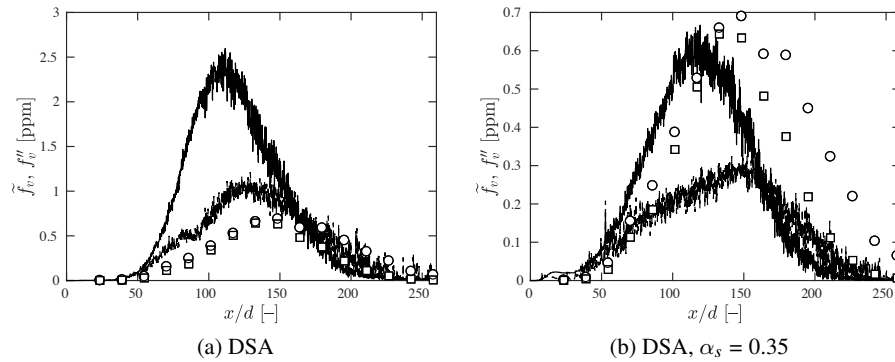


Figure 5.6: Predictions of Favre mean (—) and RMS (---) of soot volume fraction at the centre-line of the Sandia flame. (a) Case 1, (b) Case 2. Soot mass growth and oxidation are modelled as proportional to the soot surface area (DSA). Comparison to measured mean (\square) and RMS (\circ) from [141].

of predicted mean soot volume fraction with the experiment is good for Case 2, and improved compared to calculations without surface chemistry (Fig. 5.6a) with the peak soot location shifted upstream by merely $10 d$. For the case of surface-independent calculation of growth and oxidation (ISA, Fig. 5.7), the peak soot value is overpredicted by a factor of 2, with elevated levels of soot in the zone $x/d \leq 50$, a pronounced overprediction of soot downstream from the peak location, and the magnitude of soot volume fraction RMS further reduced compared to the mean. The present rates for surface-independent oxidation hence appear too low. Further, the surface-independent growth model appears to lead to exaggerated levels of soot upstream in the flame, where the number density is comparatively high. The predictions using the extended growth model presented in Fig. 5.7b exhibit an even greater overprediction of soot near the nozzle, which may indicate an overestimation of the sensitivity to the soot number density in the ISA growth model upstream.

In Fig. 5.8, results obtained from calculations using the ISA assumption with the modified oxidation rates $k_{O,3}$, $k_{OH,3}$, $k_{O_2,3}$ are presented. Compared to the cases using $k_{O,2}$, $k_{OH,2}$, $k_{O_2,2}$, the overall balance of soot production and oxidation across the whole flame is restored with regard to the mean volume fraction, while the overprediction of soot upstream due to the effect of the ISA assumption on growth is unaffected. The peak mean soot volume fraction in the results from the original growth model, shown in Fig. 5.8a, is slightly improved compared to

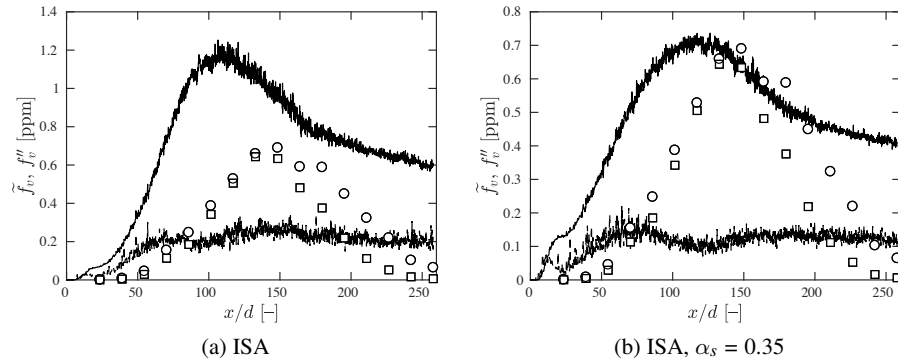


Figure 5.7: Predictions of Favre mean and RMS of soot volume fraction at the centre-line of the Sandia flame. (a) Case 3, (b) Case 4. Soot mass growth and oxidation are modelled as independent of the soot surface area (ISA). Lines and symbols as in Fig. 5.6.

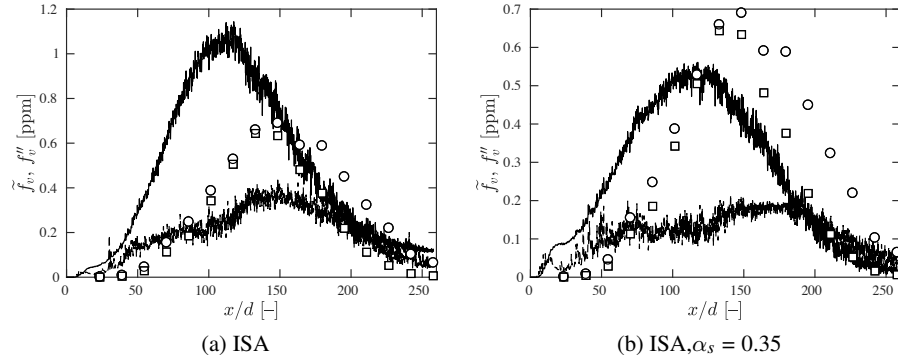


Figure 5.8: Predictions of Favre mean and RMS of soot volume fraction at the centre-line of the Sandia flame. (a) Case 5, (b) Case 6. Soot mass growth and oxidation are modelled as independent of soot surface area (ISA), with the modified oxidation rates $k_{O,3}$, $k_{OH,3}$, $k_{O_2,3}$. Lines and symbols as in Fig. 5.6.

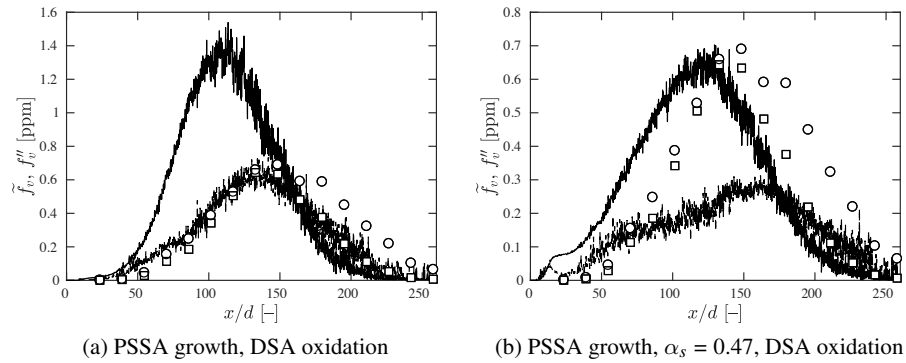


Figure 5.9: Predictions of Favre mean and RMS of soot volume fraction at the centre-line of the Sandia flame. (a) Case 8, (b) Case 9. Soot mass growth is modelled as proportional to $\sqrt{A_s}$ (PSSA), and oxidation as proportional to the soot surface area (DSA). Lines and symbols as in Fig. 5.6.

the corresponding DSA case (Fig. 5.6a), while qualitative agreement suffers for the case with soot surface chemistry presented in Fig. 5.8b compared to the DSA case (Fig. 5.7a). The qualitative agreement of the predicted RMS of soot volume fraction with experiment worsens when the ISA assumption is made compared to the corresponding DSA cases, while the absolute values of the RMS are reduced even further relative to the mean.

Predictions using the PSSA assumption for soot growth presented in Fig. 5.9 show an improved quantitative agreement with experiment in absence of the soot surface chemistry model. Excessive levels of soot near the nozzle when the latter is used is shared with Cases 2 and 4, although agreement upstream from the peak is slightly improved compared to the ISA case.

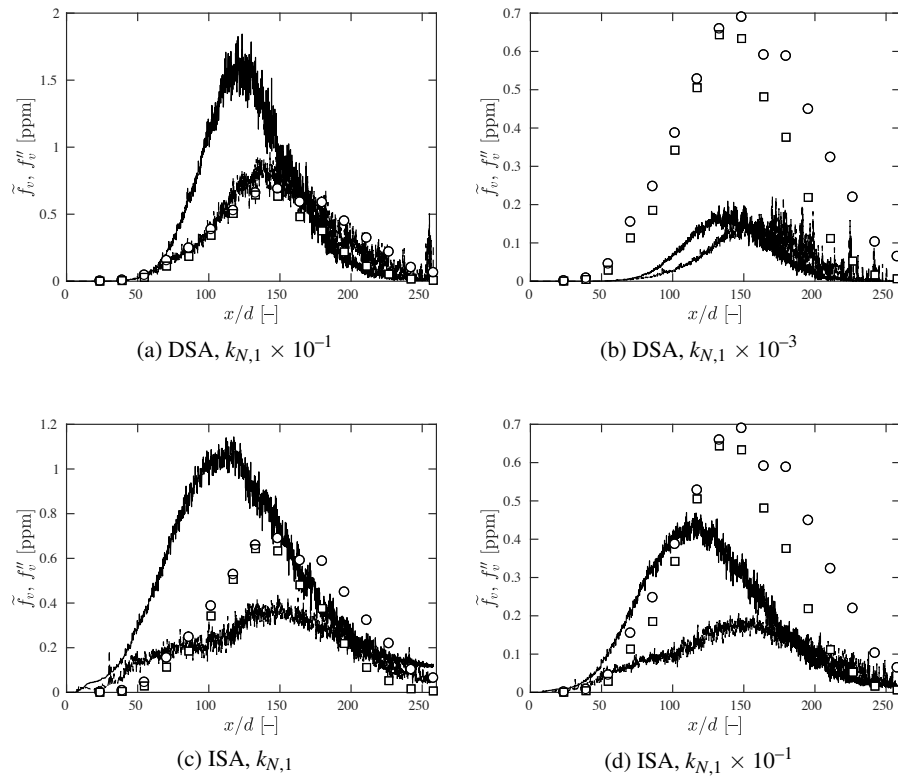


Figure 5.10: The sensitivity of soot volume fraction predictions at the centre-line of the Sandia flame to the nucleation rate. (a/b): Surface area dependent soot mass growth and oxidation based on Case 1 (DSA). (c/d): Surface area independent growth/oxidation (ISA) based on Case 5. Lines and symbols as in Fig. 5.6.

The sensitivity of the model making the DSA and ISA assumptions to the nucleation rate is illustrated in Fig. 5.10, showing predictions obtained based on Cases 1 and 5 without the soot surface growth model. Naturally, the two cases exhibit a different sensitivity to the reduced nucleation rate, with an optimal rate for the ISA assumption in this flame being about an order of magnitude greater than for the DSA assumption.

In Fig. 5.11, results obtained via the nucleation rate $k_{N,3}$ with DSA growth and oxidation are presented. With the original growth model [27], peak soot is approximately matched, with soot levels upstream and downstream from the peak appearing somewhat underpredicted. Compared to Case 1, the ratio of Favre mean to RMS is markedly closer to that observed in the experimental data. With the soot surface growth model, qualitative agreement of the mean is improved, with peak soot matched for $\alpha_s = 0.85$, although the improvement of the RMS agreement is much smaller here. The increase from $\alpha_s = 0.35$ used to match peak soot for Case 2 is required to compensate for the reduced nucleation rate in Case 2b.

Radial profiles of soot predictions obtained from Cases 1b and 2b are presented in Fig. 5.12 and Fig. 5.13, respectively. While the measured peak in soot volume fraction is approximately matched in the results from Case 1b, mean and RMS of soot are distinctly underpredicted near the nozzle, and soot oxidises too quickly downstream of the peak. Qualitative agreement is considerably improved with the introduction of the PAH analogy model for soot surface growth, included in

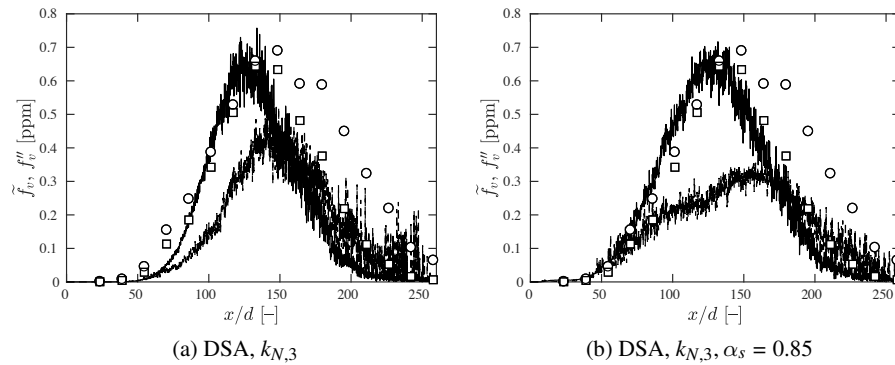


Figure 5.11: Predictions of Favre mean and RMS of soot volume fraction at the centre-line of the Sandia flame. (a) Case 1b, (b) Case 2b. Soot mass growth and oxidation are modelled as proportional to the soot surface area (DSA). Lines and symbols as in Fig. 5.6.

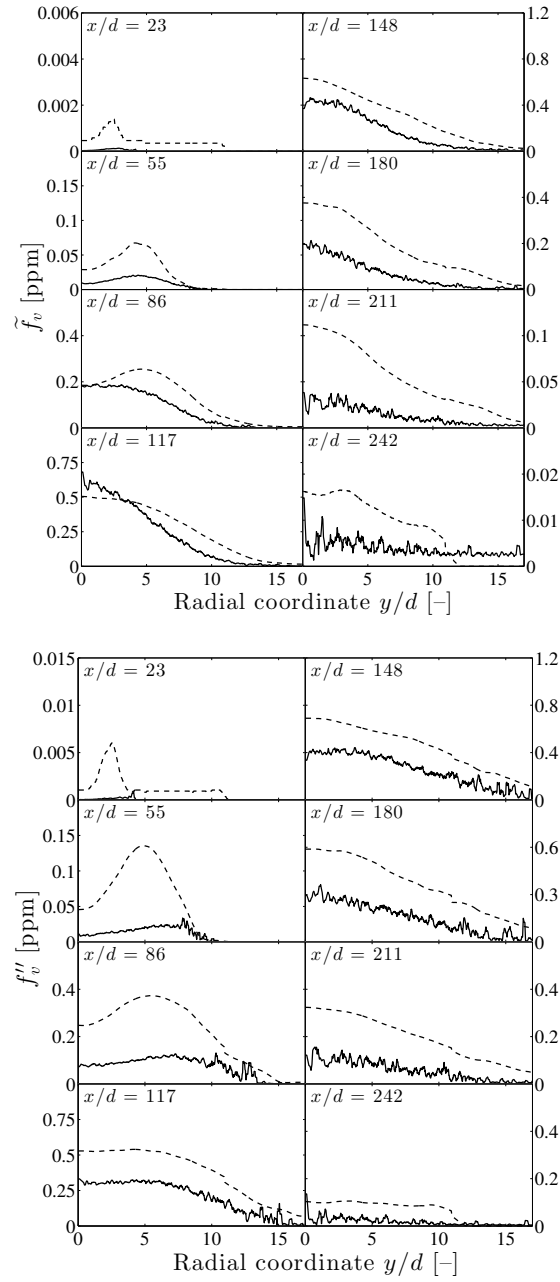


Figure 5.12: Radial profiles of (a) Favre mean and (b) RMS of soot volume fractions in the Sandia flame. Calculated data is smoothed via a centred moving average filter with window size $0.2 d$. Comparison of predictions (—) from Case 1b to experimental data (---) from [141].

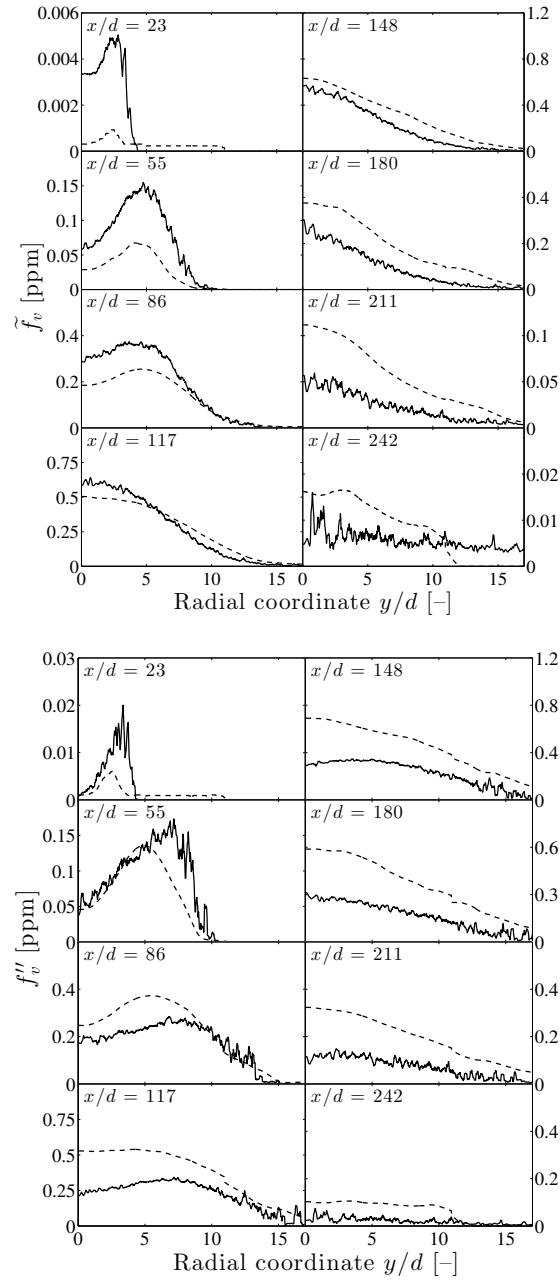


Figure 5.13: Radial profiles of (a) Favre mean and (b) RMS of soot volume fractions in the Sandia flame. Calculated data is smoothed via a centred moving average filter with window size $0.2 d$. Comparison of predictions (—) from Case 2b to experimental data (---) from [141].

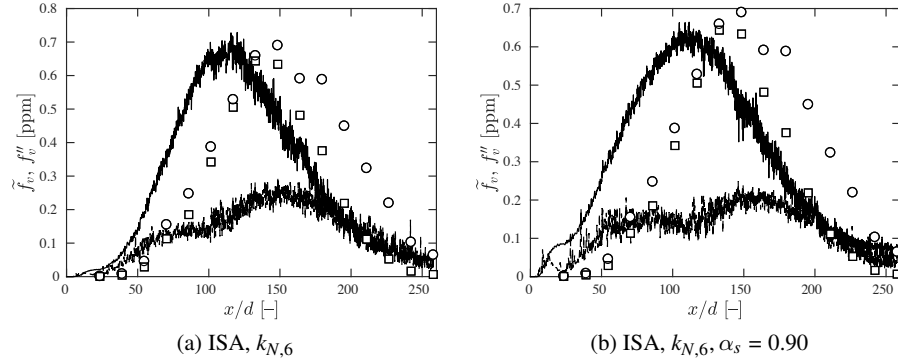


Figure 5.14: Predictions of Favre mean and RMS of soot volume fraction at the centre-line of the Sandia flame. a) Case 5b, b) Case 6b. Soot mass growth and oxidation are modelled as independent of soot surface area (ISA), with the modified oxidation rates $k_{O,3}$, $k_{OH,3}$, $k_{O_2,3}$. Lines and symbols as in Fig. 5.6.

Case 2b, with the evolution matching the experimental observations better, including the profile width in the near-peak region at $x/d = 117$. Mean soot both in the jet flanks and centre is overpredicted near the nozzle at $x/d = 23$, but the discrepancy to the experimental data is reduced subsequently, and the agreement is arguably reasonable for $86 \leq x/d \leq 148$. Further downstream, soot oxidation appears too high, but agreement is still moderately improved over Case 1b in this zone. Along with the elevated values for the mean, the RMS of soot volume fraction is approximately matching the measured data for $x/d = 55$, but the peak is exaggerated at $x/d = 23$. For $x/d \geq 86$, the calculated RMS is too low throughout, with the discrepancy increasing along the length of the flame.

In Figs. 5.14–5.15, results for the ISA and PSSA assumptions and the nucleation rates $k_{N,6}$ and $k_{N,7}$, obtained empirically for this flame, are shown. Compared to Case 1b shown in Fig. 5.11a, qualitative agreement is worsened for Case 5b, but improved for Case 8b, particularly upstream from the peak location. With the soot surface growth model, high values near or at the theoretical limit of $\alpha_s = 0.90$ (ISA) and 1.00 (PSSA) are required to match the mean soot peak, while the same tendency for soot overprediction upstream of the peak is present as for Cases 6 and 9.

Results obtained using a functional dependence of α_s on mixture fraction with both an DSA and ISA assumption based on Cases 2 and 6 are presented in Fig. 5.16, where in the latter case the updated oxidation rates $k_{O,3}$, $k_{OH,3}$, $k_{O_2,3}$ are used.

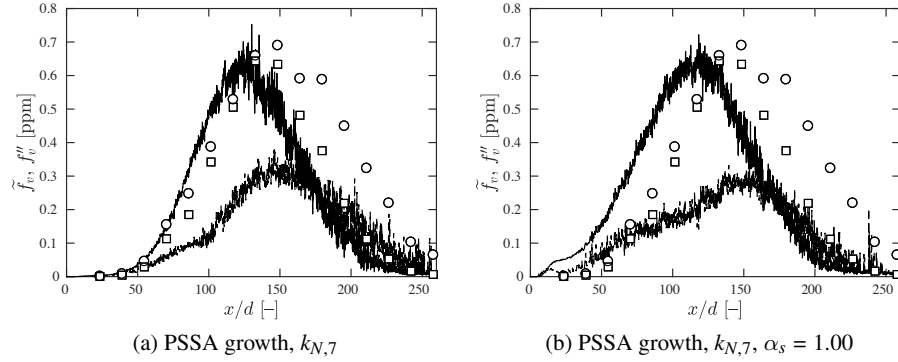


Figure 5.15: Predictions of Favre mean and RMS of soot volume fraction at the centre-line of the Sandia flame. (a) Case 8b (a) Case 9b Soot mass growth is modelled as proportional to $\sqrt{A_s}$ (PSSA), and oxidation as proportional to the soot surface area (DSA). Lines and symbols as in Fig. 5.6.

Peak soot is approximately matched in the DSA case, whereas it is underpredicted when surface area independent growth and oxidation are assumed. However, both the qualitative and quantitative agreement with experiment is very similar to that of Cases 2 and 6. While the surface reactivity parameter was adjusted to approximately match peak soot for Case 2 (and the same value was retained for Case 6), the predictions presented in Fig. 5.16 were obtained without any further adjustment to the model.

In all computations discussed above, particle dynamics are included via the full model for two-equation type approaches, including coagulation of small particles to spherical particles, the aggregation of larger particles into fractal aggregates, and models for coagulation/aggregation in the free molecular, continuum and transition regimes as a function of the Knudsen number, as described in Section 2.2. From a practical perspective, the implementation of a simplified particle dynamics model may be tempting, e.g. by modelling particle collisions exclusively as coagulation in the free molecular regime via Eq. (2.20), which constitutes the limit case for incipient and small soot particles in the current model. A set of calculations following such simplifications is presented Fig. 5.17. The results shown in Fig. 5.17a and 5.17b are obtained based on Cases 1b and 5b: The proposed update to the soot nucleation rate is included and soot growth and oxidation are modelled via the DSA and ISA assumption, respectively. Figures 5.17c and 5.17d present computations based on Cases 2 and 6: The original nucleation rate $k_{N,1}$

and the PAH analogy model for soot surface growth with $\alpha_s = 0.35$ are used, and the DSA (Fig. 5.17c) and ISA (Fig. 5.17d) assumptions are made. Finally, the calculations presented in Figures 5.17e and 5.17f are based on Cases 2b (DSA, $\alpha_s = 0.85$) and 6b ((DSA, $\alpha_s = 0.90$)) with the optimised nucleation rates $k_{N,3}$ and $k_{N,6}$. While the DSA case with the original growth step (Fig. 5.17a) is not sensitive to the simplification of the particle dynamics model, peak soot is affected for ISA growth/oxidation (Fig. 5.17b), although moderately. The calculations using the soot surface chemistry model (Figs. 5.17c–5.17e) are insensitive to the simplification, independent of the DSA/ISA assumption made. An analysis of the mean particle diameter and Knudsen number approximated from cell Favre mean properties (not shown) suggests that the deviation of the predictions for the latter case from the base cases coincides with passing from the coagulation to the agglomeration regime, which occurs at around $x/d \approx 55$ for Case 5b, but further downstream at $x/d \approx 70$ for Case 1b and at $x/d \approx 100$ for Cases 2 and 6. However, although the agglomeration regime is entered at $x/d \approx 45$ for for Cases 2b and 6b, the impact on soot mass predictions for these cases is small. Further, the continuum regimes appear to be of only minor importance for the current cases, with the mean Knudsen number >10 throughout.

From the above results, the parameter set of Case 2b can be recommended as

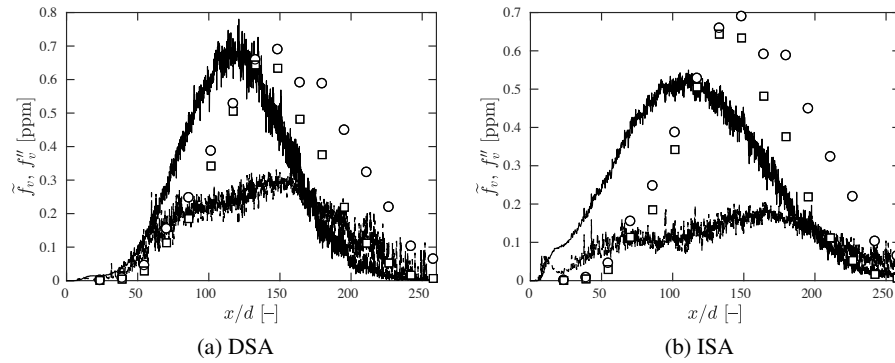


Figure 5.16: Predictions of Favre mean and RMS of soot volume fraction at the centre-line of the Sandia flame. Calculations are based on Cases 2 and 6, with a functional dependence of α_s on mixture fraction. Soot mass growth and oxidation are modelled as either dependent on (DSA) or independent of (ISA) soot surface area, the latter with the modified oxidation rates $k_{O,3}$, $k_{OH,3}$, $k_{O_2,3}$. Lines and symbols as in Fig. 5.6. 5

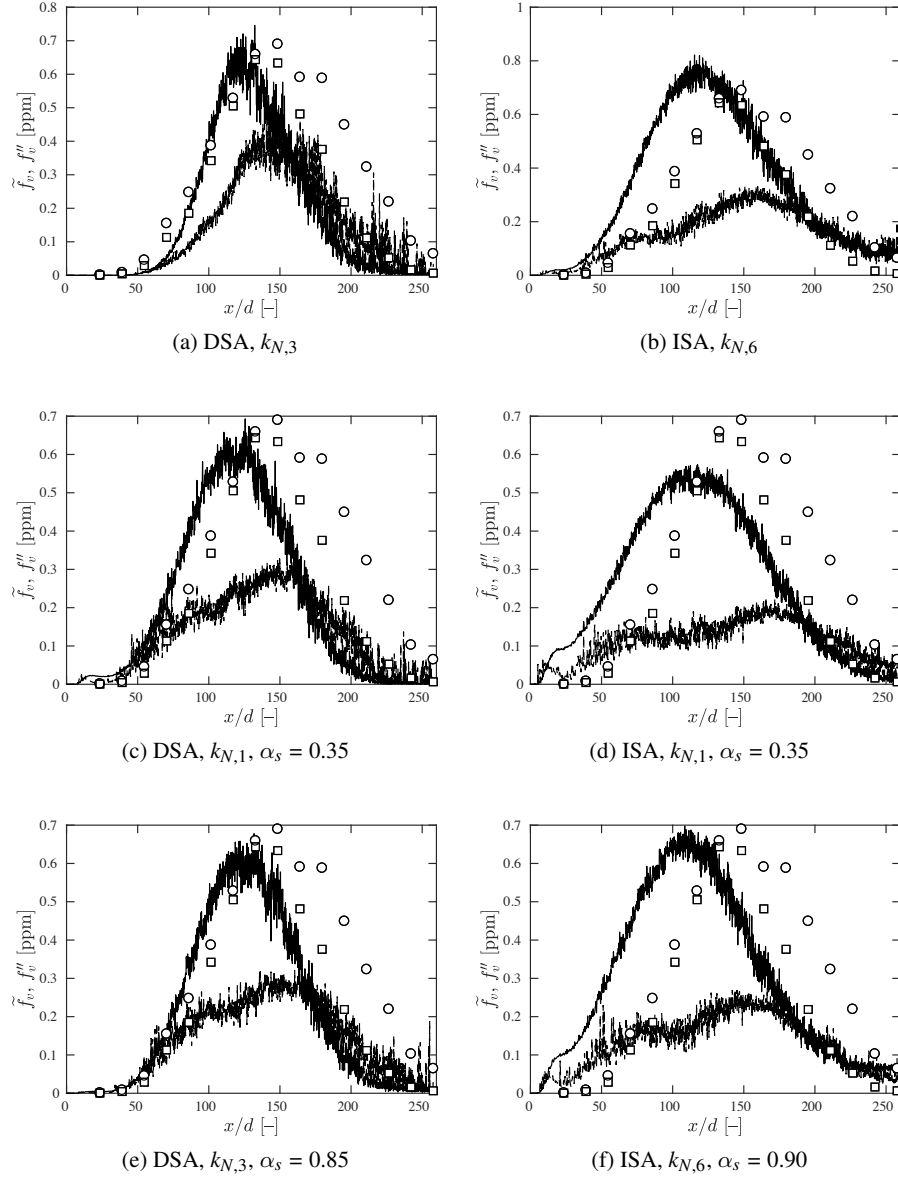


Figure 5.17: Predictions of Favre mean and RMS of soot volume fraction at the centre-line of the Sandia flame. Calculations are based on (a) Case 1b, (b) Case 5b, (c) Case 2, (d) Case 6, (e) Case 2b, (f) Case 6b, with only coagulation in the free molecular regime considered. A modified two-equation soot model with the original growth step (top row) and the soot surface chemistry growth model by Lindstedt and Louloudi [30] (middle and bottom row) is used. Lines and symbols as in Fig. 5.6.

an updated set for two-equation soot modelling: The updates to the nucleation and oxidation rates discussed in Chapter 3 are included, producing encouraging agreement consistently across all three setups. Soot growth is modelled via the PAH analogy soot surface growth model by Lindstedt and Louloudi [30] with $\alpha_s = 0.85$. By omitting the latter and modelling growth via Eq. (2.36) instead, the model and parameter set used for Case 1b offers a simpler, computationally moderately less expensive alternative, yielding good agreement of the peak mean soot value for this flame, and improved agreement for the RMS. Should an approach modelling soot growth as proportional to $\sqrt{A_s}$ be preferred, the parameter set used for Case 8b offers a starting point, yielding acceptable agreement for the Sandia flame via the empirically deduced nucleation rate $k_{N,7}$. As has been shown, the recommended model parameter set corresponding to Case 1b is contingent on the incorporation of the formation of fractal aggregates in the particle dynamics model, while the set Case 2b did not show a pronounced sensitivity to the latter in the current flame configuration.

5.5. Conclusions

Soot in the Sandia turbulent ethylene diffusion flame at $Re = 20,000$ was calculated using a two-equation soot model, both with and without a PAH analogy model [30] for soot surface growth. The effect of calculation of soot growth and oxidation as proportional to soot surface area (DSA) soot number density (ISA) or the square-root of the surface area (PSSA) was investigated. The following main findings were made and conclusions drawn:

- ISA oxidation rates used in previous work [28] appear too low for the current flame, and alternative rates for surface area independent oxidation were proposed based on a larger characteristic particle size similar to the primary particle size. With the updated rates, the growth and oxidation across the current flame is balanced also for the ISA assumption.
- Mean soot mass fraction is overpredicted if the simple growth model is used with a nucleation rate from previous work [27] and the impact of a reduction of nucleation was studied. Good agreement could be obtained with the DSA assumption and the nucleation rate $k_{N,3}$, consistent with results presented in the previous chapters in the context of PSD predictions in a WSR/PFR setup and a turbulent natural gas diffusion flame. The nucleation rate sensitivity when

making the ISA and PSSA assumptions is naturally different, and decreased nucleation rates $k_{N,6}$ and $k_{N,7}$ are required for good agreement with experiment.

- Qualitative agreement, particularly for the DSA assumption, can be achieved via the soot surface growth model by Lindstedt and Louloudi [30], although for the nucleation via $k_{N,3}$, values of the surface reactivity parameter α_s near the theoretical maximum are required for good agreement with experiment.
- A flame-independent expression for the parameter α_s based on work by Kazakov et al. [81] was implemented in turbulent flame calculations and showed promising results with agreement similar to the optimised constant value for α_s for $k_{N,1}$ and the DSA and ISA assumptions. In the context of the update nucleation rate $k_{N,3}$, where values in the range $0.85 \leq \alpha_s \leq 1.00$ are required to match the measured peak soot, the model would not perform well in its current form.
- The impact of a simplified particle dynamics model that assumes all coagulation to take place between spherical particles in the free molecular regime was also investigated. Calculations including the PAH analogy for the surface chemistry and modelling nucleation via $k_{N,1}$ (from previous work) showed no sensitivity compared to the full particle dynamics model. However, a moderate sensitivity was noted following such a simplification in the absence of the surface chemistry model with the ISA assumption and the updated (reduced) rate $k_{N,6}$.
- A summary of the recommended model assumptions and parameters is shown in Table 5.7, with the corresponding reaction rates stated in Section 5.3.

Table 5.7: Recommended sets of models and parameters for the two-equation model.

Case	Growth	Surface chemistry	α_s	Oxidation	$k_{N,i}$	$k_{G,j}$	$k_{OH,k}, k_{O,k}, k_{O_2,k}$
2b	DSA	Yes	0.85	DSA	$k_{N,3}$	$k_{G,2}$	$k_{i,2}$
1b	DSA	No	-	DSA	$k_{N,3}$	$k_{G,1}$	$k_{i,2}$
8b	PSSA	No	-	DSA	$k_{N,7}$	$k_{G,5}$	$k_{i,2}$

6. Soot Particle Size Distributions in the Sandia Flame

6.1. Introduction

In this chapter, calculation results for the Sandia turbulent ethylene diffusion flame [25, 26, 123], obtained using the sectional approach introduced in Chapter 3 in the context of the WSR/PFR reactor of Manzello et al. [17], are presented. In addition to soot volume fraction predictions, as presented for this flame in Chapter 5, the discretised particle size distribution function (PSD) is directly available from the sectional model calculations, and results are discussed in this chapter.

The sectional soot model, with the same parameters ($N_{bin} = 61$) presented in Chapter 3, was implemented in the context of the joint scalar transported PDF approach, as used for the turbulent flame calculations in Chapters 4 and 5. Soot nucleation is modelled based on the acetylene concentration via Eqs. (2.33) and (2.34) with the updated nucleation rate $k_{N,3}$. Both the original set of oxidation rates $k_O, k_{OH,1}, k_{O_2,1}$ by Lindstedt and Louloudi [30] as well as the updated set $k_O, k_{OH,2}, k_{O_2,2}$ are evaluated. All reaction rate constants used in this chapter are summarised in Table 6.1. Growth is modelled using the PAH analogy to soot sur-

Table 6.1: Reaction rate constants for soot growth and oxidation in Eqs. (2.35) and (2.59)-(2.61) presented in the form $A_i \alpha_i T^{\beta_i} \exp(-E_i/RT)$ [27, 28, 96]. Units are in K, kmol, m³ and s.

k_i	A_i	α_i	β_i	E_i/R
$k_{N,3}$	6.30×10^1	1	0	21,000
$k_{G,2}$	3.57×10^{21}	1	-3.176	7,471
k_O	9.09	0.2	1/2	0
$k_{OH,1}$	8.82	0.05	1/2	0
$k_{O_2,1}$	6.43	0.723	1/2	11,250
$k_{OH,2}$	8.82	0.10	1/2	0
$k_{O_2,2}$	6.43	116	1/2	19,680
$k_{O_2,PAH}$	2.15×10^{10}	1	0	3,076

face growth by Lindstedt and Louloudi [30] via Eq. (2.57), where the soot surface area A_s is calculated for each section. The model for the flow field and the gas phase chemistry corresponds to that in Chapter 5, with a radial discretisation of the domain into 465 control volume found sufficient in the context of the sectional model.

6.2. Results and Discussion

In Fig. 6.1, calculation results obtained with the sectional soot model, outlined in Chapter 2, for the Sandia flame are presented. Favre mean and RMS at the centre-line of the flame are shown. For these calculations, incipient soot particles were assigned the mass and diameter of pyrene, and nucleation was modelled via Eq. (2.33), with a scaling of the rate ensuring consistency of the nucleation in terms of particle number density with calculations using the same rate in the two-equation and method of moments calculations in Chapters 4 and 5, as discussed in Section 2.3. The value $C_a = 3.0$ for the van der Waals enhancement factor is used [13], and peak soot is approximately matched for a value of the surface reactivity $\alpha_s = 0.35$, with the nucleation rate $k_{N,3}$ as discussed in Chapters 3–5. The value compares to $\alpha_s = 0.50$, used for two-equation and method of moments calculations of the Delft flame (Chapter 4), and 0.85, used for the Sandia flame with the same methods (Chapter 5). Both values were found in the context of the assumption of soot growth being proportional to the soot surface area (DSA), which is equivalent to the approach in the sectional model calculations. The results presented in Fig. 6.1a were obtained by modelling soot oxidation via the original set of rates $k_O, k_{OH,1}, k_{O_2,1}$ by Lindstedt and Louloudi [28, 30]. The location of peak soot is matched within $10 d$, with the mean soot volume profile generally agreeing with the measurements, although the profile of the latter is somewhat less steep on both sides of the peak. Considering the measurements, the calculated values of the RMS are low compared to the mean as also observed for the two-equation model calculations discussed in Chapter 5, although the qualitative agreement is arguably reasonable. Calculations using the updated set of oxidation rates $k_O, k_{OH,2}, k_{O_2,2}$ are presented in Fig. 6.1b. Results are very similar as those obtained for the original set of rates, with the soot peak shifted downstream by approximately $15 d$ and slightly improved agreement with the experimental data. The same observation with regards to the influence of the oxidation rate on soot volume fraction mean and RMS is made for the calculations using different parameter sets presented in

this chapter, although only results obtained using $k_O, k_{OH,2}, k_{O_2,2}$ will be shown.

In Fig. 6.2, radial profiles of Favre mean and RMS of soot volume fraction obtained of the calculation shown in Fig. 6.1b are presented. Qualitative agreement of the mean profiles with the experimental data is good, with the location of the radial maximum generally well-matched. The measured soot volume fraction at the peak and in the centre of the jet is well-matched by the calculations at $x/d = 23$, but is underpredicted for $55 \leq x/d \leq 86$. Downstream from $x/d = 117$, approaching the peak location, to $x/d = 211$, the agreement with experiment is arguably excellent, with a moderate tendency to underpredicted soot volume fraction in the jet flanks present for $117 \leq x/d \leq 180$. Soot oxidation at the tip of the flame appears underpredicted, with increased levels predicted at $x/d = 242$. The calculated values of RMS of soot volume fraction approximately match the experimental data in the outer jet flanks for $55 \leq x/d \leq 117$, but are too low in the centre of the flame and the main reaction zone. For $148 \leq x/d \leq 211$, the RMS is underpredicted throughout. Further downstream the discrepancy with the experimental data reduces along with the elevated values of the mean.

Apart from the increased levels of soot at the tip of the flame, the agreement with experiment shown here is considerably improved both qualitatively and quantitatively compared to that of the two-equation model calculations presented in Chapter 5, with mean predictions far upstream at $x/d = 23$ as well as mean and RMS

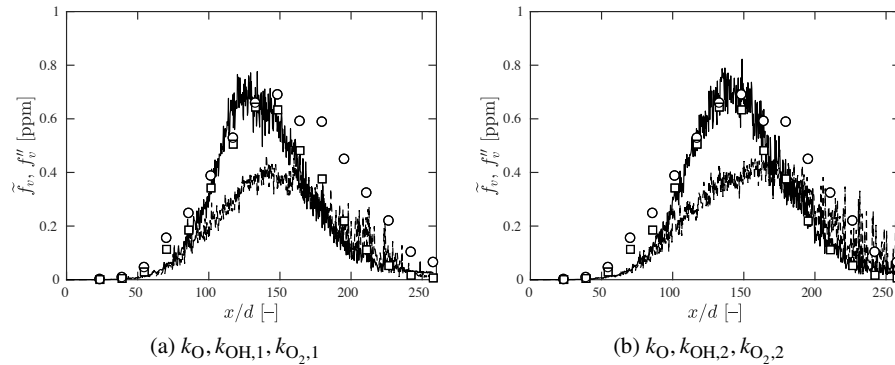
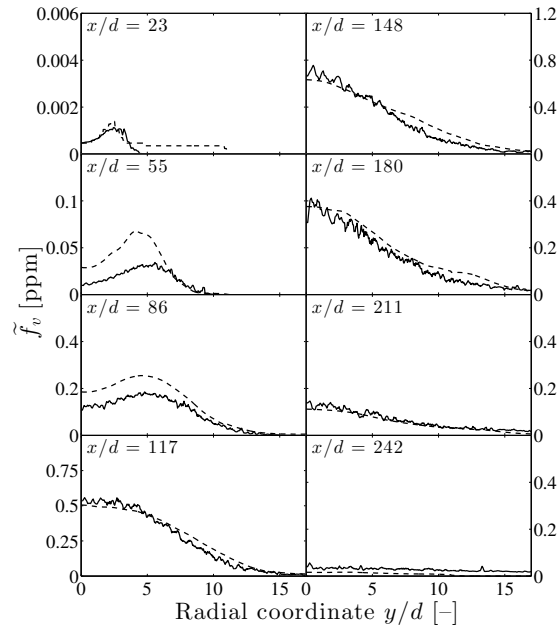
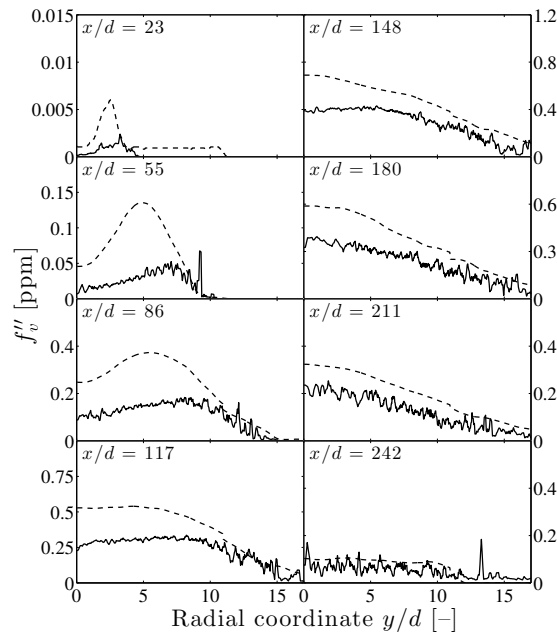


Figure 6.1: Predictions of Favre mean (—) and RMS (---) of soot volume fraction from the sectional model at the centre-line of the Sandia flame using different sets of oxidation rates. Incipient soot particles are assigned the properties of pyrene, $C_a = 3.0$ and $\alpha_s = 0.35$. Comparison to measured mean (\square) and RMS (\circ) from [141].



(a)



(b)

Figure 6.2: Radial profiles of predictions (—) of (a) Favre mean and (b) RMS of soot volume fraction from the sectional model in the Sandia flame. Calculated data is smoothed via a centred moving average filter with window size $0.2 d$. Incipient soot particles are assigned the properties of pyrene, $C_a = 3.0$, $\alpha_s = 0.35$ and $k_{O}, k_{OH,2}, k_{O_2,2}$ are used. Comparison to experimental data (---) from [141].

predictions along most of the length of the flame (from $x/d = 117$ to 242) particularly improved. It may also be noted that the increase in \tilde{f}_v by around a factor of 400 from $x/d = 23$ to $x/d = 148$ is well reproduced. Due to the inherent uncertainty associated with using a constant value for the parameter α_s , the evolution of agreement across the flame is of particular importance, and considerably improved in the sectional model calculations.

The use of $\alpha_s = 0.35$ in conjunction with the updated nucleation and oxidation rates $k_{N,3}, k_{OH,2}, k_{O_2,2}$ is in approximate agreement with the results obtained for the Delft flame presented in Chapter 4, where peak soot was moderately overpredicted for the same set of reaction rates and $\alpha_s = 0.50$. However, the value is lower than the $\alpha_s = 0.85$ required for good agreement using the two-equation model with the surface chemistry and the same set of parameters, as discussed in Chapter 5. The discrepancy is not surprising given that the two-equation model does not provide the PSD of soot, but rather a single representative size of soot particles. The sensitivity to the parameter in the context of the sectional model is presented in Fig. 6.3, where calculations for values of $\alpha_s = 0.25$ and 0.50 are shown, and the same set of parameters as for Fig. 6.1b was used otherwise. Predictions of the mean are underpredicted for $\alpha_s = 0.25$ and increased for $\alpha_s = 0.50$, by a factor of approximately 2.5 in each case. The ratio of the calculated mean to the RMS is much reduced in the former case, matching the experimental observations more closely in this respect.

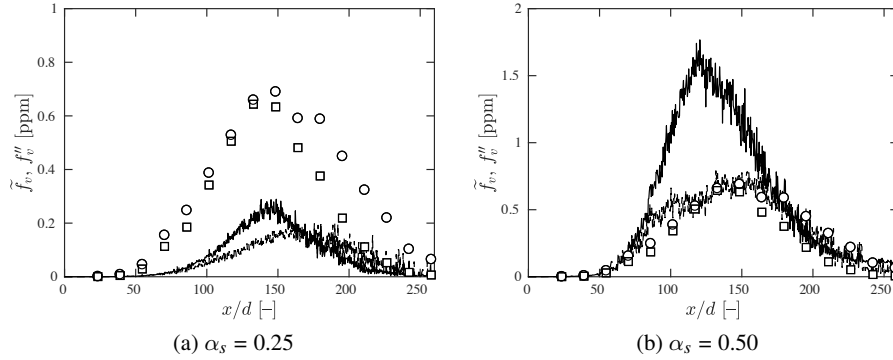


Figure 6.3: Soot predictions from the sectional model at the centre-line of the Sandia flame for different values of the surface reactivity parameter α_s . Incipient soot particles are assigned the properties of pyrene, $C_a = 3.0$ and $k_O, k_{OH,2}, k_{O_2,2}$ are used. Lines and symbols as in Fig. 6.1.

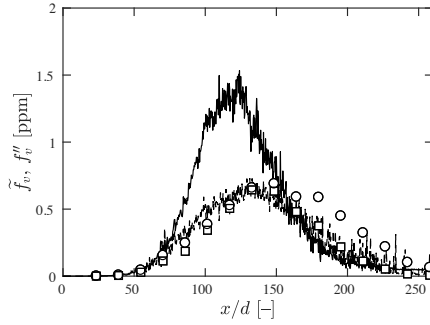


Figure 6.4: Soot predictions from the sectional model at the centre-line of the Sandia flame using a functional dependence of α_s on mixture fraction. Incipient soot particles are assigned the properties of pyrene, $C_a = 3.0$ and $k_O, k_{OH,2}, k_{O_2,2}$ are used. Lines and symbols as in Fig. 6.1.

The functional dependence of α_s on mixture fraction based on the fit by Kazakov et al. [81] and laminar diffusion flame calculations presented in Chapter 5 is evaluated in the current context, and results are shown in Fig. 6.4. The computed profiles are very similar as for the calculations with a constant value of $\alpha_s = 0.50$ shown in Fig. 6.3b.

A number of different choices regarding model assumptions and parameters is naturally possible. Calculations modelling nucleation via Eq. (2.34), as the formation of incipient particles with the properties of naphthalene, are presented in Fig. 6.5. The change from pyrene to naphthalene as the nucleating species changes the mass and diameter of the first section, the thermodynamic properties of all sec-

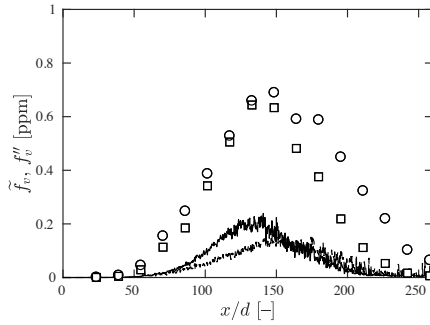


Figure 6.5: Soot predictions from the sectional model at the centre-line of the Sandia flame. Incipient soot particles are assigned the properties of naphthalene. $C_a = 3.0$, $\alpha_s = 0.35$ and $k_O, k_{OH,2}, k_{O_2,2}$ are used. Lines and symbols as in Fig. 6.1.

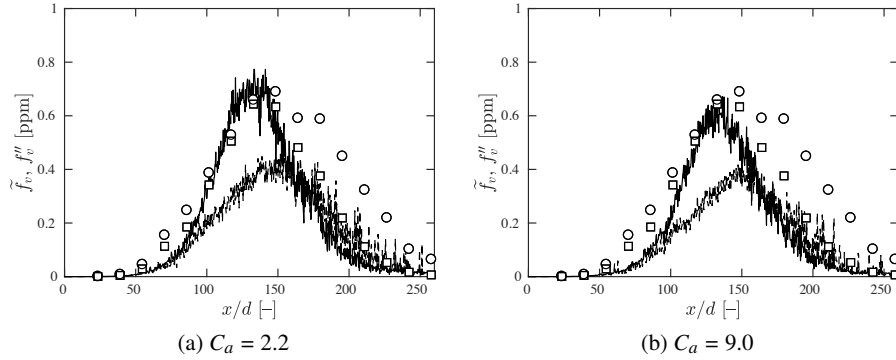


Figure 6.6: Soot predictions from the sectional model at the centre-line of the Sandia flame for different values of the van der Waals enhancement factor C_a . Incipient soot particles are assigned the properties of pyrene, $\alpha_s = 0.35$ and $k_O, k_{OH,2}, k_{O_2,2}$ are used. Lines and symbols as in Fig. 6.1.

tions, and will also affect the gas phase via Eq. (2.34). Compared to the case shown in Fig. 6.1b, the mean soot volume fraction is reduced significantly by a factor of approximately 3.5 in the results shown here. The value of the RMS also decreases, and the agreement with experiment regarding its magnitude relative to the mean is improved. A range of values for the van der Waals enhancement factor C_a have been used in previous work [13, 15, 48], and the sensitivity of the current model is shown in Fig. 6.6. Compared to the reference case (Fig. 6.1b), which uses $C_a = 3.0$, agreement is similar for $C_a = 2.2$ [65], with a steeper profile in the oxidation zone downstream from the peak, and the soot volume fraction is moderately decreased throughout the flame and approximately by 15 % at the peak for $C_a = 9.0$ [30], as shown in Fig. 6.6a and 6.6b, respectively.

In the computations presented in Fig. 6.7, additional soot oxidation via an analogy to the PAH soot surface growth term by Lindstedt and Louloudi [30], as introduced by Lindstedt and Waldheim [13] and shown in Eq. (2.63) is considered. In comparison to the reference case shown in Fig. 6.1b, peak soot is moderately reduced, and soot is oxidized noticeably faster downstream from the peak, which reduces the agreement with the measurements.

The sectional soot model calculations inherently grant access to information about particle size distributions. In Figs. 6.8–6.12, PSDs obtained from the model using the recommended updated nucleation and oxidation rates, $C_a = 3.0$ and $\alpha_s = 0.35$, with nucleation occurring via formation of pyrene from acetylene (cor-

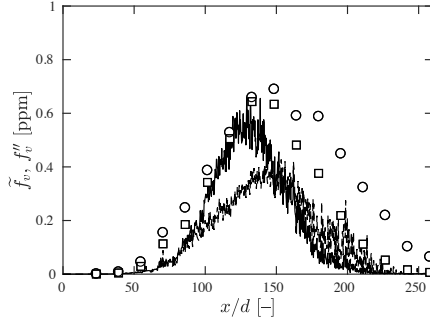


Figure 6.7: Soot predictions from the sectional model at the centre-line of the Sandia flame. Additional O_2 oxidation via the surface chemistry based expression by Lindstedt and Waldheim [13] was introduced. Incipient soot particles are assigned the properties of pyrene, $C_a = 3.0$, $\alpha_s = 0.35$ and $k_O, k_{OH,2}, k_{O_2,2}$ are used. Lines and symbols as in Fig. 6.1.

responding to the case shown in Fig. 6.1b) are shown. As no experimental data set on soot particle sizes exists for this flame, the calculated PSDs are presented for demonstration purposes only, allowing a limited assessment of the predictions. At the centre-line (Fig. 6.8), the PSD is initially unimodal at $x/d \leq 40$. The development of a moderately bimodal distribution is observed for $x/d \geq 80$, with the maximum in the distribution occurring at a particle size of approximately 30 nm for $x/d \geq 120$, and another peak being located at the smallest bin, into which particles formed by the nucleation reaction are inserted. A discontinuity of the PSD is present at a diameter of $d_p \approx 27.5$ nm. The location coincides with the switch from coagulation into spherical particles to aggregation into fractal structures at this particle diameter, resulting in a step-change of the calculated coagulation rates and the particle surface area, the latter affecting surface growth and oxidation rates. While under the conditions in the WSR/PFR configuration discussed in Chapter 3, the switch results merely in a change of the slope of the PSD, in qualitative agreement with the experimental data, the notable discontinuity of the distribution that develops particularly under oxidative conditions in the Sandia flame (e.g. for $x/d \geq 120$ at the centre-line) appears unphysical, and may indicate that a refinement of the model for the onset of agglomeration is required. At the limits of the regions where soot is present, i.e. at the tip of the flame ($x/d \geq 200$) and in the jet flanks (e.g., at $x/d = 100, y/d \geq 12$), oxidation is dominant, and the particle concentration in the bin for the largest particles is observed to decrease slower than in the penultimate bin. The effect stems from the boundary treatment in the context of

the 'two-point' method (see Section 2.7), leading to reduced growth and oxidation rates in the final bin. Some truncation of the PSD is inevitable, and the total number of bins was chosen here to ensure that particle concentrations at the upper end of the PSD are several orders of magnitude lower than at the peak, eliminating any significant influence on the main region of interest at smaller particle sizes.

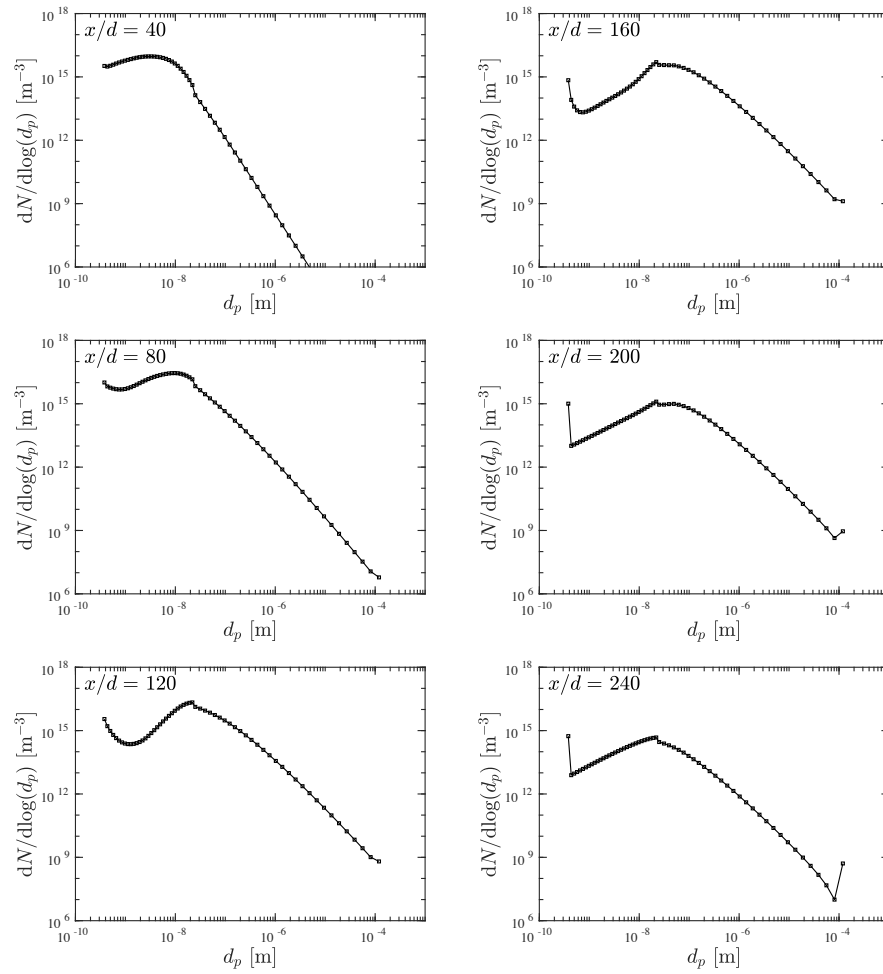


Figure 6.8: Calculated particle size distributions at the centre-line of the Sandia flame.

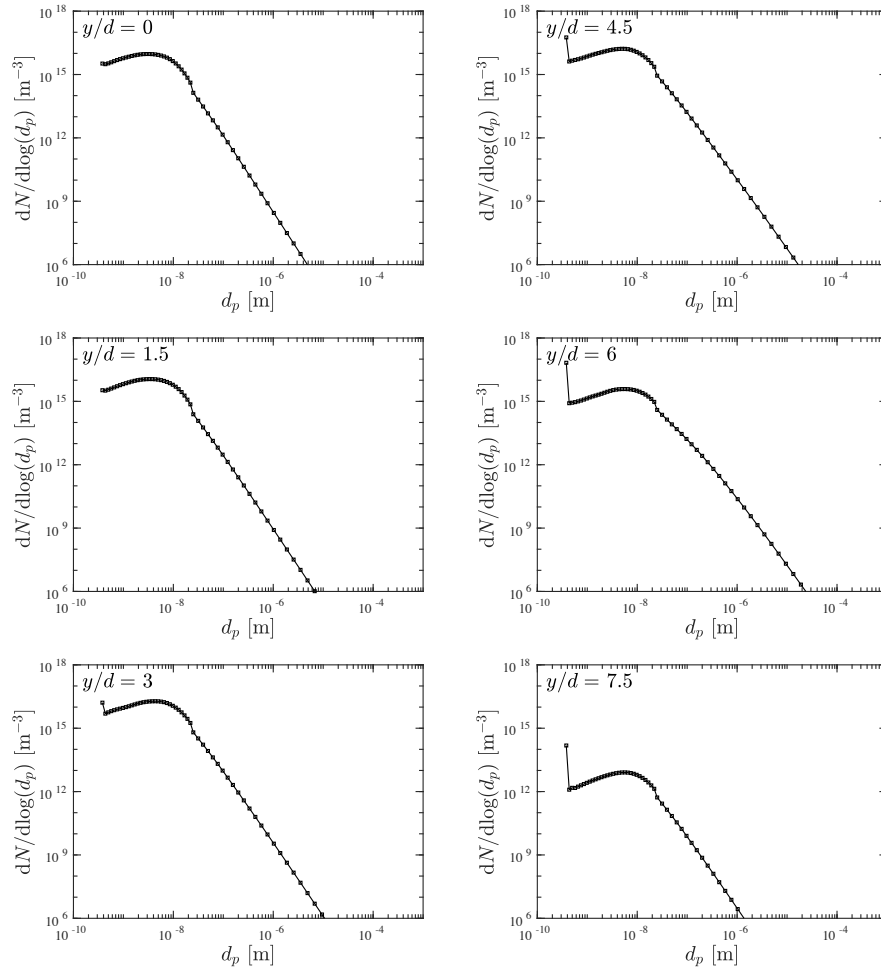


Figure 6.9: Calculated particle size distributions at different radial positions and axial position $x/d = 40$ of the Sandia flame.

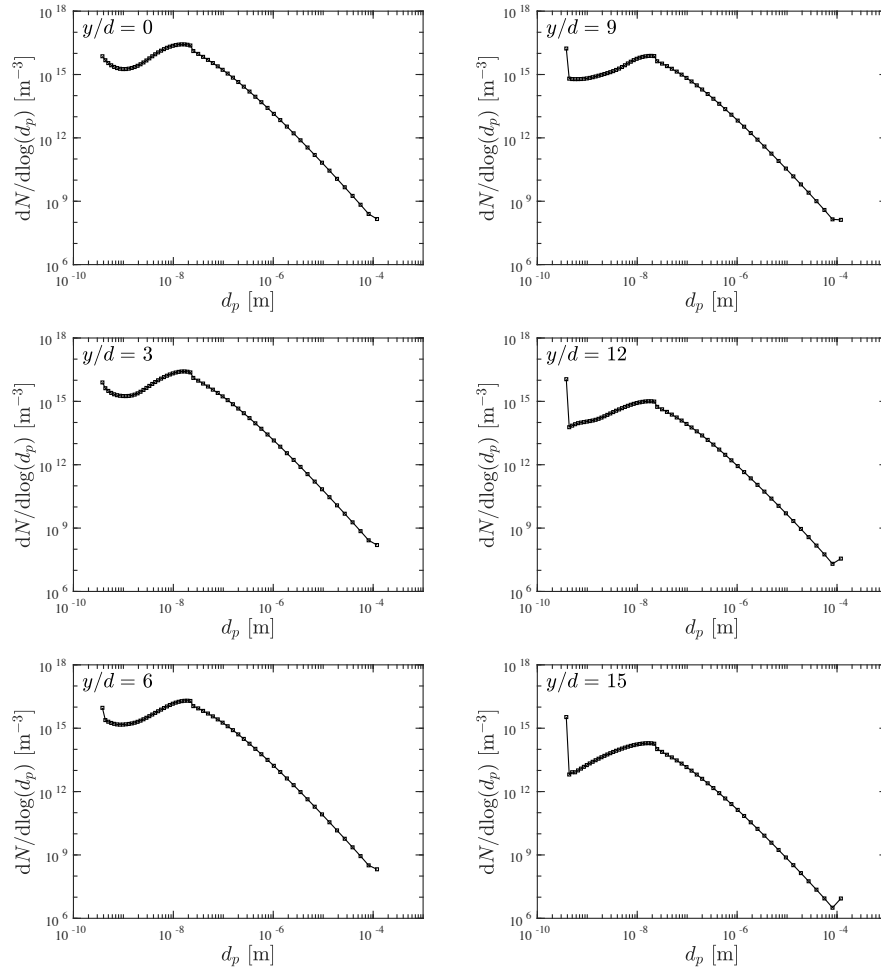


Figure 6.10: Calculated particle size distributions at different radial positions and axial position $x/d = 100$ of the Sandia flame.

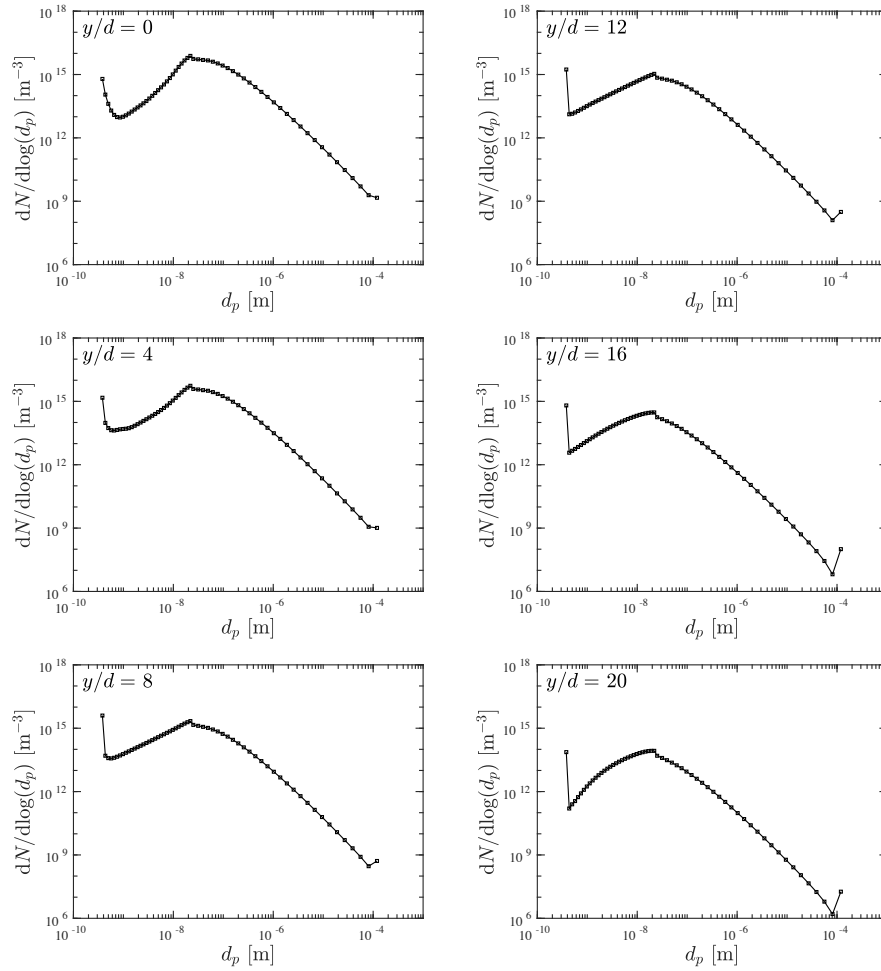


Figure 6.11: Calculated particle size distributions at different radial positions and axial position $x/d = 150$ of the Sandia flame.

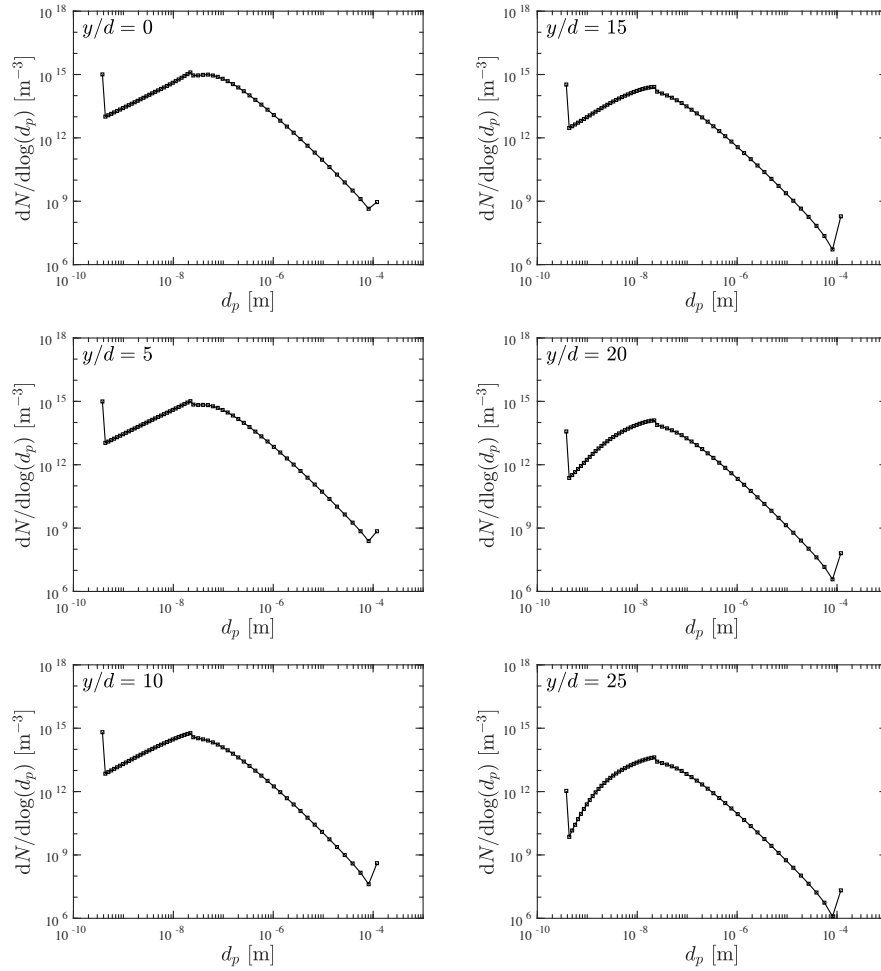


Figure 6.12: Calculated particle size distributions at different radial positions and axial position $x/d = 200$ of the Sandia flame.

6.3. Conclusions

Calculations of soot volume fraction statistics and PSDs in the Sandia turbulent ethylene diffusion flame obtained using a sectional soot model were presented. The following conclusions are drawn:

- The agreement of the mean soot volume fraction with experimental data is encouraging, and a considerable improvement over results computed using a two-equation type soot model in Chapter 5, while the same tendency to underpredict the RMS of soot is observed.
- Consistent with the results presented in Chapters 3 to 5, good agreement could be obtained with of the updated rate $k_{N,3}$ for acetylene based nucleation models.
- The sensitivity of the soot model to a range of different parameters has been explored, and the recommended set of parameters comprises the updated set of oxidation rates $k_O, k_{OH,2}, k_{O_2,2}$, $C_a = 3.0$, the use of pyrene properties for the mass and size of incipient soot particles as well as for the thermodynamical data of soot sections, and a constant value of the surface reactivity parameter $\alpha_s = 0.35$.
- A mixture fraction based functional form for α_s introduced in Chapter 5 has been applied in the current context, and result similar to those obtained for a constant value $\alpha_s = 0.50$ were obtained, with peak soot levels at the centre-line overpredicted by a factor of 2.5.
- In the absence of experimentally measured particle size data, the calculated PSDs can only be evaluated tentatively. Results appear reasonable, and the comparison of predictions from the current model in turbulent flames to measured PSDs would constitute the next logical step for model validation.

7. Conclusions and Future Work

7.1. Conclusions

The present work has analysed the modelling of soot in three different reactor systems and flames, spanning a combined well-stirred/plug flow reactor for premixed conditions and two non-premixed turbulent jet flames burning natural gas and ethylene. The choice of laboratory-scale configurations allows the development of modelling capabilities in well-defined setups for which experimental data bases exist in the literature that may be further extended in the future. The joint scalar transported PDF approach adopted treats turbulence-chemistry interactions without approximation and eliminates any uncertainty that may stem from a model. Accordingly, it permits a focus on the performance of the soot model within the framework of the selected gas phase chemistry models.

Calculations via a detailed sectional soot model were carried out for the premixed WSR/PFR setup to assess the influence of model assumptions on soot particle size predictions as compared with experimental data:

- It was found that the nucleation rate adopted in the context of turbulent flames in previous work [27, 28, 30] appears too high under premixed conditions, and a reduced, updated nucleation rate was proposed.
- An update to the soot oxidation rates used in previous work [15, 142] was also introduced, and found to affect PSD predictions only marginally.
- The sensitivity to model parameters was explored, and it is recognized that uncertainties, particularly regarding the surface reactivity parameter α_s , may affect results considerably.
- However, for a choice of parameters in line with previous work [13, 15], the proposed reduced nucleation rates improve the agreement of PSD predictions with measurements.

Two-equation and method of moments calculations were performed for the two turbulent diffusion flames considered, using ethylene and a methane-based fuel:

- The updates to soot nucleation and oxidation rates previously evaluated on the WSR/PFR setup were implemented into these turbulent calculations, and found to yield encouraging results.
- The agreement of soot predictions in the Delft III / Adelaide non-premixed turbulent natural gas flame compares favourably to previous LES studies using a flamelet/progress variable approach with a nucleation model based on PAH dimerisation [114, 115], despite the considerably simpler treatment of the fluid mechanics in the current work.
- In the context of the Sandia non-premixed turbulent ethylene flame, a range of different assumptions regarding the surface-area dependence of soot growth and oxidation from previous work [23, 27, 28] have been re-considered. It was found that the more conventional assumption of proportionality to the surface area in conjunction with a growth model considering reactions on the soot surface via a steady-state assumption yields the best agreement with experiment.
- Propositions of parameter sets for growth proportional to the soot surface area or its square-root with a single acetylene-based growth step were made, should a computationally less expensive growth model be preferred. The former includes the reduced nucleation rate derived in the WSR/PFR setup, while the rate for the latter was determined empirically.

The sectional soot model was integrated with the joint scalar transported PDF approach, and soot volume fraction statistics and PSDs in the Sandia flame were computed with the model.

- Calculations using the updated nucleation and oxidation rates resulted in considerably improved agreement of soot volume fraction with experimental data.
- Soot PSDs obtained with the model are available, but could not be quantitatively analysed due to lack of measured PSDs in this flame and in turbulent flames generally.

The main contributions of the current work can be summed up as following:

- The work represents a steps towards a more unified model across flame conditions and fuels. Reasonable agreement of calculations with experiment could be obtained for a relatively small range of nucleation rates across premixed and non-premixed configurations and ethylene and methane-based fuels. Furthermore, for a constant value of the parameter α_s describing the fraction of available reaction sites on the soot surface, the uncertainty across the three

different experimental setups considered in the present work was reduced to $0.35 \leq \alpha_s \leq 0.85$.

- By further validating and empirically optimising the two-equation soot model with acetylene-based nucleation, this work contributes to providing options to modellers, particularly where economical considerations take precedence.
- The accurate treatment of turbulence-chemistry interactions via the use of a transported PDF approach is favoured over elaborate flow-field models (e.g. via LES) in this work, and the relatively good agreement of soot predictions with experiment that could be obtained hence highlights the importance of the former.
- The current work is among the first to present calculations of soot PSDs in turbulent flames via a sectional model, with comparable work only having started to appear very recently [143, 144]. It thus represents a contribution to the development of modelling capabilities, ensuring evolving emission standards be met.

7.2. Future Work

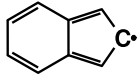
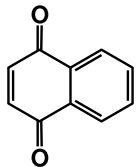
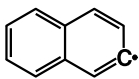
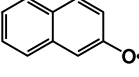
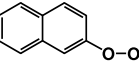
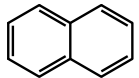
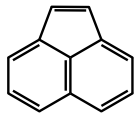
- In the future, an extension of the validation for the reduced nucleation rates proposed in this work is required, and can be achieved by including further reactor cases and laminar flames. The inclusion of both premixed and non-premixed systems would be desirable to improve generality. Lindstedt and Waldheim [13] calculated soot PSDs in the premixed stagnation flow flames by Abid et al. [52–54] using the sectional model with the pyrene-based nucleation discussed in this work, and the inclusion of an acetylene-based nucleation model into these calculations would constitute a suitable starting point.
- The surface reactivity parameter α_s is a source of uncertainty, and the development of flame-independent functional forms is important. The integration of, for example, thermal age dependant functional forms [137, 138] into the current models and turbulent flame calculations may offer a way to improve the applicability of the models across systems.
- Further analysis of the calculated PSDs in the Sandia flame is necessary and the comparison to experimental data for soot PSDs in turbulent flows is required for validation. Boyette et al. [145] and Chowdhury et al. [146] recently presented measurement of soot particle size distributions obtained on two turbulent

C_2H_4/N_2 flames at $Re = 10,000$ and $20,000$, based on the same burner used for the Sandia flame, and the current model can be applied in this context.

- While the work presented in this thesis concerns itself with systems at atmospheric pressure, applications such as jet engine combustors or diesel engines operate at (often highly) elevated pressures. The validation of the soot models under pressurised conditions is required to bridge this gap. The calculation of pressurised laminar sooting flames [111] using the current acetylene-based nucleation model could serve as a first step to this end.
- Further, the pairing of the current soot models with an elliptic flow solver or their integration into an LES approach would allow the application to more complex configurations such as pressurised swirl flames [111, 147], approaching industrial applications.
- Ultimately, the application of the soot (sub-)models discussed in this work to commercial systems such as aeronautical combustors or internal combustion engines must be the aim, and as such practical fuels such as kerosene must be considered. This makes the procurement of experimental data across increasingly complex flow fields essential.

A. Structures of Species

Table A.1: The structures of the aromatic species in the PAH analogy model for soot surface growth by Lindstedt and Louloudi [28, 30].

Acronym	Structure
C_9H_7	
$C_{10}H_6O_2$	
$C_{10}H_7$	
$C_{10}H_7O$	
$C_{10}H_7OO$	
$C_{10}H_8$	
$C_{12}H_8$	

Bibliography

- [1] United States Environmental Protection Agency, Health and Environmental Effects of Particulate Matter (PM), <https://www.epa.gov/pm-pollution/health-and-environmental-effects-particulate-matter-pm>.
- [2] K. Donaldson, D. Brown, A. Clouter, R. Duffin, W. MacNee, L. Renwick, L. Tran, V. Stone, The Pulmonary Toxicology of Ultrafine Particles, *Journal of Aerosol Medicine*, 15(2), (2002), pp. 213–220.
- [3] R. D. Brook, S. Rajagopalan, C. A. Pope, J. R. Brook, A. Bhatnagar, A. V. Diez-Roux, F. Holguin, Y. Hong, R. V. Luepker, M. A. Mittleman, A. Peters, D. Siscovick, S. C. Smith, L. Whitsel, J. D. Kaufman, Particulate matter air pollution and cardiovascular disease: An update to the scientific statement from the american heart association, *Circulation*, 121(21), (2010), pp. 2331–2378.
- [4] G. B. Hamra, N. Guha, A. Cohen, F. Laden, O. Raaschou-Nielsen, J. M. Samet, P. Vineis, F. Forastiere, P. Saldiva, T. Yorifuji, D. Loomis, Outdoor particulate matter exposure and lung cancer: A systematic review and meta-analysis, *Environmental Health Perspectives*, 122(9), (2014), pp. 906–911.
- [5] K. Donaldson, L. Tran, L. A. Jimenez, R. Duffin, D. E. Newby, N. Mills, W. MacNee, V. Stone, Combustion-derived nanoparticles: a review of their toxicology following inhalation exposure., *Particle and fibre toxicology*, 2(10), (2005), pp. 1–14.
- [6] European Commission, Air Quality Standards, <http://ec.europa.eu/environment/air/quality/standards.htm>.
- [7] J. Fan, Y. Wang, D. Rosenfeld, X. Liu, Review of Aerosol–Cloud Interactions: Mechanisms, Significance, and Challenges, *Journal of the Atmospheric Sciences*, 73(11), (2016), pp. 4221–4252.

- [8] International Civil Aviation Organization, ICAO Environmental Report 2016.
- [9] European Commission, Emissions in the Automotive Sector, https://ec.europa.eu/growth/sectors/automotive/environment-protection/emissions_en.
- [10] DieselNet, Emission Standards, European Union, <https://www.dieselnets.com/standards/eu/index.php>.
- [11] United States Environmental Protection Agency, Regulations for Emissions from Vehicles and Engines, <https://www.epa.gov/regulations-emissions-vehicles-and-engines/regulations-onroad-vehicles-and-engines>.
- [12] TransportPolicy.net, Regions: United States, <https://www.transportpolicy.net/region/north-america/united-states>.
- [13] R. P. Lindstedt, B. B. O. Waldheim, Modeling of soot particle size distributions in premixed stagnation flow flames, *Proceedings of the Combustion Institute*, 34(1), (2013), pp. 1861–1868.
- [14] B. B. O. Waldheim, Modelling of soot formation and aromatic growth in laminar flames and reactor systems, Ph.D. thesis, Imperial College London, 2015.
- [15] J. S. Bhatt, R. P. Lindstedt, Analysis of the impact of agglomeration and surface chemistry models on soot formation and oxidation, *Proceedings of the Combustion Institute*, 32(1), (2009), pp. 713–720.
- [16] S. Kumar, D. Ramkrishna, On the solution of population balance equations by discretization–I. A fixed pivot technique, *Chemical Engineering Science*, 51(8), (1996), pp. 1311–1332.
- [17] S. L. Manzello, D. B. Lenhert, A. Yozgatligil, M. T. Donovan, G. W. Mulholland, M. R. Zachariah, W. Tsang, Soot particle size distributions in a well-stirred reactor/plug flow reactor, *Proceedings of the Combustion Institute*, 31, (2007), pp. 675–683.
- [18] D. B. Lenhert, S. L. Manzello, Effects of benzene and naphthalene addition on soot inception in a well-stirred reactor/plug flow reactor, *Proceedings of the Combustion Institute*, 32(1), (2009), pp. 657–664.

- [19] S. B. Pope, PDF methods for turbulent reactive flows, *Progress in Energy and Combustion Science*, 11(2), (1985), pp. 119–192.
- [20] T. W. J. Peeters, P. P. J. Stroomer, J. E. de Vries, D. J. E. M. Roekaerts, C. J. Hoogendoorn, Comparative experimental and numerical investigation of a piloted turbulent natural-gas diffusion flame, *Proceedings of the Combustion Institute*, 25(1), (1994), pp. 1241–1248.
- [21] P. A. Nooren, Stochastic modeling of turbulent natural-gas flames, Ph.D. thesis, Technische Universiteit Delft, 1998.
- [22] P. A. Nooren, M. Versluis, T. H. van der Meer, R. S. Barlow, J. H. Frank, Raman-Rayleigh-LIF measurements of temperature and species concentrations in the Delft piloted turbulent jet diffusion flame, *Applied Physics B: Lasers and Optics*, 71(1), (2000), pp. 95–111.
- [23] K. M. Leung, R. P. Lindstedt, W. P. Jones, A simplified reaction mechanism for soot formation in nonpremixed flames, *Combustion and Flame*, 87(3-4), (1991), pp. 289–305.
- [24] M. Frenklach, Method of moments with interpolative closure, *Chemical Engineering Science*, 57(12), (2002), pp. 2229–2239.
- [25] C. R. Shaddix, J. Zhang, R. W. Schefer, J. Doom, J. C. Oefelein, S. Kook, L. M. Pickett, H. Wang, Understanding and predicting soot generation in turbulent non-premixed jet flames, Tech. rep., Sandia Report SAND2010-7178, 2010.
- [26] J. Zhang, C. R. Shaddix, R. W. Schefer, Design of model-friendly turbulent non-premixed jet burners for C_{2+} hydrocarbon fuels, *Review of Scientific Instruments*, 82(7), (2011), pp. 1–10.
- [27] R. P. Lindstedt, Simplified Soot Nucleation and Surface Growth Steps for non-Premixed Flames, in: H. Bockhorn, ed., *Soot Formation in Combustion: Mechanisms and Models*, 59, Springer-Verlag, 1994, pp. 417–441.
- [28] S. A. Louloudi, Transported probability density function modeling of turbulent jet flames, Ph.D. thesis, Imperial College London, 2003.
- [29] D. B. Spalding, *GENMIX – A General Computer Program for Two-Dimensional Parabolic Phenomena*, Pergamon Press, Oxford, 1977.

- [30] R. P. Lindstedt, S. A. Louloudi, Joint-scalar transported PDF modeling of soot formation and oxidation, *Proceedings of the Combustion Institute*, 30(1), (2005), pp. 775–782.
- [31] S. H. Park, S. N. Rogak, A novel fixed-sectional model for the formation and growth of aerosol agglomerates, *Journal of Aerosol Science*, 35(11), (2004), pp. 1385–1404.
- [32] J. H. Kent, D. Honnery, Soot and Mixture Fraction in Turbulent Diffusion Flames, *Combustion Science and Technology*, 54, (1987), pp. 383–398.
- [33] A. Coppalle, D. Joyeux, Temperature and Soot Volume Fraction in Turbulent Diffusion Flames: Measurements of Mean and Fluctuating Values, *Combustion and Flame*, 96(3), (1994), pp. 275–285.
- [34] W. L. Grosshandler, RADCAL: A Narrow-Band Model for Radiation Calculations in a Combustion Environment., Tech. rep., NIST Technical Note 1402, 1993.
- [35] R. J. Hall, Computation of the radiative power loss in a sooting diffusion flame, *Applied Optics*, 27(5), (1988), pp. 809–811.
- [36] C. G. Speziale, S. Sarkar, T. B. Gatski, Modelling the pressure-strain correlation of turbulence: an invariant dynamical systems approach, *Journal of Fluid Mechanics*, 227, (1991), pp. 245–272.
- [37] B. J. Daly, F. H. Harlow, Transport Equations in Turbulence, *Physics of Fluids*, 13(11), (1970), pp. 2634–2649.
- [38] J. Janicka, W. Kolbe, W. Kollmann, Closure of the Transport Equation for the Probability Density Function of Turbulent Scalar Fields, *Journal of Non-Equilibrium Thermodynamics*, 4, (1979), pp. 47–66.
- [39] R. P. Lindstedt, S. A. Louloudi, E. M. Város, Joint scalar probability density function modeling of pollutant formation in piloted turbulent jet diffusion flames with comprehensive chemistry, *Proceedings of the Combustion Institute*, 28(1), (2000), pp. 149–156.
- [40] R. P. Lindstedt, S. A. Louloudi, Joint scalar transported probability density function modeling of turbulent methanol jet diffusion flames, *Proceedings of the Combustion Institute*, 29(2), (2002), pp. 2147–2154.

- [41] T. S. Kuan, R. P. Lindstedt, E. M. Váos, Higher Moment Based Modeling of Turbulence Enhanced Explosion Kernels in Confined Fuel-Air Mixtures, in: G. Roy, ed., *Advances in Confined Detonations and Pulse Detonation Engines*, Torus Press, 2003, ISBN 5-94588-012-4, pp. 17–40.
- [42] R. P. Lindstedt, E. M. Váos, Transported PDF modeling of high-Reynolds-number premixed turbulent flames, *Combustion and Flame*, 145(3), (2006), pp. 495–511.
- [43] R. P. Lindstedt, H. Ozarovsky, R. S. Barlow, A. N. Karpetsis, Progression of localized extinction in high Reynolds number turbulent jet flames, *Proceedings of the Combustion Institute*, 31(1), (2007), pp. 1551–1558.
- [44] K. Gkagkas, R. P. Lindstedt, The impact of reduced chemistry on auto-ignition of H_2 in turbulent flows, *Combustion Theory and Modelling*, 13(4), (2009), pp. 607–643.
- [45] M. von Smoluchowski, Three lectures on diffusion, Brownian movement and coagulation of colloidal particles, *Physikalische Zeitschrift*, 17, (1916), pp. 557–571, 585–599.
- [46] M. Frenklach, S. J. Harris, Aerosol dynamics modeling using the method of moments, *Journal of Colloid And Interface Science*, 118(1), (1987), pp. 252–261.
- [47] M. Frenklach, H. Wang, Detailed Mechanism and Modeling of Soot Particle Formation, in: H. Bockhorn, ed., *Soot Formation in Combustion: Mechanisms and Models*, Springer-Verlag, 1994, pp. 165–192.
- [48] A. Kazakov, M. Frenklach, Dynamic Modeling of Soot Particle Coagulation and Aggregation: Implementation With the Method of Moments and Application to High-Pressure Laminar Premixed Flames, *Combustion and Flame*, 114, (1998), pp. 484–501.
- [49] F. Gelbard, Y. Tambour, J. H. Seinfeld, Sectional representations for simulating aerosol dynamics, *Journal of Colloid and Interface Science*, 76(2), (1980), pp. 541–556.
- [50] T. T. Nguyen, F. Laurent, R. O. Fox, M. Massot, Solution of population balance equations in applications with fine particles: Mathematical modeling

and numerical schemes, *Journal of Computational Physics*, 325, (2016), pp. 129–156.

- [51] M. D. Smooke, M. B. Long, B. C. Connelly, M. B. Colket, R. J. Hall, Soot formation in laminar diffusion flames, *Combustion and Flame*, 143, (2005), pp. 613–628.
- [52] A. D. Abid, N. Heinz, E. D. Tolmachoff, D. J. Phares, C. S. Campbell, H. Wang, On evolution of particle size distribution functions of incipient soot in premixed ethylene–oxygen–argon flames, *Combustion and Flame*, 154, (2008), pp. 775–788.
- [53] A. D. Abid, E. D. Tolmachoff, D. J. Phares, H. Wang, Y. Liu, A. Laskin, Size distribution and morphology of nascent soot in premixed ethylene flames with and without benzene doping, *Proceedings of the Combustion Institute*, 32(1), (2009), pp. 681–688.
- [54] A. D. Abid, J. Camacho, D. A. Sheen, H. Wang, Quantitative measurement of soot particle size distribution in premixed flames – The burner-stabilized stagnation flame approach, *Combustion and Flame*, 156(10), (2009), pp. 1862–1870.
- [55] H. Bockhorn, *Soot Formation in Combustion: Mechanisms and Models*, 1994.
- [56] R. McGraw, Description of Aerosol Dynamics by the Quadrature Method of Moments, *Aerosol Science and Technology*, 27, (1997), pp. 255–265.
- [57] D. L. Marchisio, R. O. Fox, Solution of population balance equations using the direct quadrature method of moments, *Journal of Aerosol Science*, 36, (2005), pp. 43–73.
- [58] M. E. Mueller, G. Blanquart, H. Pitsch, Hybrid Method of Moments for modeling soot formation and growth, *Combustion and Flame*, 156(6), (2009), pp. 1143–1155.
- [59] C. Yuan, R. O. Fox, Conditional quadrature method of moments for kinetic equations, *Journal of Computational Physics*, 230(22), (2011), pp. 8216–8246.

- [60] S. Salenbauch, A. Cuoci, A. Frassoldati, C. Saggese, T. Faravelli, C. Hasse, Modeling soot formation in premixed flames using an Extended Conditional Quadrature Method of Moments, *Combustion and Flame*, 162(6), (2015), pp. 2529–2543.
- [61] M. Fairweather, W. P. Jones, H. S. Ledin, R. P. Lindstedt, Predictions of soot formation in turbulent, non-premixed propane flames, *Proceedings of the Combustion Institute*, 24, (1992), pp. 1067–1074.
- [62] M. Fairweather, W. P. Jones, R. P. Lindstedt, Predictions of radiative transfer from a turbulent reacting jet in a cross-wind, *Combustion and Flame*, 89(1), (1992), pp. 45–63.
- [63] P. P. Popov, S. B. Pope, Large eddy simulation/probability density function simulations of bluff body stabilized flames, *Combustion and Flame*, 161(12), (2014), pp. 3100–3133.
- [64] S. E. Pratsinis, Simultaneous Nucleation, Condensation, and Coagulation in Aerosol Reactors, *Journal of Colloid and Interface Science*, 124(2), (1988), pp. 416–427.
- [65] S. J. Harris, I. M. Kennedy, The Coagulation of Soot Particles with van der Waals Forces, *Combustion Science and Technology*, 59(4-6), (1988), pp. 443–454.
- [66] B. A. Pailthorpe, W. B. Russel, The retarded van der Waals interaction between spheres, *Journal of Colloid and Interface Science*, 89(2), (1982), pp. 563–566.
- [67] Ü. Ö. Köylü, G. M. Faeth, T. L. Farias, M. G. Carvalho, Fractal and Projected Structure Properties of Soot Aggregates, *Combustion and Flame*, 100(4), (1995), pp. 621–633.
- [68] C. M. Sorensen, The mobility of fractal aggregates: A review, *Aerosol Science and Technology*, 45(7), (2011), pp. 755–769.
- [69] C. M. Sorensen, W. Kim, D. Fry, D. Shi, A. Chakrabarti, Observation of soot superaggregates with a fractal dimension of 2.6 in laminar acetylene/air diffusion flames, *Langmuir*, 19(18), (2003), pp. 7560–7563.

- [70] Z. Li, C. Song, J. Song, G. Lv, S. Dong, Z. Zhao, Evolution of the nanostructure, fractal dimension and size of in-cylinder soot during diesel combustion process, *Combustion and Flame*, 158(8), (2011), pp. 1624–1630.
- [71] S. Vemury, S. E. Pratsinis, Self-preserving size distributions of agglomerates, *Journal of Aerosol Science*, 26(4), (1995), p. 1995.
- [72] S. K. Friedlander, *Smoke, Dust, and Haze*, Oxford University Press, New York, 2nd edn., 2000.
- [73] S. Löffler, K. H. Homann, Large Ions in Premixed Benzene-Oxygen Flames, *Proceedings of the Combustion Institute*, 23, (1990), pp. 355–362.
- [74] P. B. Sunderland, Ü. Ö. Köylü, G. M. Faeth, Soot formation in weakly buoyant acetylene-fueled laminar jet diffusion flames burning in air, *Combustion and Flame*, 100(1-2), (1995), pp. 310–322.
- [75] K. Lin, P. B. Sunderland, G. M. Faeth, Soot nucleation and growth in acetylene air laminar coflowing jet diffusion flames.pdf, *Combustion and Flame*, 104, (1996), pp. 369–375.
- [76] P. B. Sunderland, G. M. Faeth, Soot formation in hydrocarbon air laminar jet diffusion flames, *Combustion and Flame*, 105(95), (1996), pp. 132–146.
- [77] S. J. Harris, A. M. Weiner, Determination of the Rate Constant for Soot Surface, *Combustion Science and Technology*, 32, (1983), pp. 267–275.
- [78] J. Appel, H. Bockhorn, M. Frenklach, Kinetic modeling of soot formation with detailed chemistry and physics: laminar premixed flames of C₂ hydrocarbons, *Combustion and Flame*, 121(1-2), (2000), pp. 122–136.
- [79] M. Frenklach, H. Wang, Detailed modelling of soot particle nucleation and growth, *Proceedings of the Combustion Institute*, 23(1), (1990), pp. 1559–1566.
- [80] M. L. Potter, *Detailed Chemical Kinetic Modelling of Propulsion Fuels*, Ph.D. thesis, Imperial College London, 2003.
- [81] A. Kazakov, H. Wang, M. Frenklach, Detailed Modeling of Soot Formation in Laminar Premixed Ethylene Flames at a Pressure of 10 Bar, *Combustion and Flame*, 100(1-2), (1995), pp. 111–120.

- [82] H. Guo, P. M. Anderson, P. B. Sunderland, Optimized rate expressions for soot oxidation by OH and O₂, *Fuel*, 172, (2016), pp. 248–252.
- [83] K. B. Lee, M. W. Thring, J. M. Beér, On the rate of combustion of soot in a laminar soot flame, *Combustion and Flame*, 6, (1962), pp. 137–145.
- [84] C. P. Fenimore, G. W. Jones, Oxidation of soot by hydroxyl radicals, *Journal of Physical Chemistry*, 71(3), (1967), pp. 593–597.
- [85] K. G. Neoh, Soot Burnout in Flames, Ph.D. thesis, Massachusetts Institute of Technology, 1980.
- [86] M.-L. Chan, K. N. Moody, J. R. Mullin, A. Williams, Low-temperature oxidation of soot, *Fuel*, 66, (1987), pp. 1694–1698.
- [87] A. Garo, G. Prado, J. Lahaye, Chemical Aspects of Soot Particles Oxidation in a Laminar Methane-Air Diffusion Flame, *Combustion and Flame*, 79, (1990), pp. 226–233.
- [88] R. Puri, R. J. Santoro, K. C. Smyth, The Oxidation of Soot and Carbon Monoxide in Hydrocarbon Diffusion Flames, *Combustion and Flame*, 97, (1994), pp. 125–144.
- [89] R. Puri, R. J. Santoro, K. C. Smyth, Erratum, *Combustion and Flame*, 102, (1995), pp. 226–228.
- [90] K. J. Higgins, H. Jung, D. B. Kittelson, J. T. Roberts, M. R. Zachariah, Size-selected nanoparticle chemistry: kinetics of soot oxidation, *Journal of Physical Chemistry A*, 106, (2002), pp. 96–103.
- [91] F. Xu, A. M. El-Leathy, C. H. Kim, G. M. Faeth, Soot surface oxidation in hydrocarbon/air diffusion flames at atmospheric pressure, *Combustion and Flame*, 132, (2003), pp. 43–57.
- [92] C. H. Kim, A. M. El-Leathy, F. Xu, G. M. Faeth, Soot surface growth and oxidation in laminar diffusion flames at pressures of 0.1–1.0 atm, *Combustion and Flame*, 136, (2004), pp. 191–207.
- [93] C. H. Kim, F. Xu, G. M. Faeth, Soot surface growth and oxidation at pressures up to 8.0 atm in laminar nonpremixed and partially premixed flames, *Combustion and Flame*, 152, (2008), pp. 301–316.

- [94] M. Kalogirou, Z. Samaras, Soot oxidation kinetics from TG experiments, *Journal of Thermal Analysis and Calorimetry*, 99, (2010), pp. 1005–1010.
- [95] H. N. Sharma, L. Pahalagedara, A. Joshi, S. L. Suib, A. B. Mhadeshwar, Experimental Study of Carbon Black and Diesel Engine Soot Oxidation Kinetics Using Thermogravimetric Analysis, *Energy and Fuels*, 26, (2012), pp. 5613–5625.
- [96] P. Roth, O. Brandt, S. von Gersum, High Temperature Oxidation of Suspended Soot Particles Verified by CO and CO₂ Measurements, *Proceedings of the Combustion Institute*, 23, (1990), pp. 1485–1491.
- [97] M. B. Fernandes, J. O. Skjemstad, B. B. Johnson, J. D. Wells, P. Brooks, Characterization of carbonaceous combustion residues. I. Morphological, elemental and spectroscopic features, *Chemosphere*, 51(8), (2003), pp. 785–795.
- [98] O. B. Popovitcheva, N. M. Persiantseva, M. E. Trukhin, G. B. Rulev, N. K. Shonija, Y. Ya. Buriko, A. M. Starik, B. Demirdjian, D. Ferry, J. Suzanne, Experimental characterization of aircraft combustor soot: Microstructure, surface area, porosity and water adsorption, *Physical Chemistry Chemical Physics*, 2(19), (2000), pp. 4421–4426.
- [99] K. J. Rockne, G. L. Taghon, D. S. Kosson, Pore structure of soot deposits from several combustion sources, *Chemosphere*, 41(8), (2000), pp. 1125–1135.
- [100] J. Hounslow, R. L. Ryall, V. R. Marshall, A Discretized Population Balance for Nucleation, Growth, and Aggregation, *AIChE Journal*, 34(11), (1988), pp. 1821–1832.
- [101] R. P. Lindstedt, V. Markaki, R. K. Robinson, Oxidation of two-ringed aromatic species as models for soot surface reactions, in: H. Bockhorn, A. D’Anna, H. Wang, eds., *Combustion Generated Fine Carbonaceous Particles*, KIT Scientific Publishing, Karlsruhe, 2009, pp. 499–521.
- [102] J. M. Robertson, Bond-Length Variations in Aromatic Systems, *Acta Crystallographica*, 1(1-6), (1948), pp. 101–109.

- [103] H. Wang, M. Frenklach, A detailed kinetic modeling study of aromatics formation in laminar premixed acetylene and ethylene flames, *Combustion and Flame*, 110(1-2), (1997), pp. 173–221.
- [104] R. K. Robinson, R. P. Lindstedt, On the chemical kinetics of cyclopentadiene oxidation, *Combustion and Flame*, 158(4), (2011), pp. 666–686.
- [105] M. P. Meyer, The Application of Detailed and Systematically Reduced Chemistry to Transient Laminar Flames, Ph.D. thesis, Imperial College London, 2001.
- [106] R. P. Lindstedt, M. A. Selim, Reduced Reaction Mechanisms for Ammonia Oxidation in Premixed Laminar Flames, *Combustion Science and Technology*, 99(4-6), (1994), pp. 277–298.
- [107] V. Sick, F. Hildenbrand, P. Lindstedt, Quantitative laser-based measurements and detailed chemical kinetic modeling of nitric oxide concentrations in methane-air counterflow diffusion flames, *Proceedings of the Combustion Institute*, 27(1), (1998), pp. 1401–1409.
- [108] W. Juchmann, H. Latzel, D. I. Shin, G. Peiter, T. Dreier, H. R. Volpp, J. Wolfrum, R. P. Lindstedt, K. M. Leung, Absolute radical concentration measurements and modeling of low-pressure CH₄/O₂/NO flames, *Proceedings of the Combustion Institute*, 27(1), (1998), pp. 469–476.
- [109] F. Xu, P. B. Sunderland, G. M. Faeth, Soot formation in laminar premixed ethylene/air flames at atmospheric pressure, *Combustion and Flame*, 108(4), (1997), pp. 471–493.
- [110] S. Hanisch, H. Jander, T. Pape, H. G. Wagner, Soot Mass Growth and Coagulation of Soot Particles in C₂H₄/Air-Flames at 15 bar, *Proceedings of the Combustion*, 25, (1994), pp. 577–584.
- [111] The University of Adelaide, International Sooting Flame (ISF) Workshop, <http://www.adelaide.edu.au/cet/isfworkshop/>.
- [112] P. P. J. Stroomer, J. E. de Vries, T. H. van der Meer, Effects of Small- and Large-Scale Structures in a Piloted Jet Diffusion Flame, *Flow, Turbulence and Combustion*, 62, (1999), pp. 53–68.

- [113] N. H. Qamar, Z. T. Alwahabi, Q. N. Chan, G. J. Nathan, D. Roekaerts, K. D. King, Soot volume fraction in a piloted turbulent jet non-premixed flame of natural gas, *Combustion and Flame*, 156(7), (2009), pp. 1339–1347.
- [114] M. E. Mueller, H. Pitsch, LES model for sooting turbulent nonpremixed flames, *Combustion and Flame*, 159(6), (2012), pp. 2166–2180.
- [115] P. Donde, V. Raman, M. E. Mueller, H. Pitsch, LES/PDF based modeling of soot-turbulence interactions in turbulent flames, *Proceedings of the Combustion Institute*, 34(1), (2013), pp. 1183–1192.
- [116] P. A. Nooren, H. A. Wouters, T. W. J. Peeters, D. Roekaerts, U. Maas, D. Schmidt, Monte Carlo PDF modelling of a turbulent natural-gas diffusion flame, *Combustion Theory and Modelling*, 1(1), (1997), pp. 79–96.
- [117] B. Merci, B. Naud, D. Roekaerts, Flow and Mixing Fields for Transported Scalar PDF Simulations of a Piloted Jet Diffusion Flame ('Delft Flame III'), *Flow, Turbulence and Combustion*, 74(3), (2005), pp. 239–272.
- [118] B. Merci, D. Roekaerts, B. Naud, Study of the performance of three micromixing models in transported scalar PDF simulations of a piloted jet diffusion flame ("Delft Flame III"), *Combustion and Flame*, 144(3), (2006), pp. 476–493.
- [119] D. Roekaerts, B. Merci, B. Naud, Comparison of transported scalar PDF and velocity-scalar PDF approaches to 'Delft flame III', *Comptes Rendus Mécanique*, 334(8-9), (2006), pp. 507–516.
- [120] A. Habibi, B. Merci, D. Roekaerts, Turbulence radiation interaction in Reynolds-averaged Navier-Stokes simulations of nonpremixed piloted turbulent laboratory-scale flames, *Combustion and Flame*, 151(1-2), (2007), pp. 303–320.
- [121] S. Ayache, E. Mastorakos, Conditional Moment Closure/Large Eddy Simulation of the Delft-III Natural Gas Non-premixed Jet Flame, *Flow, Turbulence and Combustion*, 88, (2012), pp. 207–231.
- [122] J. E. de Vries, Study on Turbulent Fluctuations in Diffusion Flames using Laser Induced Fluorescence, Ph.D. thesis, TU Delft, 1994.

- [123] C. R. Shaddix, J. Zhang, Measurement of Joint Temperature-Volume Fraction Statistics of Soot in Turbulent Non-Premixed Jet Flames, Proceedings of the European Combustion Meeting, (2013), pp. 1–6.
- [124] B. S. Haynes, H. G. Wagner, Soot Formation, Progress, 7, (1981), pp. 229–273.
- [125] K. H. Homann, Formation of Large Molecules, Particulates and Ions in Premixed Hydrocarbon Flames; Progress and Unresolved Questions, Proceedings of the Combustion Institute, 20, (1984), pp. 857–870.
- [126] C. J. Dasch, The Decay of Soot Surface Growth Reactivity and Its Importance in Total Soot Formation, Combustion and Flame, 61, (1985), pp. 219–225.
- [127] I. T. Woods, B. S. Haynes, Soot Surface Growth at Active Sites, Combustion and Flame, 85, (1991), pp. 523–525.
- [128] F. Mauss, T. Schäfer, H. Bockhorn, Inception and growth of soot particles in dependence on the surrounding gas phase, Combustion and Flame, 99(3-4), (1994), pp. 697–705.
- [129] R. A. Dobbins, R. A. Fletcher, H.-C. Chang, The Evolution of Soot Precursor Particles in a Diffusion Flame, Combustion and Flame, 115, (1998), pp. 285–298.
- [130] F. Xu, K.-C. Lin, G. M. Faeth, Soot Formation in Laminar Premixed Methane/Oxygen Flames at Atmospheric Pressure, Combustion and Flame, 115, (1998), pp. 195–209.
- [131] F. Xu, G. M. Faeth, Soot Formation in Laminar Acetylene/Air Diffusion Flames at Atmospheric Pressure, Combustion and Flame, 125, (2001), pp. 804–819.
- [132] A. M. El-Leathy, F. Xu, C. H. Kim, G. M. Faeth, Soot Surface Growth in Laminar Hydrocarbon/Air Diffusion Flames, AIAA Journal, 41(5), (2003), pp. 856–865.
- [133] J. Singh, M. Balthasar, M. Kraft, W. Wagner, Stochastic modeling of soot particle size and age distributions in laminar premixed flames, Proceedings of the Combustion Institute, 30, (2005), pp. 1457–1465.

- [134] M. Balthasar, M. Frenklach, Detailed kinetic modeling of soot aggregate formation in laminar premixed flames, *Combustion and Flame*, 140, (2005), pp. 130–145.
- [135] A. Faccinetto, P. Desgroux, M. Ziskind, E. Therssen, C. Focsa, High-sensitivity detection of polycyclic aromatic hydrocarbons adsorbed onto soot particles using laser desorption/laser ionization/time-of-flight mass spectrometry: An approach to studying the soot inception process in low-pressure flames, *Combustion and Flame*, 158, (2011), pp. 227–239.
- [136] P. D. Teini, D. M. A. Karwat, A. Atreya, Observations of nascent soot: Molecular deposition and particle morphology, *Combustion and Flame*, 158, (2011), pp. 2045–2055.
- [137] A. Veshkini, S. B. Dworkin, M. J. Thomson, A soot particle surface reactivity model applied to a wide range of laminar ethylene/air flames, *Combustion and Flame*, 161(12), (2014), pp. 3191–3200.
- [138] A. Khosousi, S. B. Dworkin, Detailed modelling of soot oxidation by O₂ and OH in laminar diffusion flames, *Proceedings of the Combustion Institute*, 35(2), (2015), pp. 1903–1910.
- [139] A. Khosousi, S. B. Dworkin, Soot surface reactivity during surface growth and oxidation in laminar diffusion flames, *Combustion and Flame*, 162(12), (2015), pp. 4523–4532.
- [140] C. R. Shaddix, Data provided to the third International Sooting Flame (ISF) Workshop, 2016.
- [141] The University of Adelaide, International Sooting Flame (ISF) Workshop, <http://www.adelaide.edu.au/cet/isfworkshop/data-sets/turbulent/>, accessed 08/02/2016.
- [142] R. P. Lindstedt, H. Ozarovskiy, Joint scalar transported PDF modeling of nonpiloted turbulent diffusion flames, *Combustion and Flame*, 143(4), (2005), pp. 471–490.
- [143] P. Rodrigues, B. Franzelli, R. Vicquelin, O. Gicquel, N. Darabiha, Coupling an LES approach and a soot sectional model for the study of sooting turbulent non-premixed flames, *Combustion and Flame*, 190, (2018), pp. 477–499.

- [144] F. Sewerin, S. Rigopoulos, An LES-PBE-PDF approach for predicting the soot particle size distribution in turbulent flames, *Combustion and Flame*, 189, (2018), pp. 62–76.
- [145] W. Boyette, S. Chowdhury, W. Roberts, Soot particle size distribution functions in a turbulent non-premixed ethylene-nitrogen flame, *Flow, Turbulence and Combustion*, 98(4), (2017), pp. 1173–1186.
- [146] S. Chowdhury, W. R. Boyette, W. L. Roberts, Time-averaged probability density functions of soot nanoparticles along the centerline of a piloted turbulent diffusion flame using a scanning mobility particle sizer, *Journal of Aerosol Science*, 106, (2017), pp. 56–67.
- [147] K. P. Geigle, M. Köhler, W. O’Loughlin, W. Meier, Investigation of soot formation in pressurized swirl flames by laser measurements of temperature, flame structures and soot concentrations, *Proceedings of the Combustion Institute*, 35, (2015), pp. 3373–3380.